## General Disclaimer

### One or more of the Following Statements may affect this Document

- This document has been reproduced from the best copy furnished by the organizational source. It is being released in the interest of making available as much information as possible.

- This document may contain data, which exceeds the sheet parameters. It was furnished in this condition by the organizational source and is the best copy available.

- This document may contain tone-on-tone or color graphs, charts and/or pictures, which have been reproduced in black and white.

- This document is paginated as submitted by the original source.

- Portions of this document are not fully legible due to the historical nature of some of the material. However, it is the best reproduction available from the original submission.

Produced by the NASA Center for Aerospace Information (CASI)

WASHCON

J. Mastasky, 482

CR# 95618

# FINAL REPORT FOR THE DUAL CHANNEL SCANNING RADIOMETER

Contract No. NAS5-10414

Prepared by

RCA Defense Electronic Products
Astro-Electronics Division

FACILITY FORM 602

N69-28504 (ACCESSION NUMBER) (THRU) 1

119 (PAGES) (CODE)

CR 95618 (NASA CR OR TMX OR AD NUMBER) 14 (CATEGORY)

JUL 1968
RECEIVED
NASA STI FACILITY
INPUT BRANCH

for

National Aeronautics and Space Administration
Goddard Space Flight Center
Greenbelt, Maryland

# FINAL REPORT
# FOR THE
# DUAL CHANNEL
# SCANNING RADIOMETER

Contract No. NAS5-10414

Prepared by

RCA Defense Electronic Products
Astro-Electronics Division

for

National Aeronautics and Space Administration
Goddard Space Flight Center
Greenbelt, Maryland

AED R-3278

Issued: January 25, 1968
Princeton, New Jersey

PRECEDING PAGE BLANK NOT FILMED.

## TABLE OF CONTENTS


| Section | | Page |
|---|---|---|
| I | INTRODUCTION AND SUMMARY | 1 |
| II | TECHNICAL DISCUSSION | 9 |
| | A. GENERAL DESCRIPTION OF RADIOMETER | 9 |
| | B. PROBLEM AREAS DEFINED | 15 |
| | 1. Spatial Resolution | 15 |
| | 2. Visual Channel Dynamic Range | 16 |
| | 3. Stray Light | 16 |
| | 4. Data Handling | 16 |
| | C. RADIOMETER DESIGN | 17 |
| | 1. Optical Design | 17 |
| | a. Geometrical Requirements and Optical Layout | 17 |
| | b. Spectral Characteristics | 20 |
| | c. Stray Light Tests | 20 |
| | d. Sun Shade Design | 25 |
| | e. In-Flight Radiometric Calibration | 35 |
| | 2. Radiometer Electronics | 36 |
| | a. Low-Noise Preamplifiers | 36 |
| | (1) Sources of Amplifier Noise | 36 |
| | (2) Amplifier Design | 38 |
| | (3) Sample Design | 41 |
| | (4) Bolometer-Preamplifier Interface | 42 |
| | b. Infrared Channel Signal Electronics | 47 |
| | (1) Introduction | 47 |
| | (2) Detailed Description | 53 |
| | (3) Sensitivity Calculations | 56 |
| | c. Visual Channel Signal Electronics | 58 |
| | (1) Introduction | 58 |
| | (2) Detailed Description | 59 |
| | (3) Visual Channel Sensitivity Calculation | 66 |
| | 3. Logic | 70 |
| | a. Introduction | 70 |
| | b. Logic Design | 71 |
| | c. Logic Operation | 72 |
| | 4. Scanning Mirror-Velocity Control Loop | 78 |
| | a. Basic Requirements | 78 |
| | b. Design for Short-Term Jitter Requirements | 78 |

TABLE OF CONTENTS (Continued)


| Section | | | Page |
|---|---|---|---|
| | | c. Design for Long-Term Velocity Requirements | 80 |
| | 5. | Power Supply | 90 |
| | 6. | Mechanical Design | 95 |
| | 7. | Packaging Design | 99 |
| | 8. | Telemetry | 101 |
| D. | | RADIOMETER CALIBRATION AND TEST | 105 |
| | 1. | Alignment and Focussing | 105 |
| | 2. | Spatial Resolution Measurements | 106 |
| E. | | SPACECRAFT INTERFACE | 107 |
| | 1. | Mechanical | 107 |
| | 2. | Electrical | 107 |
| | 3. | Data Handling | 108 |
| F. | | DIGITAL DATA HANDLING | 109 |

## LIST OF ILLUSTRATIONS


| Figure | | Page |
|---|---|---|
| 1 | Photographs of the Dual Channel Scanning Radiometer Engineering Model | 2 |
| 2 | Oscilloscope Pictures Showing Resolution Capabilities of the Dual Channel Scanning Radiometer Engineering Model | 6 |
| 3 | Resolution of Dual Channel Scanning Radiometer Engineering Model Compared to TOS Camera Systems | 7 |
| 4 | Dual Channel Radiometer, Block Diagram | 11 |
| 5 | Dual Channel Scanning Radiometer Signal Outputs | 14 |
| 6 | Radiometer Optical Layout | 18 |
| 7 | Detector-Filter-Beamsplitter Subassembly | 19 |
| 8 | Infrared Filter Spectral Transmission of Combined Elements | 21 |
| 9 | Visual Channel Spectral Characteristics | 21 |
| 10 | Test Setup for Stray Light Measurements | 22 |
| 11 | Comparison Plot of $\Delta V$ for Various Data Sets | 23 |
| 12 | Response to Light Scattered From White Paper | 24 |
| 13 | Installation of Honeycomb, Schematic Diagram | 27 |
| 14 | Honrycomb Refinement | 29 |
| 15 | Field-of-View With and Without Honeycomb | 31 |
| 16 | Approximate Modulation Transfer Function MTF With and Without Honeycomb | 33 |
| 17 | Visual Channel In-Flight Calibration Assembly | 36 |
| 18 | Amplifier Noise Spectrum Versus Frequency | 38 |
| 19 | Broadband NF vs Source Resistance for a Typical Low-Noise Bipolar Transistor and an FET Amplifier | 39 |
| 20 | Broadband NF vs Source Resistance for a Typical Low-Noise Bipolar Transistor and an FET Amplifier | 40 |

## LIST OF ILLUSTRATIONS (Continued)


| Figure | | Page |
|---|---|---|
| 21 | Spot NF vs Frequency for the IR Channel Amplifier | 41 |
| 22 | Basic Bolometer Bridge Circuit | 43 |
| 23 | Bolometer-Amplifier Coupling Methods | 45 |
| 24 | Infrared Channel Response Curves | 24 |
| 25 | IR Channel Signal Electronics, Schematic Wiring Diagram | 49 |
| 26 | Frequency Response Characteristics of IR Channel Preamplifier | 54 |
| 27 | Temperature Resolution vs Scene Temperature | 59 |
| 28 | Visual Channel Signal Electronics, Schematic Wiring Diagram | 61 |
| 29 | Light Diode Resistance Loading and Amplifier Configuration | 63 |
| 30 | Conditioning Networks, Schematic Diagrams | 64 |
| 31 | Transfer Characteristics, Log Mode | 67 |
| 32 | Transfer Characteristics, Semilog Mode | 67 |
| 33 | Transfer Characteristics, Linear Mode | 68 |
| 34 | Transfer Characteristics, Ultralinear Mode | 68 |
| 35 | Dual Channel Radiometer, Logic Diagram | 73 |
| 36 | Six-Level Voltage Calibration Generator | 75 |
| 37 | Radiometer Mirror-Velocity Control Loop Block Diagram | 79 |
| 38 | Bipolar PWM $\phi$-Detector for Phase-Locked Mirror Speed Control Position Loop | 81 |
| 39 | PWM Timing Diagram | 82 |
| 40 | Sensor Amplifier Duty Cycle | 83 |
| 41 | Motor Drive Electronics, Schematic Wiring Diagram | 85 |

## LIST OF ILLUSTRATIONS (Continued)


| Figure | | Page |
|---|---|---|
| 42 | Position Notch Filter and Notch Pulldown . . . . . | 87 |
| 43 | Compensation Network . . . . . | 88 |
| 44 | Zener Diode Amplitude-Limited PWM Output . . . . . | 88 |
| 45 | Velocity Loop Characteristics . . . . . | 89 |
| 46 | Phase-Lock Loop Characteristics . . . . . | 90 |
| 47 | Power Supply, Block Diagram . . . . . | 91 |
| 48 | DC-to-DC Converter, Schematic Diagram . . . . . | 93 |
| 49 | Typical Voltage Regulator, Simplified Schematic . . . . . | 95 |
| 50 | Dual Channel Radiometer, Mechanical Configuration . . . . . | 97 |
| 51 | Dual Channel Radiometer Electronics Packaging . . . . . | 100 |
| 52 | Telemetry, Logic, and Gating Circuits, Schematic Wiring Diagram . . . . . | 103 |
| 53 | Digital Data Handling System for Radiometer . . . . . | 110 |

## LIST OF TABLES


| Table | | Page |
|---|---|---|
| 1 | Summary of Parameters for Dual Channel Scanning Radiometer Engineering Model | 5 |
| 2 | Effect of Honeycomb on Low Frequency Response | 32 |
| 3 | Effect of Honeycomb on High Spatial Frequencies | 32 |
| 4 | Solar Irradiance Outside the Atmosphere | 69 |
| 5 | Logic Input Timing | 71 |
| 6 | Types of Logic Modules | 72 |
| 7 | Logic Outputs and Times of Events | 76 |
| 8 | Logic Truth Table | 77 |

# SECTION I

# INTRODUCTION AND SUMMARY

The Astro-Electronics Division (AED) of RCA submits to NASA this final engineering report covering the engineering design, development, construction and test of a Dual Channel Radiometer for Improved TOS under contract No. NAS 5-10414.

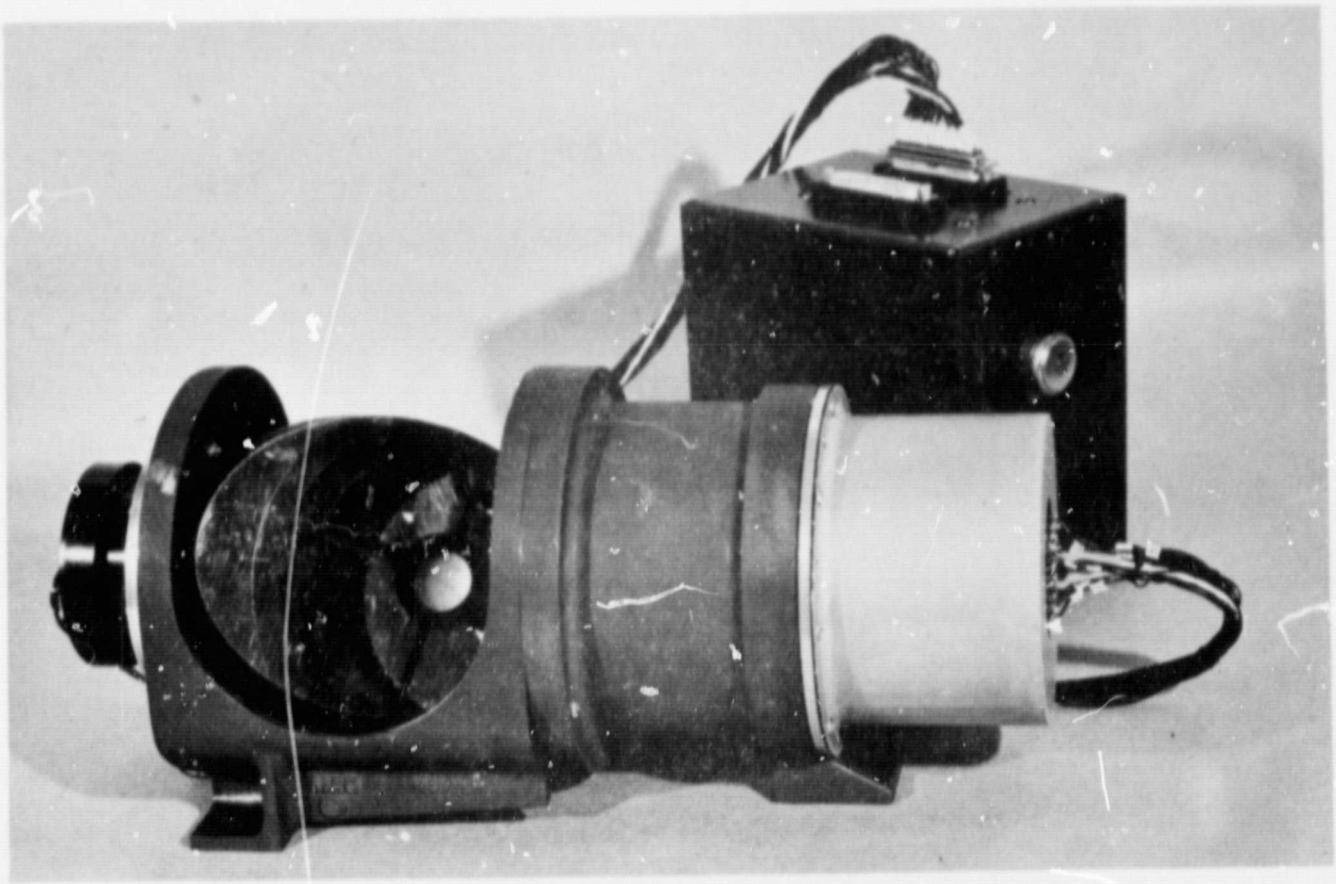
The primary purpose of this contract was to study and develop advanced electronic techniques that are applicable to the general requirements of improving the sensitivity and spatial resolution and radiometric accuracy of imaging radiometers designed for use on meteorological spacecraft such as the Improved TOS.

Imaging radiometers, such as the one shown in Figure 1, have become increasingly important in observing cloud cover and other geophysical phenomena from orbiting spacecraft.* These radiometers generate two dimensional pictures using a rotating mirror for the across-track scan with the velocity vector of the spacecraft providing the vertical scan. The principal advantages of radiometers over their predecessor sensor (the vidicon television camera) are: the ability to image in darkness, thus providing possible 24-hour coverage; radiometric accuracy over the entire picture; and freedom from certain scan distortions. Because of these inherent advantages it has become important to improve the performance of imaging radiometers; thus, the work reported here has been dedicated to advancing the state-of-art in radiometry.

During contract No. NAS 5-10414, RCA developed and tested an engineering model dual channel scanning radiometer. This radiometer has an instantaneous field of view of 2.8 milliradians which can provide a ground resolution of two miles from

---

* W. Nordberg in "Geophysical Observations from Nimbus I", Science Vol. 150, October 19, 1965.



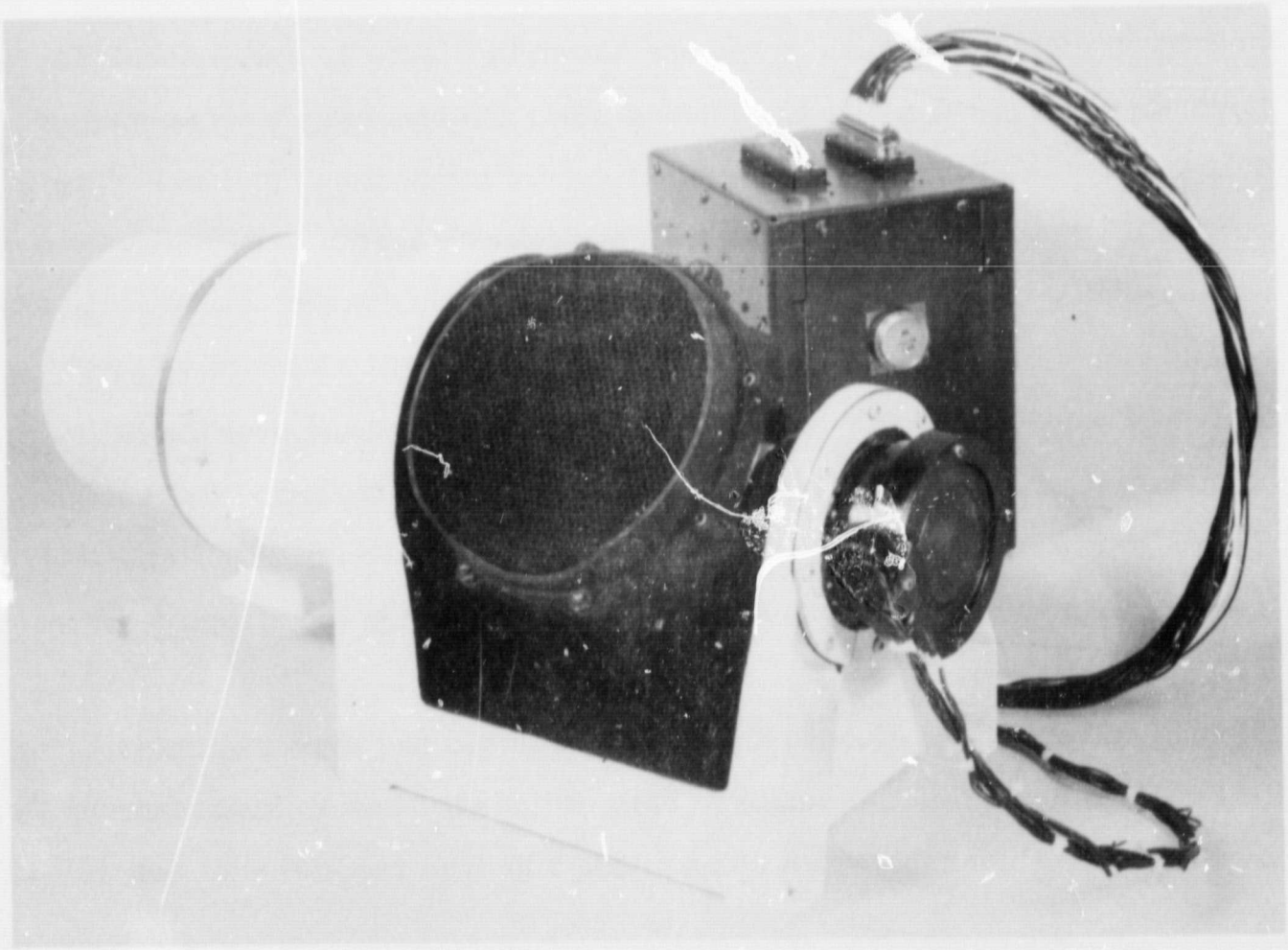


Figure 1. Photographs of the Dual Channel Scanning Radiometer Engineering Model

the TOS spacecraft attitude of 775 nautical miles. This is the best known resolution performance of a imaging radiometer using a thermal bolometer detector and possibly represents the limit of performance with this type of detector. The emphasis of the program, as noted before, was on the electronics portions of the radiometers and in this area the following techniques were implemented or studied:

- Unique bolometer amplifier coupling scheme which uses direct coupling and clamp feedback to obtain d-c stability.

- Investigation of commercially available operational amplifiers for low-level preamplifiers that provide nearly perfect noise figures.

- Use of both linear and logarithmic transfer function in the visual channel to cover the range of 1 to 10, 000 foot-lamberts scenes despite the approximately 30 db dynamic range limitation of the data storage and transmission links.

- Study of the possible advantages of digitizing the video output to preserve dynamic range, signal-to-noise ratio, and radiometer accuracy. Included in this study were schemes for reducing bandwidth with digital techniques, and possible tape recorder configurations that could handle the data requirements.

In the optical-mechanical portions of the radiometer, the following items were studied or developed:

- Extension and reduction to practice of RCA's previous work in direct drive of the scanning mirror using a dc torque motor and servo loop to provide low jitter and excellent speed accuracy.

- Investigation of possible sources of stray light interference into the optics and design of a rotating-honeycomb sunshade to provide rejection of stray light by as much as 500 times.

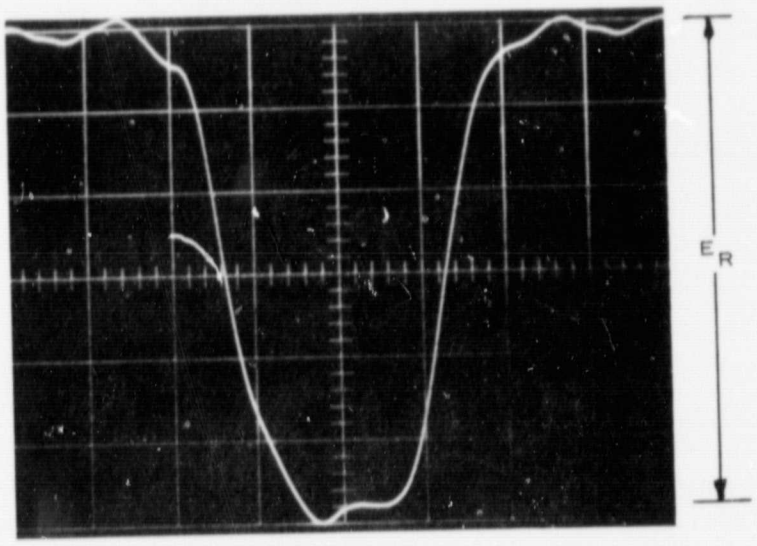
A dual channel radiometer was developed that will operate on spacecraft similar to the Improved TOS, which can provide both infrared and visual pictures with spatial resolution equivalent to that available from present ITOS vidicon television cameras. Table 1 is a summary of parameters for the dual channel scanning radiometer engineering model.

The resolution capabilities of the model are illustrated in Figures 2 and 3. The work on suppression of stray light using honeycomb sunshades was extremely promising. Figure 1A illustrates a honeycomb shade on the engineering model. Further work should be devoted to techniques for fabricating these sunshades to the precision required for maximum attenuation of stray light and minimum obscuration of desired signal.

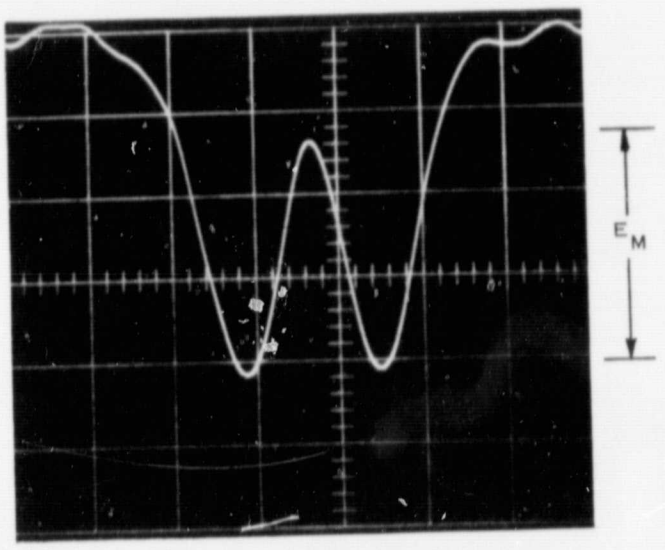
The study of digital techniques for preserving signal fidelity from the radiometer, and for reducing bandwidth requirements showed the value of digital data handling. Follow-on work to implement an all-digital radiometer channel with data stretching would be useful in developing a capability for transmitting scanning radiometer data while preserving dynamic range, signal-to-noise ratio, and radiometric accuracy.

TABLE 1. SUMMARY OF PARAMETERS FOR DUAL CHANNEL SCANNING RADIOMETER ENGINEERING MODEL

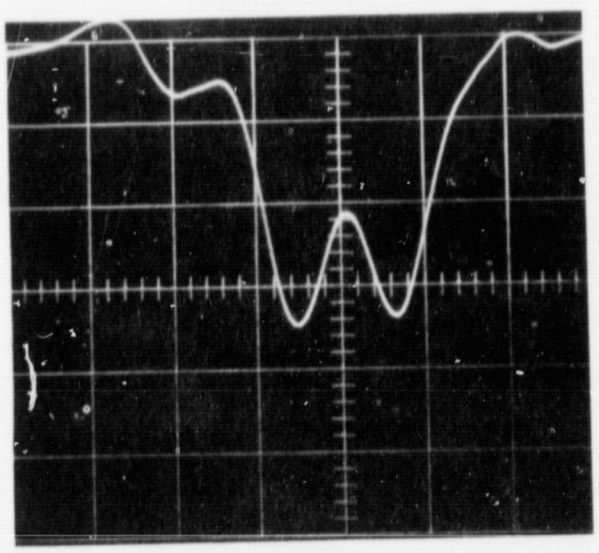
| Parameter | Value |
|---|---|
| Spatial Resolution (at Subpoint and 775 n. m. altitude) | |
| Infrared | 2.0 nautical miles @ 19% response |
| Visual (linear and semilog mode) | 2.0 nautical miles @ 50% response |
| Temperature Resolution ($NE\triangle N = 4 \times 10^{-5}$ watts-$cm^{-2}$-$ster^{-1}$) | 1.3°K @ 300°K<br>3.4°K @ 220°K<br>5.2°K @ 200°K |
| Spectral bandwidth: | |
| IR (at 50% transmission points) | 10.5 to 12.5 microns |
| Visual | 0.5 to 0.75 micron |
| Collecting Optics: | |
| Objective | 5 inches (cassegrain) |
| Focal Length | 18 inches |
| Radiance Dynamic Range (IR) | 190°K to 330°K |
| Radiance Dynamic Range (Visual) | A. 1 to 10,000 ft-lamberts (log)<br>B. 300 to 10,000 ft-lamberts (lin)<br>C. 300 to 10,000 ft-lamberts (semilog) |
| Detector: | |
| IR | Immersed thermistor bolometer |
| Active Area | 0.08 × 0.08 millimeter |
| Responsivity | 1920 volts/watt |
| Visual | Silicon Photovoltaic |
| Active Area | 0.020 × 0.020 inch |
| Responsivity (peak) | 45 amps/watt |
| Mirror Rotation Rate | 90 rpm |
| Jitter | 1.4 milliradians (p-p max) |
| Bandwidth (IR and visual each) | 0-1680 Hz |
| Overall Size | |
| Radiometer | 16.58 × 6.75 × 7.12 inches |
| Electronics | 8 × 5.5 × 7 inches |
| Overall Weight | |
| Radiometer | 11.8 lb |
| Electronics | 5.5 lb |
| Overall Power | 9.5 watts |



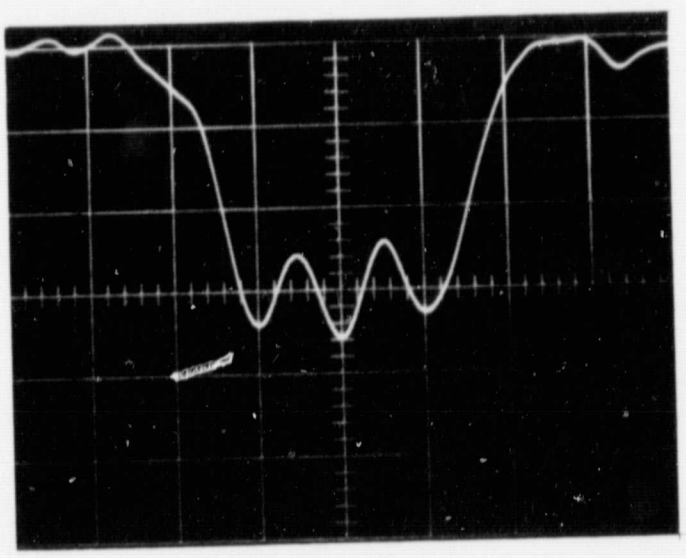

9.7 MILES



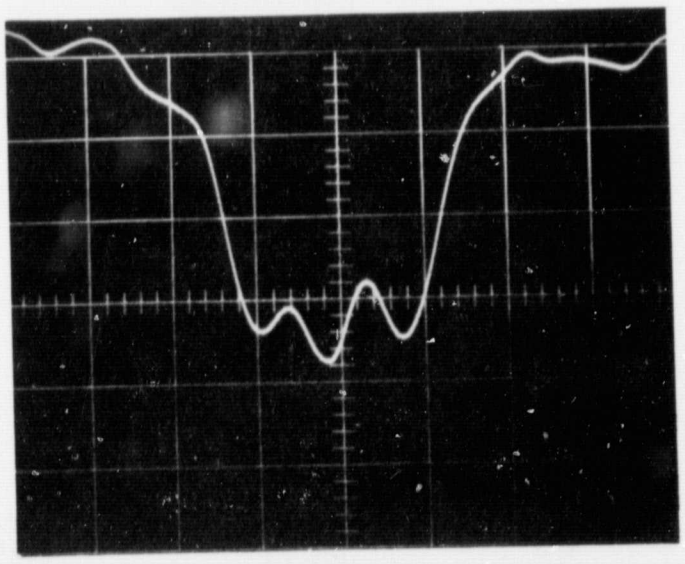

3.1 MILES



2.23 MILES



1.94 MILES



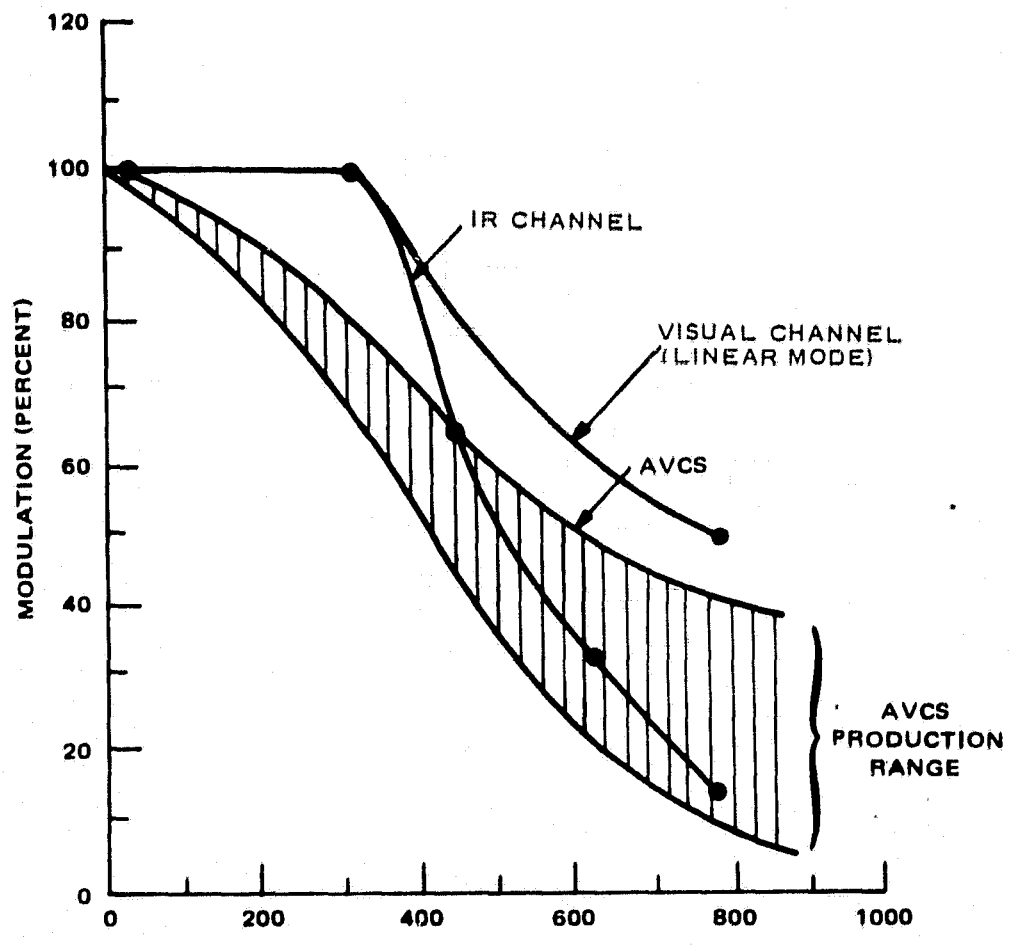
1.69 MILES

[HORIZONTAL 0.5 MS/MAJOR DIV
VERTICAL 1V/MAJOR DIV]

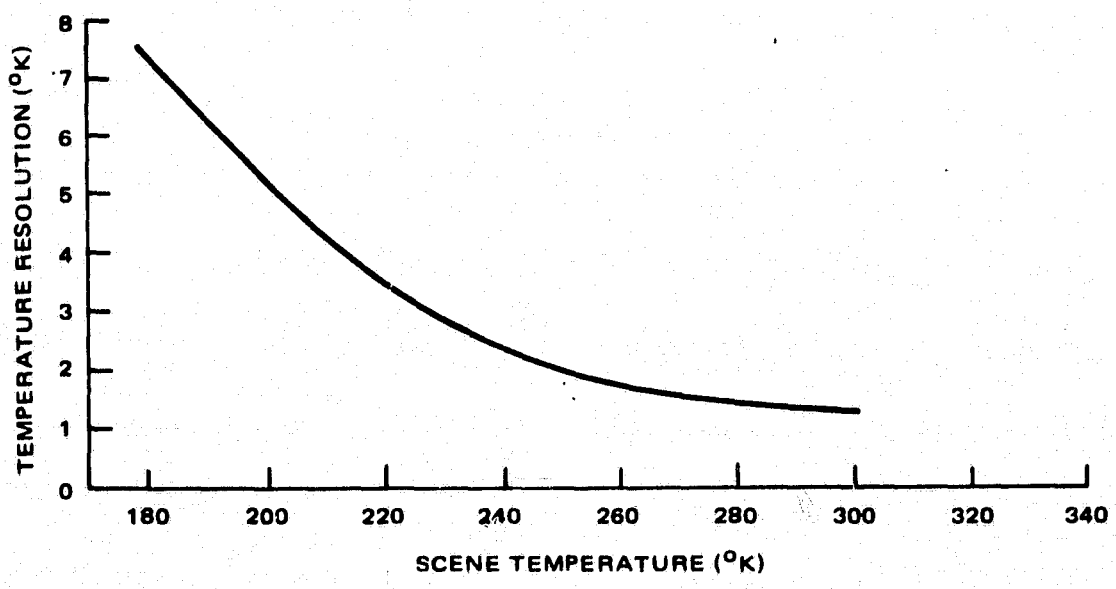
$$\text{MODULATION } \% = \frac{E_M}{E_R} \times 100$$

NOTE: RESOLUTION PATTERNS WERE TWO BAR FOR 3.1 AND 2.23 MILES, THREE BARS FOR 1.94 AND 1.69 MILES, AND NONE FOR 9.7 MILES. BAR PATTERNS WERE PLACED IN FRONT OF A BLACKBODY WITH AN EQUIVALENT SCENE TEMPERATURE OF 330° K.

Figure 2. Oscilloscope Pictures Showing Resolution Capabilities of the Dual Channel Scanning Radiometer Engineering Model




(a) Resolution of Radiometer compared to TOS AVCS cameras




(b) Temperature Resolution

Figure 3. Resolution of Dual Channel Scanning Radiometer Engineering Model Compared to TOS Camera Systems

## SECTION II

## TECHNICAL DISCUSSION

### A. GENERAL DESCRIPTION OF RADIOMETER

The Dual Channel Scanning Radiometer, shown in Figure 1, was designed to operate on an earth-oriented, stabilized platform spacecraft, such as the Improved TOS, with the prime objective of providing infrared and visual pictures with a spatial resolution (2.0 nautical miles) comparable to the existing AVCS and APT television cameras. The radiometer is of the line-scan type with a single rotating mirror providing the horizontal scan. A block diagram of the radiometer is shown in Figure 4.

The vertical component of the picture is provided by the forward motion of the spacecraft in orbit. The rotation rate of the scanning mirror is 90 rpm — a rate which is both compatible with motors used in ground displays and with the spatial resolution requirement. The unobscured angle of scan is 140 degrees symmetrically about the nadir.

The 8-to 13-micron atmospheric window permits both day and night sensing of emitted earth radiation. The reflected solar radiation is negligible in this window, but is very significant in the 3.4- to 4.2-micron window, reducing the utility of the shorter wavelength window to nighttime use only. Using the entire 8 to 13-micron window, reduces the absolute temperature accuracy compared to the performance obtainable using the 10.5 to 12.5-micron portion because of water vapor and ozone constituents present in the band between 8 and 10 microns.

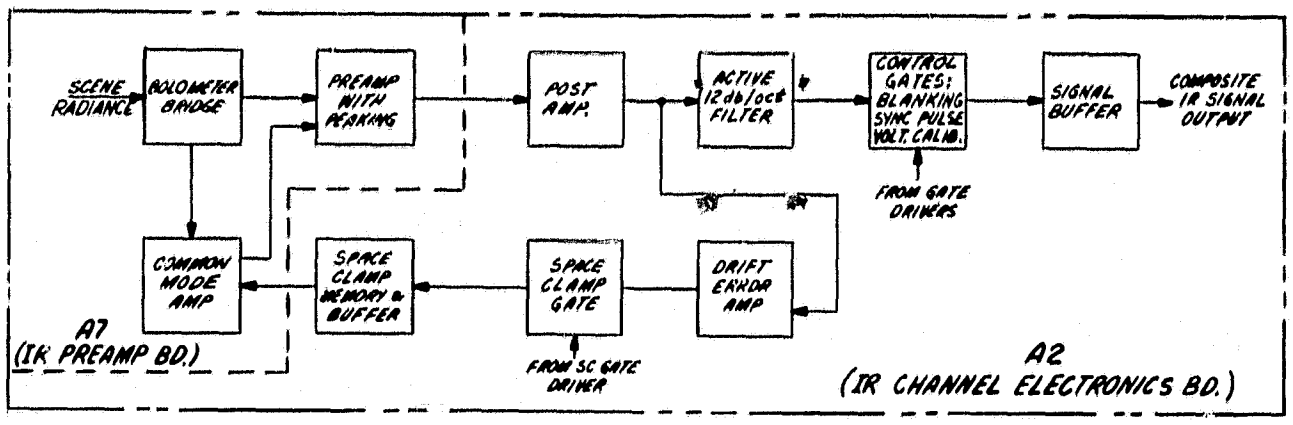
In the narrower interval, the blackbody radiant energy available is about 43 percent that in the full window, or the equivalent is that the S/N ratio of the observations is reduced by the same factor. This, in turn, might normally be expected to result in a decrease in temperature measurement accuracy; but, in the real atmosphere, it does not! The full window includes a narrow but significant ozone absorption band. The actual concentration of $O_3$ in the atmosphere at any given time and place is

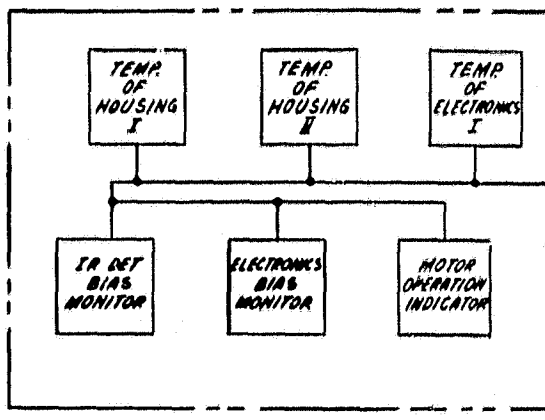
unknown, although it is known that the ozone concentration varies by a factor of 2 over the globe. Furthermore, the ozone in the atmosphere is concentrated in the upper strotosphere and mesosphere, well above the clouds, and is relatively warm. Thus, very cold clouds or surfaces observed from a satellite would be essentially obscured by the ozone. Elsewhere, its effect is to reduce the S/N ratio of the temperature measurements by about the same factor of 2. Thus, the temperature measurement accuracy using the full atmospheric window is no better than that achieved with the reduced spectral interval. Actually, the reduced spectral band can result in improved temperature accuracy. The upper part of the window includes some carbon dioxide absorption lines. With the elimination of the ozone, it is feasible to correct for the carbon dioxide effect. Thus, the choice in this tradeoff is for use of the narrow spectral band, 10.5 to 12.5 microns.

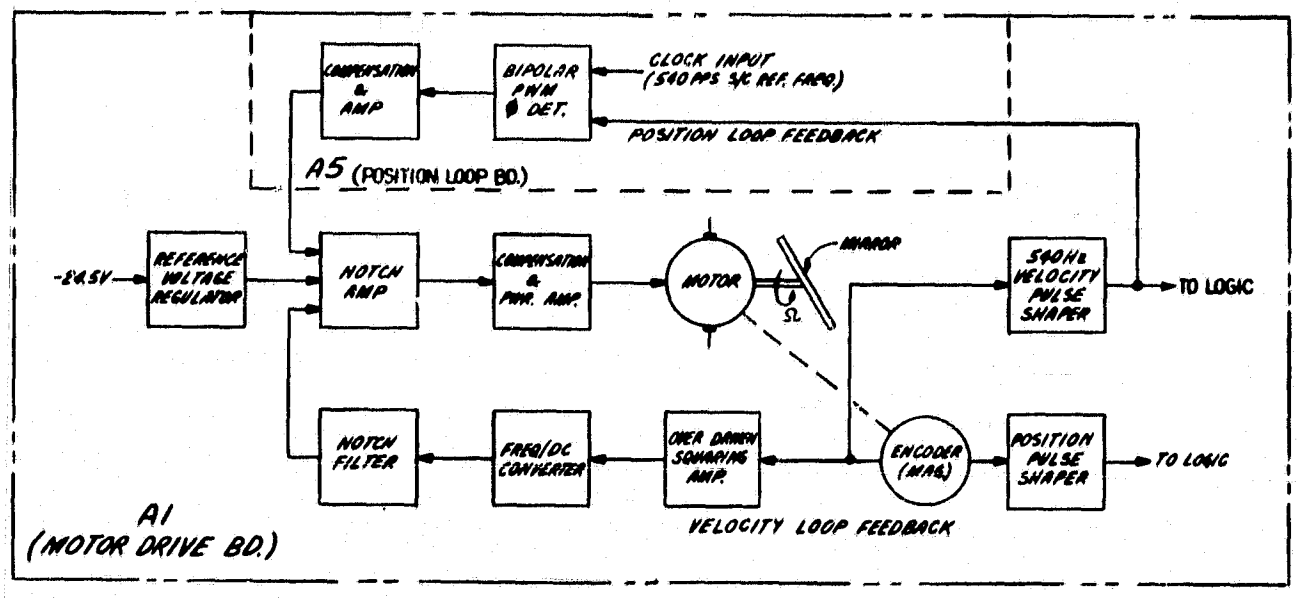
The visual channel uses a photovoltaic silicon detector which is considerably more sensitive than the infrared detector and can provide good cloud-cover pictures in twilight illumination. The spectral interval of this channel will approximately match the spectral characteristics of the television camera to be used on the Improved TOS spacecraft. The full dynamic range of the visual channel exceeds the electronics linearity capability. To overcome this limitation, the radiometer provides three different ranges, one linear and two logarithmic, to cover a 1 to 10,000 foot-lambert range.

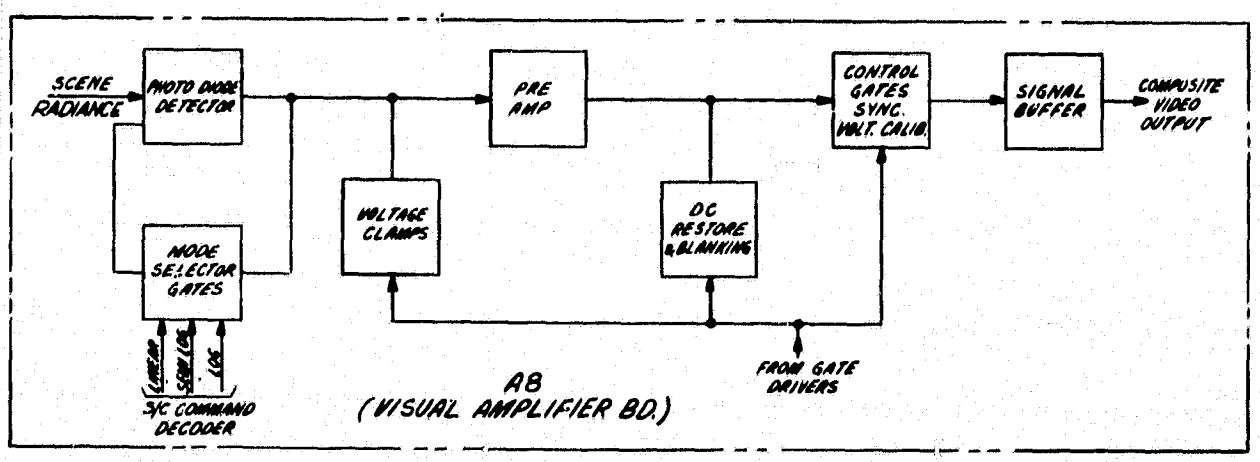
The collecting optics used are common to both channels, thus, permitting positive registration of the visual and infrared pictures.

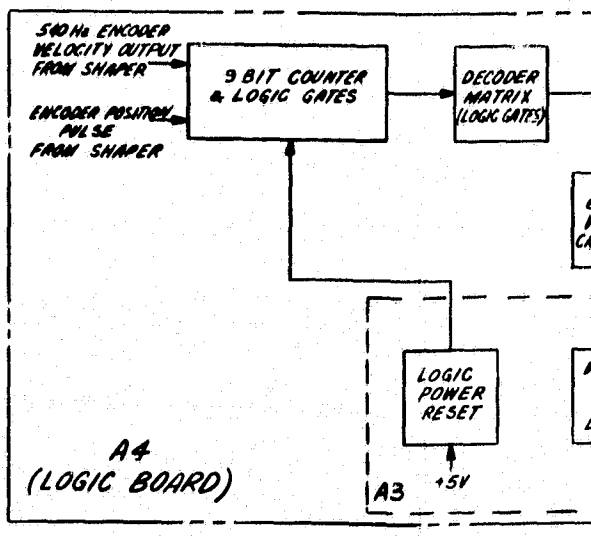
Radiometric and electronic gain calibration of both channels of the radiometer are provided along with the video signal while the equipment is in orbit. This type of calibration is similar to that used on the Nimbus HRIR and MRIR, and on infrared systems produced at AED. This calibration is achieved by viewing two known sources of radiation: (1) space and housing for the infrared, and (2) space and a calibrated lamp bulb for the visual channel.


SCENE RADIANCE
BOLOMETER BRIDGE
PREAMP WITH PEAKING
POST AMP.
ACTIVE 12db/oct FILTER
CONTROL GATES; BLANKING SYNC PULSE VOLT. CALIB.
SIGNAL BUFFER
COMPOSITE IR SIGNAL OUTPUT
FROM GATE DRIVERS
COMMON MODE AMP
SPACE CLAMP MEMORY & BUFFER
SPACE CLAMP GATE
DRIFT ERROR AMP
FROM SC GATE DRIVER
A7 (IR PREAMP BD.)
A2 (IR CHANNEL ELECTRONICS BD.)

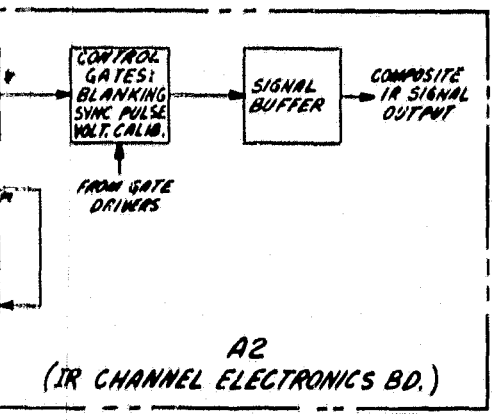

TEMP. OF HOUSING I
TEMP. OF HOUSING II
TEMP. OF ELECTRONICS I
IR DET BIAS MONITOR
ELECTRONICS BIAS MONITOR
MOTOR OPERATION INDICATOR

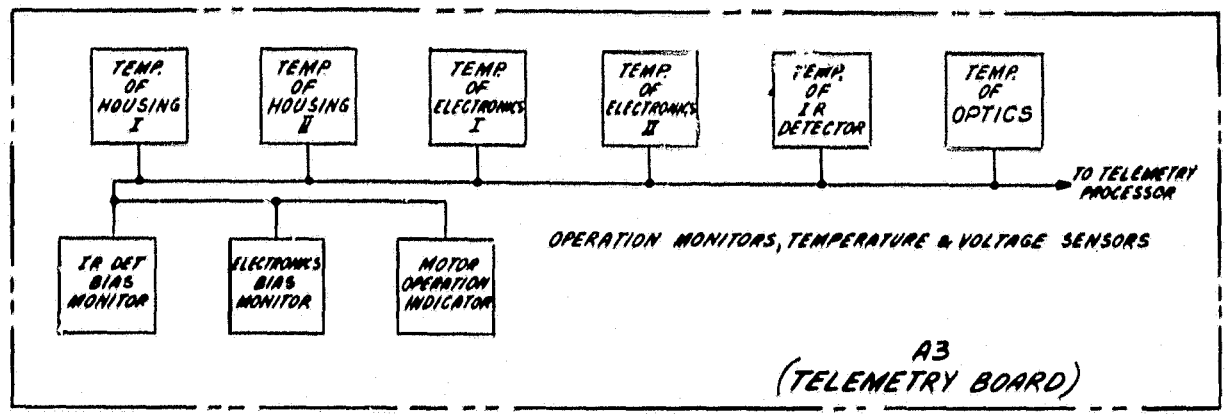

COMPENSATION & AMP
BIPOLAR PWM DET.
CLOCK INPUT (540 PPS SYC REF. FREQ)
POSITION LOOP FEEDBACK
A5 (POSITION LOOP BD.)
-24.5V
REFERENCE VOLTAGE REGULATOR
NOTCH AMP
COMPENSATION & PWR. AMP.
MOTOR
ARMATURE
Ω
540Hz VELOCITY PULSE SHAPER
TO LOGIC
NOTCH FILTER
FREQ/DC CONVERTER
OVER DRIVEN SQUARING AMP.
ENCODER (MAG.)
POSITION PULSE SHAPER
TO LOGIC
VELOCITY LOOP FEEDBACK
A1 (MOTOR DRIVE BD.)

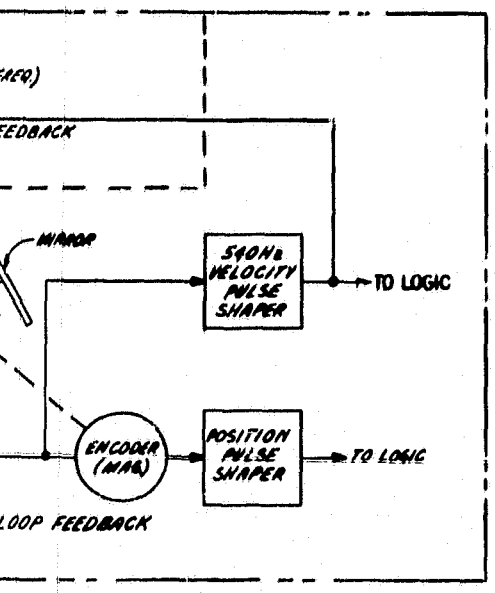

SCENE RADIANCE
PHOTO DIODE DETECTOR
PRE AMP
CONTROL GATES SYNC. VOLT. CALIB.
SIGNAL BUFFER
COMPOSITE VIDEO OUTPUT
MODE SELECTOR GATES
VOLTAGE CLAMPS
DC RESTORE & BLANKING
FROM GATE DRIVERS
LINE SYNC
SCAN LOG
LOG
S/C COMMAND DECODER
A8 (VISUAL AMPLIFIER BD.)

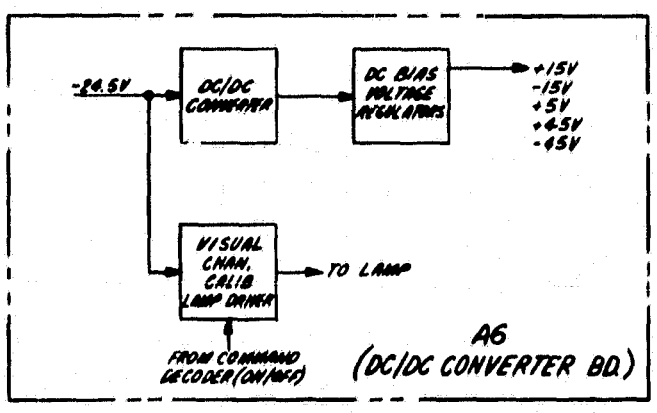

540 Hz ENCODER VELOCITY OUTPUT FROM SHAPER
ENCODER POSITION PULSE FROM SHAPER
9 BIT COUNTER & LOGIC GATES
DECODER MATRIX (LOGIC GATES)
LOGIC POWER RESET
+5V
A3
A4 (LOGIC BOARD)

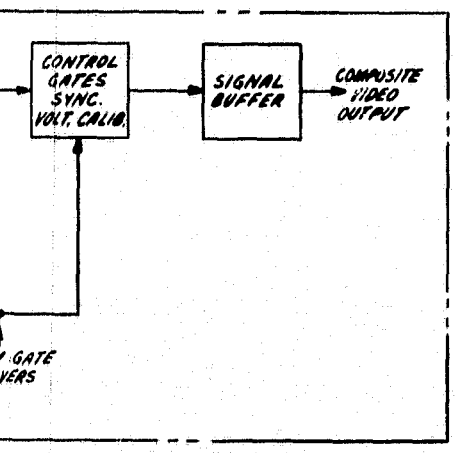
Foldout #1

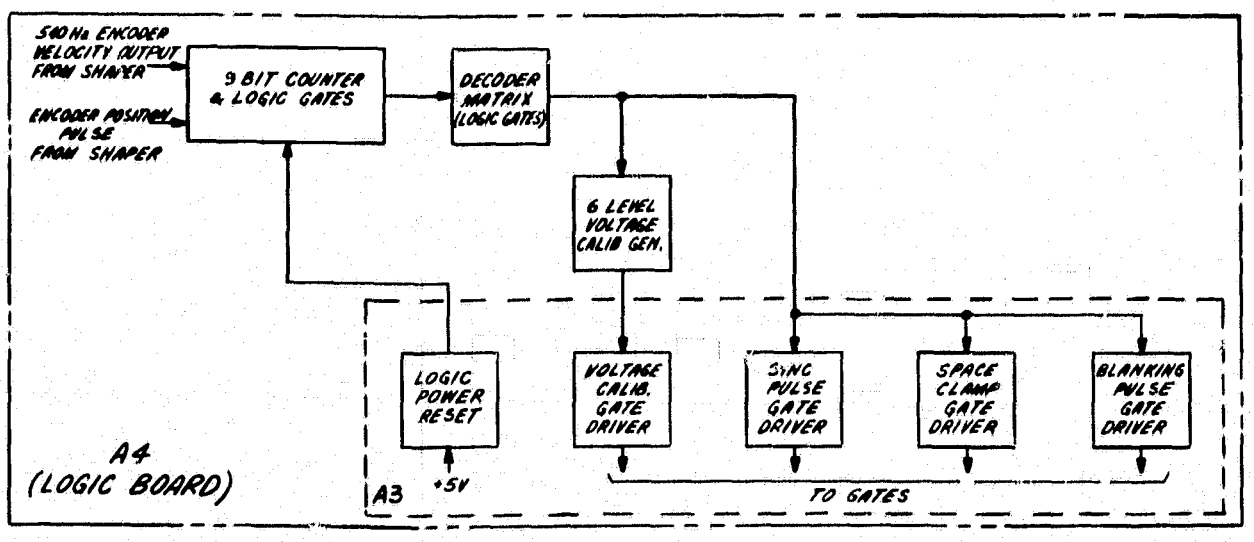



Foldout #2

**Figure 4. Dual Channel Scanning Radiometer, Block Diagram**

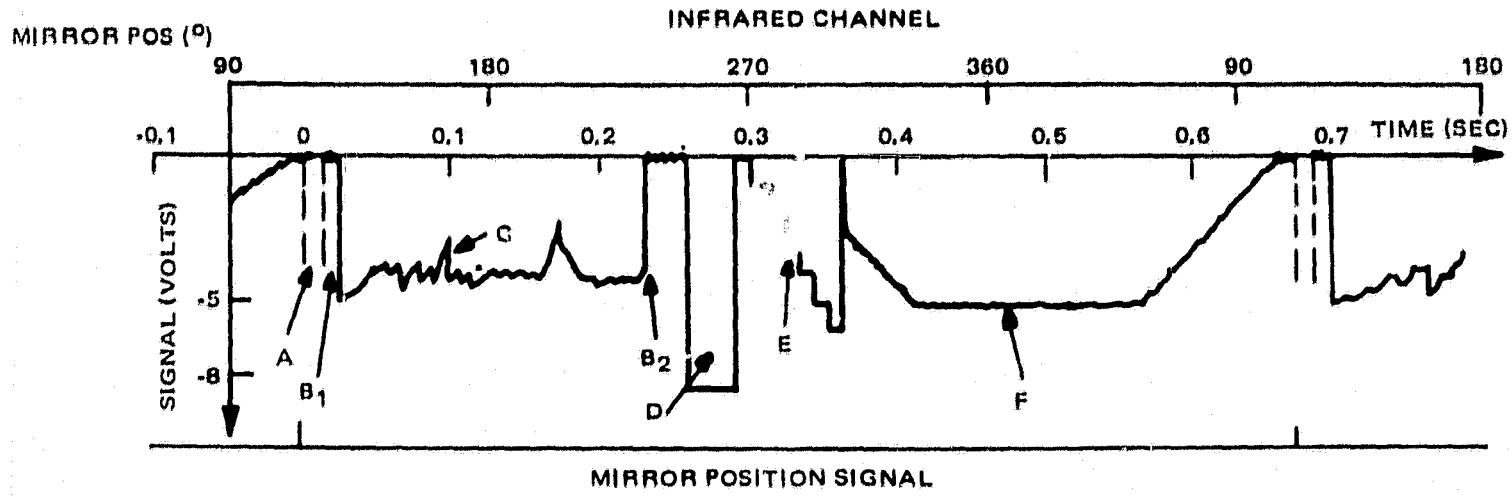
The radiometer is designed in one basic configuration, although a left-hand and right-hand version may be desirable. One configuration can be changed to the other by a simple electrical change of a prewired plug to reverse the motor direction and encoder outputs.

A d-c brush-torque motor rotates the scanning mirror at 90 rpm to provide the horizontal component of scan with the speed controlled by a feedback loop around the motor referenced to a stable 540 Hz * frequency from the spacecraft. The waveforms resulting from a typical scan of the radiometer are shown in Figures 5(a) and 5(b). At 22 milliseconds before the radiometer views the earth's horizon, a line-start pulse from the encoder triggers the sequence of events shown in Figure 5 by initiating the clamp and following timing function. Since this timing unit has both start and frequency information it can generate all the other events using a simple pulse-counting technique. A line starts with a 12 millisecond clamp during which time the mirror views space. For all practical purposes, space emits zero radiance in both the visible and infrared spectrum and this fact is used as a zero reference to clamp both channels to zero voltage output. At 10 milliseconds before horizon crossing, the clamps are removed and the mirror scans the earth for 205 milliseconds (or 114 degrees). At 260 milliseconds an 8-volt full-scale sync pulse is inserted. This sync occurs after earth time to permit the sync to occur first on playback of a tape recorder, thus simplifying ground demodulation. After sync, an accurately generated 6-level stair voltage is inserted to provide linearity information; this allows ground correction of amplitude and gain distortion that may occur in tape recorders, transmitters, and ground receiver and display equipment.

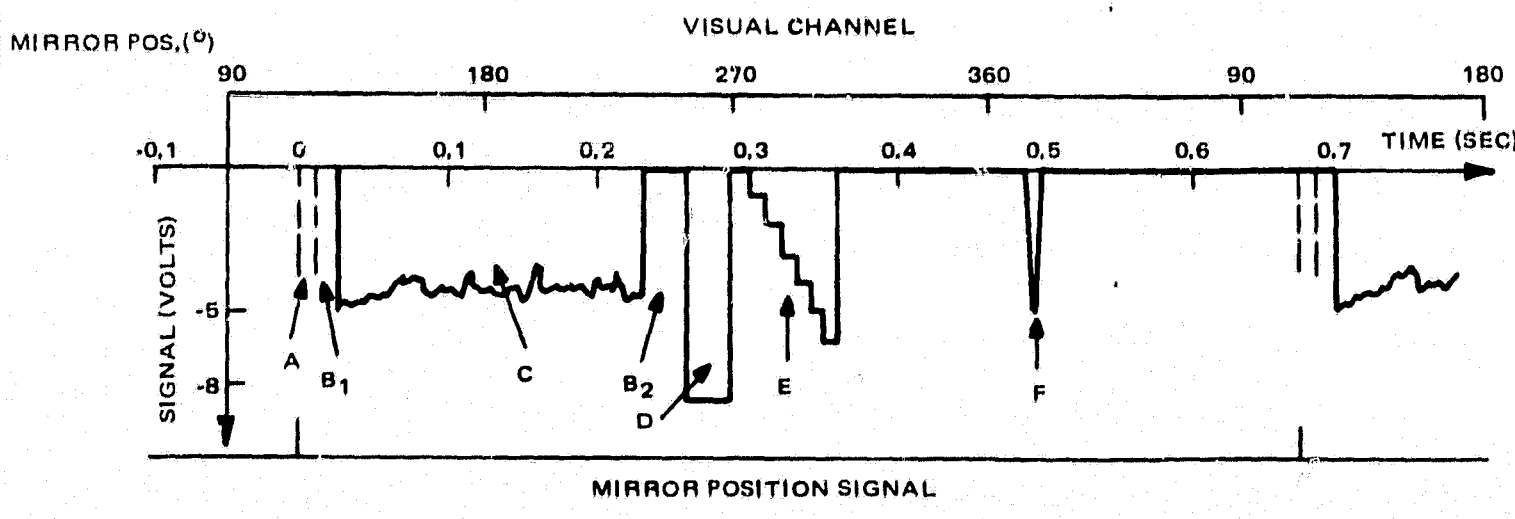
After the voltage stair, the video is gated on when the mirror views the housing and a calibration lamp which provides the means for calibrating both the infrared and visual channels . The mirror again views outer space at 667 milliseconds at which time the horizontal scan line is initiated.

---

* The frequency of 540 Hz was used in place of the 400 Hz normally available in the Improved TOS spacecraft because 540 Hz matches a standard 360 tooth encoder that was immediately available. In a final design, the encoder frequency would be specified to match the available 480-Hz frequency.




A. AMPLIFIER RESTORE PERIOD, 12.5 MS
B. OUTER SPACE SCAN
    1. PRE-EARTH 10 MS, MIN.
    2. POST EARTH 22.5 MS, MIN.
C. EARTH SCAN, 205 MS, MAX.
D. SYNC SIGNAL
    10 MS AT 0.0 VOLTS
    30 MS AT 8.0 VOLTS
    10 MS AT 0.0 VOLTS
E. CALIB. SIGNAL, 60 MS
F. HOUSING SCAN, 310 MS




A. AMPLIFIER RESTORE PERIOD, 12.5 MS
B. OUTER SPACE SCAN
    1. PRE-EARTH 10 MS, MIN.
    2. POST EARTH 22.5 MS, MIN.
C. EARTH SCAN, 205 MS, MAX.
D. SYNC SIGNAL
    10 MS AT 0.0 VOLTS
    30 MS AT 8.0 VOLTS
    10 MS AT 0.0 VOLTS
E. CALIB. SIGNAL, 60 MS
F. CALIB. LAMP SIGNAL, 5 MS

Figure 5. Dual Channel Scanning Radiometer Signal Outputs

## B. PROBLEM AREAS DEFINED

The development of the advanced electronic design techniques for the high-resolution dual channel radiometer system was motivated by performance improvements in the following areas:

- Spatial resolution and temperature sensitivity;
- Infrared detector-amplifier interface;
- Visual channel dynamic range;
- Stray light input from sun interference;
- Data storage and transmission.

### 1. Spatial Resolution

The spatial resolution and temperature sensitivity of a radiometer are interchangeable, and attempts to improve one results in a degradation of the other. The subpoint ground resolution performance value of 2 nautical miles was selected to match that of the present television sensors used on TOS so that previous experience could be used to interpret the images from the radiometer. The sensitivity or noise equivalent temperature difference ($NE\Delta T$) corresponding to this spatial resolution must be optimized to resolve the temperature-of-scene elements especially at cold scene-temperatures. Several techniques, such as the elimination of optical chopping and the use of low-noise amplifiers, are used to improve the sensitivity of the radiometer. Historically, rotating choppers were used to modulate the radiance from the scene imaging on the detector to permit detection of the infrared signal in the presence of a large d-c bias on the detector. In addition to the mechanical objection, the chopper degrades the sensitivity of the detector because the inherently slow detector does not respond efficiently to the chopping frequency required by sampling criteria.

If the use of choppers is eliminated, the sensitivity of the infrared channel for a given spatial and spectral resolution, orbit, and optical system is limited only by the noise performance of the electronics. The ultimate performance is obtained when the system

is detector noise limited. Techniques employed to eliminate the chopper and provide detector noise limited performance are discussed later in this report.

2. Visual Channel Dynamic Range

The silicon photovoltaic detector used in the radiometer is capable of a linear output of at least a seven-decade range, or 0.001 to 10,000 foot-lamberts. The dual channel radiometer has a useful range of better than 1 to 10,000 foot-lamberts (or 80 db), which is 40 to 50 db greater than can be processed with the TOS scanning-radiometer tape recorder and communication channel. To overcome this data channel limitation, the radiometer design allows for generating several nonlinear transfer functions in the visual channel.

3. Stray Light

The sun, although not directly in the field of view, will illuminate the scanning mirror during certain orbital conditions. Laboratory measurements on a radiometer show that a portion of this light will be scattered and will be indistinguishable from true signal, and no technique of internal baffling will be effective in shielding the unwanted signal. Techniques for shielding the scanning mirror from the sun have been studied, and the most promising scheme for solving the problem is discussed later in this report.

4. Data Handling

In addition to covering a wide dynamic range of input signals, radiometers can provide radiometric calibration previously unobtainable with vidicon television cameras. Present analog tape recorders and communication channels cannot handle the dynamic range and linearity without serious distortion. This problem could be solved by converting the radiometer output to a digital signal, a technique which would preserve the dynamic range and linearity of the signal, undistorted, to the final image processing device. This digital processing increases the data channel bandwidth required; however, it also permits the use of certain techniques, such as data

stretching during the backscan and elimination of some of the calibration signals currently used in the analog output. The advantages of using digital data techniques are presented later in this report.

## C. RADIOMETER DESIGN

### 1. Optical Design

#### a. Geometrical Requirements and Optical Layout

The purpose of the radiometer optical system is to image, both on the visual detector and on the infrared detector, an area of the earth which subtends 2.8 milliradians in each of two perpendicular dimensions. The scanning mirror causes the subtended segment to sweep across the earth from horizon-to-horizon in a direction perpendicular to the direction of orbital travel. The entrance aperture of the radiometer optics is selected at a 5-inch diameter to provide an instrument of practical size and weight within the constraints of the Improved TOS spacecraft.

The optical design is partially governed by detector sizes because the boundaries of the active areas of the two detectors serve as the field stops, which define the 2.8-milliradian fields of view in the two channels. Optimum performance is achieved by minimizing detector size.

The active area of the infrared detector is 0.08 x 0.08 millimeters. To achieve the desired 2.8 milliradian field of view, the focal length of the optical system is 28.6 millimeters. The optical system includes the immersion lens, a Cassegrain telescope objective, the infrared filter, the dichroic beamsplitting mirror, and the scanning mirror; however, the last three items do not affect focal length. The immersion lens, which is a hyperhemisphere with the detector at the aplanatic point, results in a demagnification of 16; therefore, the required focal length of the Cassegrain objective is 16 x 28.6 = 457 millimeters, or 18 inches. Departures of the Cassegrain objective and the hyperhemispheric immersion lens from design dimensions have resulted in a measured field of view, in the direction of scan, of 2.76 milliradians in the infrared channel.

The active area of the visual detector is a circle with a diameter of 0.020 inch. To achieve the 2.8-milliradian field of view, the optical system must have a focal length of 0.020/0.0028 = 7.15 inches. The Cassegrain focal length is already set at 18 inches by the IR channel; therefore, a demagnification of 18/7.15, or 2.52, is required.

The visual detector is not immersed, and the demagnification is accomplished by placing a positive lens in front of the detector. The measured field of view, in the direction of scan, in the visual channel is 2.33 milliradians.

The optical layout of the radiometer is shown in Figures 6 and 7: Figure 6 shows the scanning mirror, the Cassegrain objective, the light baffle in front of the Cassegrain primary mirror, and the location of the sensor assembly; details of the sensor

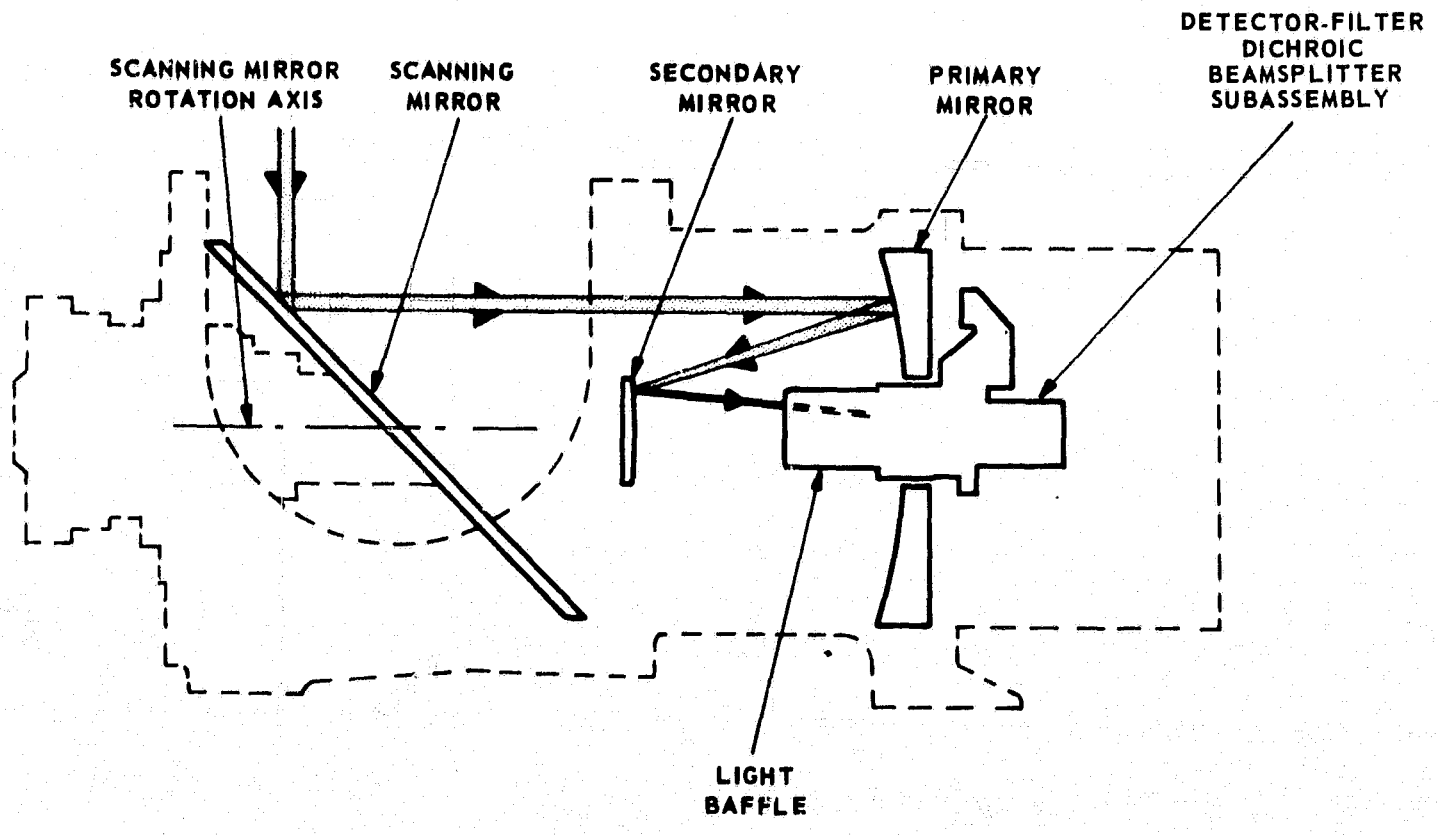



Figure 6. Radiometer Optical Layout

assembly are shown in Figure 7. Radiation from the scene is reflected by the scanning mirror into the Cassegrain system; the same is reflected by the primary mirror to the secondary mirror, which in turn reflects the image to a focus beyond the primary mirror, as shown in the diagram. The light baffle shields the region around the axial focal point from direct exposure to stray radiation which passes the secondary mirror. Image size in the focal plane of the Cassegrain corresponding to the 2.8-milliradian scanning element is $18 \times 0.0028 = 0.054$ inch. The Cassegrain objective was specified to image a point source at infinity with a spot size no larger than 0.0052 inch, and measurements on the completed objective show that almost all the energy is contained within a 0.003-inch circle.

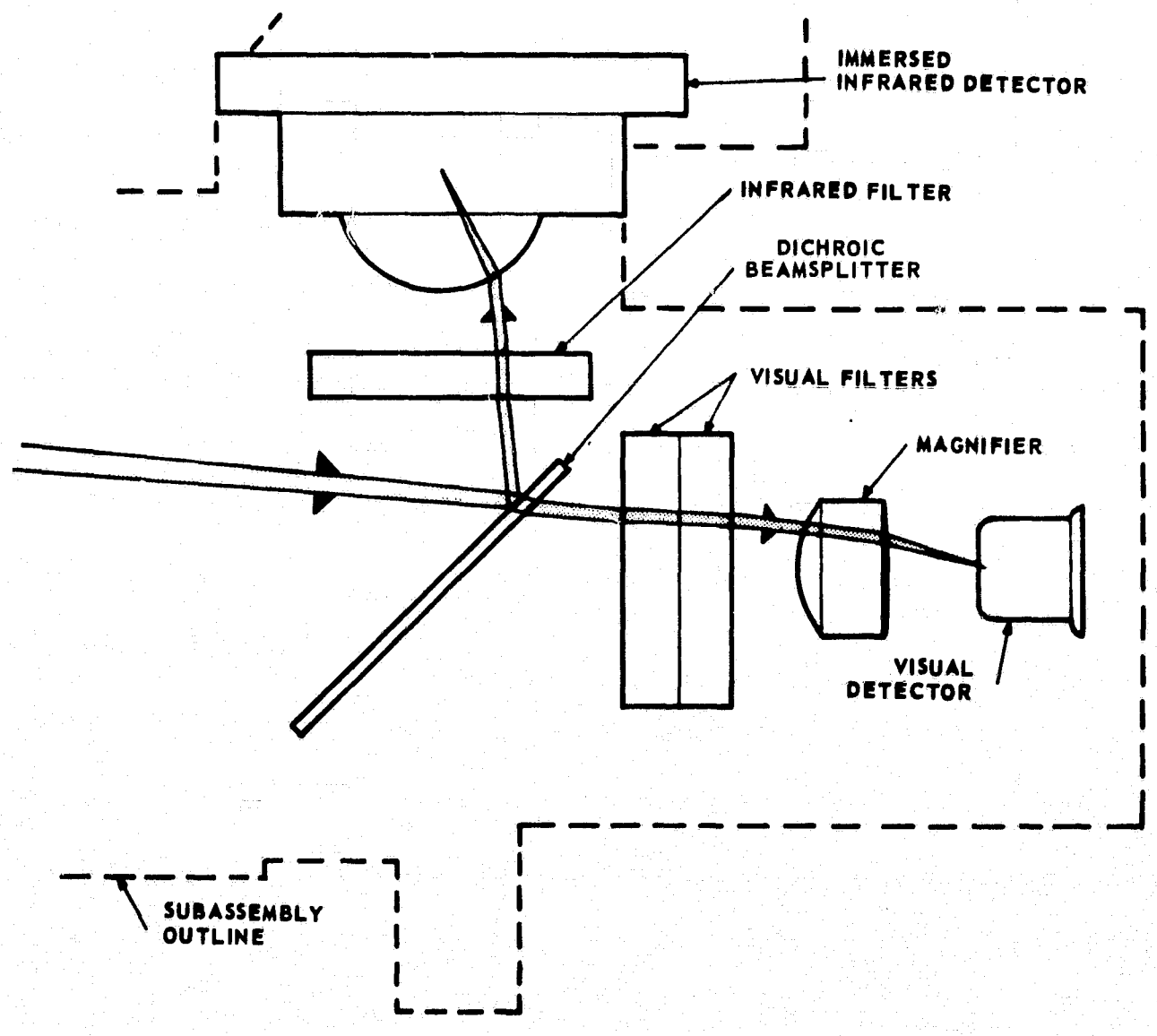



Figure 7. Detector-Filter-Beamsplitter Subassembly

As shown in Figure 7, the radiation entering the sensor assembly from the Cassegrain first encounters the dichroic beamsplitter. The infrared radiation is reflected at a 90-degree angle, and passes through the infrared bandpass filter to the germanium hyper-hemisphere, which focuses the radiation on the immersed thermistor flake. Visible light is transmitted by the beamsplitter, passes through the visual channel wavelength-limiting filters, and is focused on the silicon photodiode by the magnifying lens. The magnifying lens is an achromatic doublet with a focal length of 12.4 millimeters.

b. Spectral Characteristics

In the infrared channel, spectral sensitivity depends almost entirely upon the spectral transmission of the infrared filter, since the optical properties of the remaining components are primarily invariant with wavelength within the transmission band of the filter. The infrared filter consists of two elements. The first element, which has multilayer interference coatings on a germanium substrate, establishes the transmission passband; the second element, made from Barium Flouride, eliminates a subsidiary passband between the 19 and 23 microns. The spectral transmission of the combined elements is shown in Figure 8. Transmission below 9.86 microns and above 13 microns is less than 0.1 percent.

In the visual channel, the long-wavelength and short-wavelength cutoff filters have the greatest effect on spectral sensitivity, but there is some variation with wavelength of the transmission of the beamsplitter and the response of the detector. The cutoff filters are Corning 3-71 and 1-69. The spectral transmission of these two filters and the dichroic beamsplitter, and the spectral response of the detector are shown in Figure 9, as is a curve of the spectral characteristics of the four elements combined, which shows the spectral response of the detector modified by the transmission characteristics of the other three elements.

c. Stray Light Tests

Tests were made to assess the nature and severity of stray light problems in the radiometer. The breadboard radiometer used for these tests has an optical

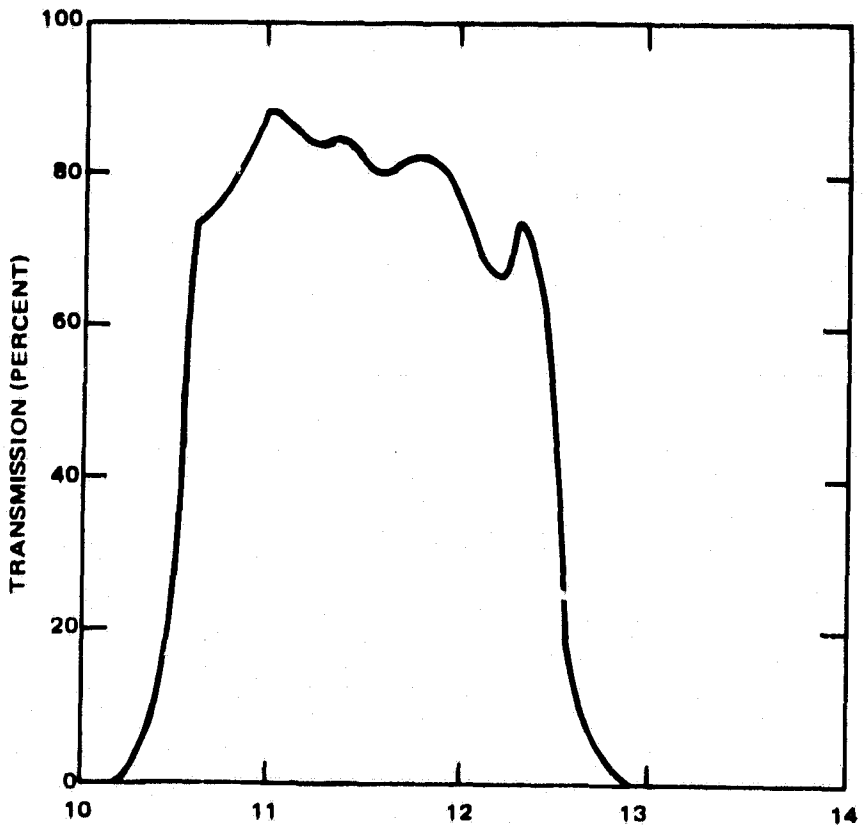



Figure 8. Infrared Filter Spectral Transmission of Combined Elements

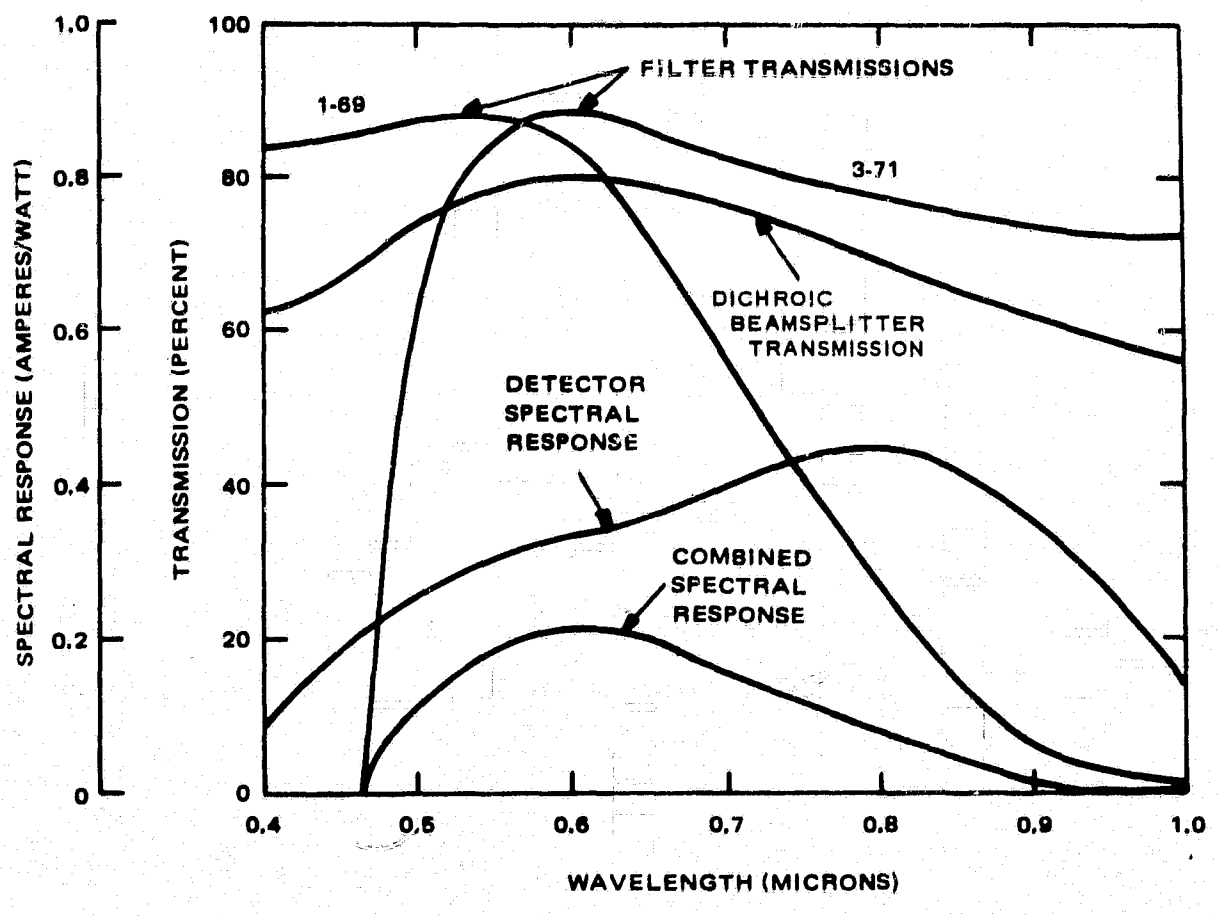



Figure 9. Visual Channel Spectral Characteristics

layout different from that described under "Geometrical Requirements and Optical Layout," but the conclusions drawn from the tests are applicable to the present radiometer. Tests have been made only in the visual channel, because stray radiation is a more serious problem in the visual channel than in the infrared channel. The tests were run using a quartz-iodide Sun Gun to introduce spurious light. A sketch of the test setup is shown in Figure 10. The Sun Gun was placed so that, for the scanning mirror position shown in the figure, light fell on the mirror at near-normal incidence. The detector output was plotted as a function of scanning

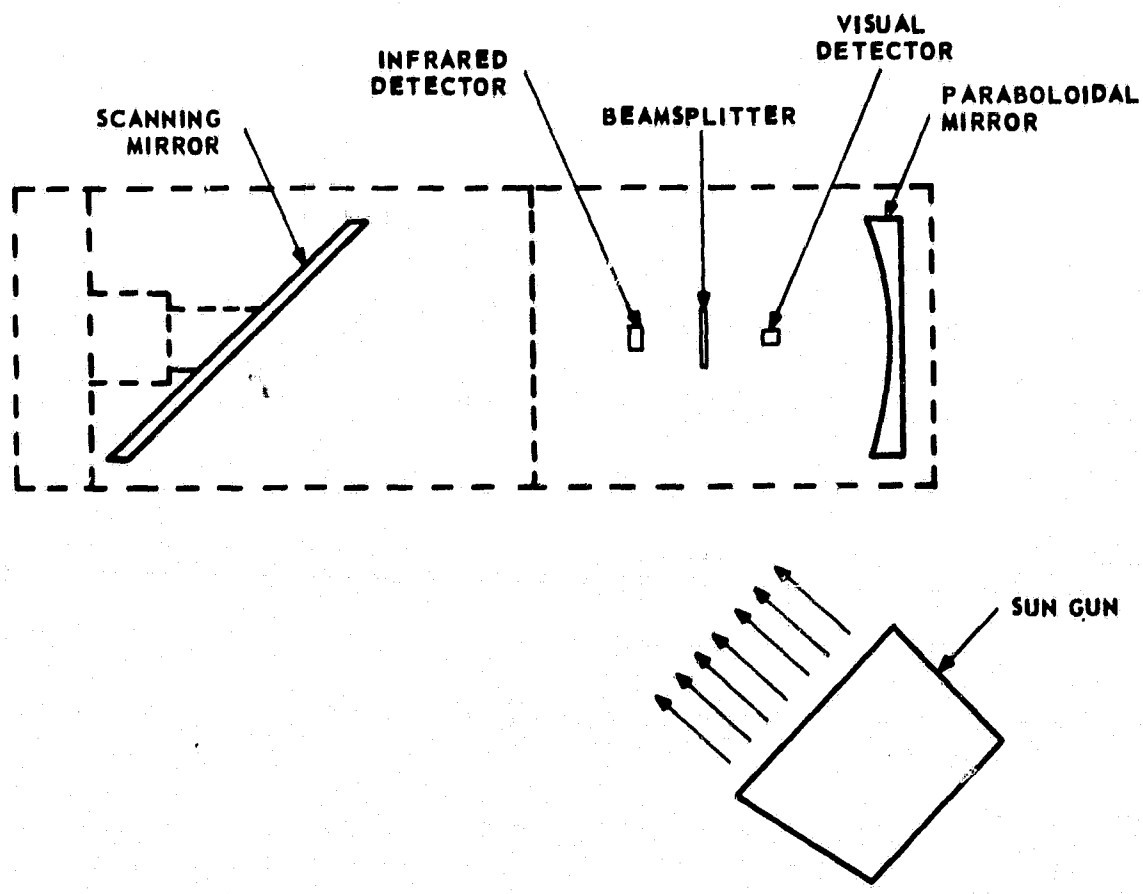



Figure 10. Test Setup for Stray Light Measurements

mirror rotational position, both with the source on and with the source off, for several different sets of conditions. Care was taken to prevent illumination by the Sun Gun of surfaces within the normal field of view of the radiometer.

The first set of measurements was taken with only those baffles necessary to prevent illumination of the normal field of view. The results are plotted as curve "A" in Figure 11. In this case, as in all the following cases, the plotted values are the differences in output signal with the light on and with the light off. The second set

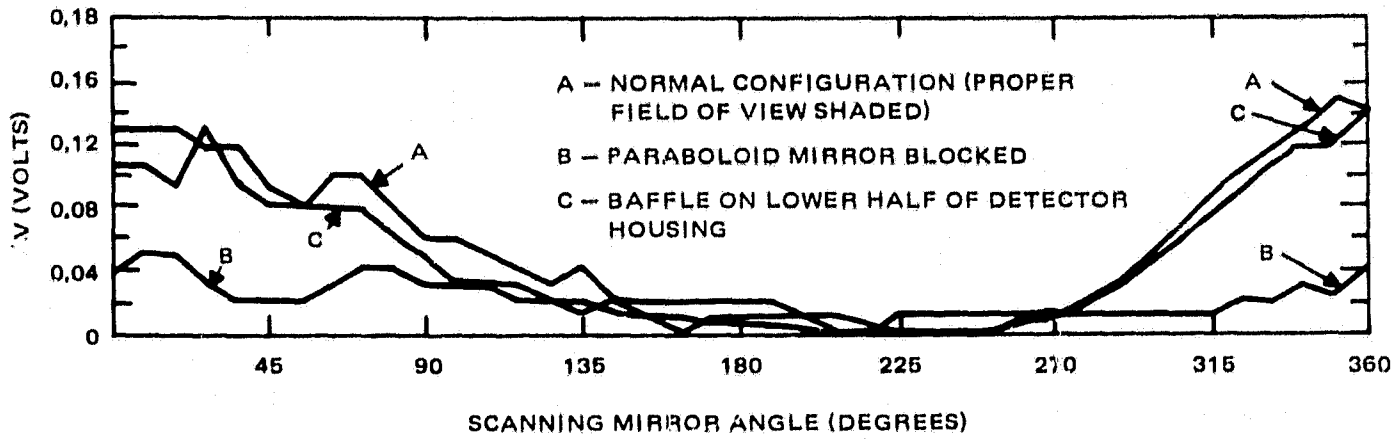



Figure 11. Comparison Plot of $\Delta V$ for Various Data Sets

of measurements, curve "B" in Figure 11, was taken with a blackened mask covering the paraboloidal mirror. Since the Sun Gun was so placed that most, if not all, of the specularly reflected light was reflected back out of the radiometer opening, it is apparent that most of the spurious signals observed in these tests resulted from light scattered by the scanning mirror. Furthermore, the substantial reduction in spurious signal level resulting from covering the paraboloidal mirror indicates that most of the stray light reaches the detector via this mirror. Although the paths followed by the light which produced the residual signals of curve "B" were not determined, reflection from the blackened mask is probably inconsequential, and most of the light must come from the walls of the radiometer. This is possible because, in the breadboard model used for the tests, the detector was shielded only against direct light from outside the radiometer and not against light from the walls.

Another set of measurements was made with a shield on the lower half of the detector housing intended to shield the detector from the radiometer walls. The results of these measurements are shown as curve "C" in Figure 11. The reduction in signal is not large but is approximately half the residual signal of curve "B," which supports the conclusion that most of the signal recorded in curve "B" results from light reflected from the walls.

In order to assess the amount of light scattered into the radiometer by the scanning mirror, a set of measurements was taken with the scanning mirror covered by white paper. These results are shown in Figure 12. The shape of the curve is similar to that of curve "A" in Figure 11, and the signals are somewhat more than 20 times as large, indicating that the brightness of the scattered light is close to 5 percent of the brightness that would be observed if the mirror were a perfect diffuser.

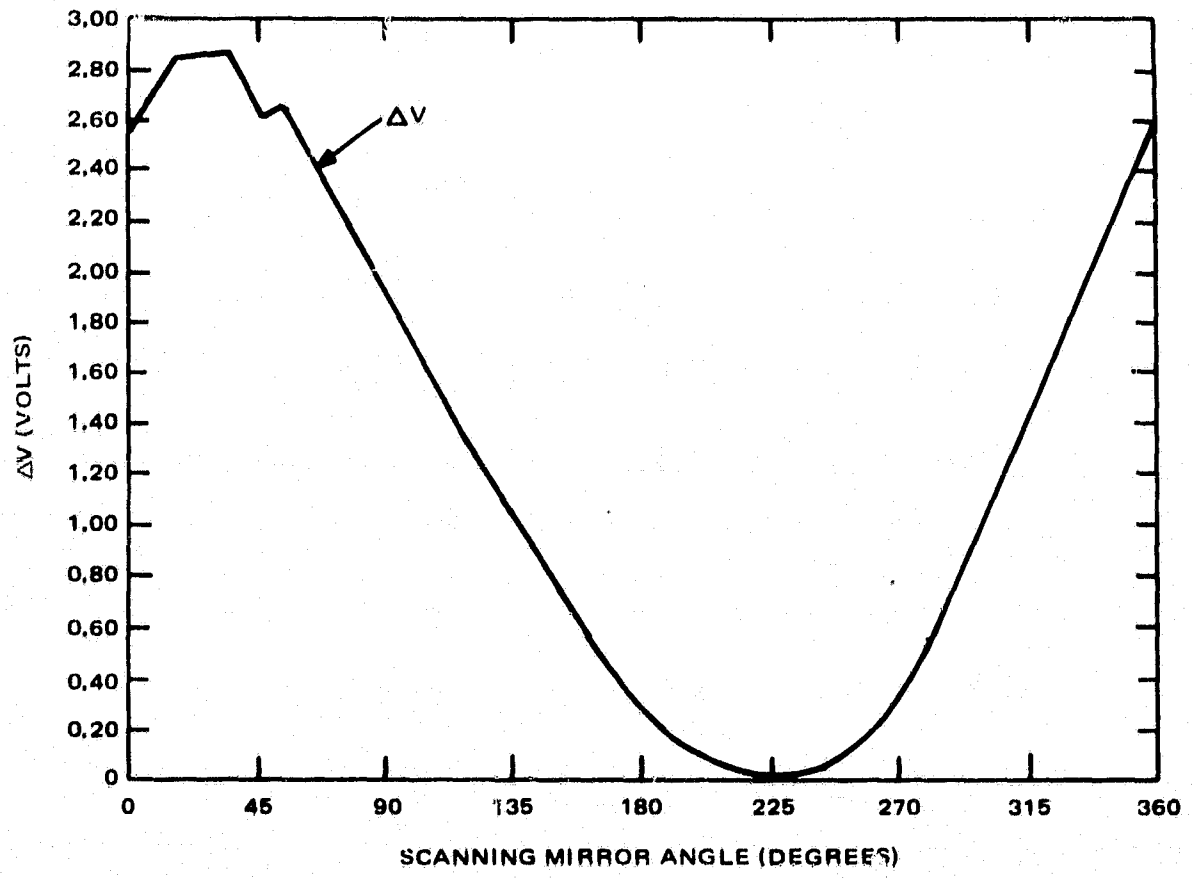



Figure 12. Response to Light Scattered From White Paper

One further test was made to determine the improvement which might be realized with a better scanning mirror surface since the surface of the scanning mirror used in these tests had deteriorated from laboratory use over a long period of time. A new mirror was placed on top of the radiometer mirror, and the result was a decrease in spurious signal of about 50 percent.

The following conclusions were reached on the basis of the tests described in the preceding paragraphs:

- Scattered light from the scanning mirror when sunlight is incident directly upon it may produce spurious signals as large as 2-3% of full scale in a radiometer designed for full scale output from bright clouds, even with a good quality scanning mirror surface.

- Most of the spurious signals result from light scattered directly into the optical system and cannot be eliminated without also eliminating the desired signal.

- Spurious signals which result from reflections from walls of the radiometer can be substantially reduced, if not eliminated, by use of internal baffles.

d. Sun Shade Design

The preceding conclusions indicate that the direct illumination of the scanning mirror by sunlight can produce excessive spurious signals in a high-performance radiometer, and that these signals can only be eliminated by preventing sunlight from reaching the scanning mirror. One solution to this problem is the use of sunshades which do not interfere with the scanning aperture during the period of active scan. Two general philosophies can be followed: to shield the radiometer opening from viewing anything but the earth (since the radiometer is earth-oriented); and to shield the radiometer opening from viewing in any direction where it might see the sun. In both cases, design of the sunshade is a straightforward, although

perhaps complex, geometrical problem. The principal difficulty which arises from this approach is that, because of the large aperture of the radiometer, the sizes of the required sun shades are impractically large. Furthermore, with the first philosophy, space observation for calibration and clamping level is eliminated, and with the second philosophy, it is impossible (in some orbits) to prevent direct viewing of the sun.

It should also be noted, however, that the earth itself will be a source of spurious signals. Although not very bright, the earth subtends a very large solid angle. Illumination on the earth side of the radiometer will be approximately 2/3 of the average of the product of reflectance and illumination in the area of the earth to which the radiometer is exposed. When the radiometer is directly over the subsolar point, for example, the illumination on the under side of the radiometer, for an average scene-reflectance of 30 percent, will be approximately 1/5 the illumination resulting from direct sunlight. This source of spurious signals is unaffected by the sunshades described in the preceding paragraph.

A technique for reducing spurious signals from both the sun and the earth consists of placing a "honeycomb" structure in the aperture of the radiometer in front of the scanning mirror. A sketch of this configuration is shown in Figure 13. The purpose of the honeycomb is to limit the angle between the scanning axis and the view angle from which light can fall directly on the mirror surface. This angle will be determined by the size of the honeycomb mesh and the thickness of the honeycomb. For example, if the honeycomb were 1-inch thick and the openings 1/8 inch in diameter, which is possible with readily available stock, the viewing angle would be 1/8 radian, or about 7 degrees, from the scanning axis, and the mirror would be shielded from direct radiation from sources more than 7 degrees off-axis. The configuration shown in Figure 13 has the added advantage that the interior of the radiometer is shielded from all radiation except that which passes through the honeycomb.

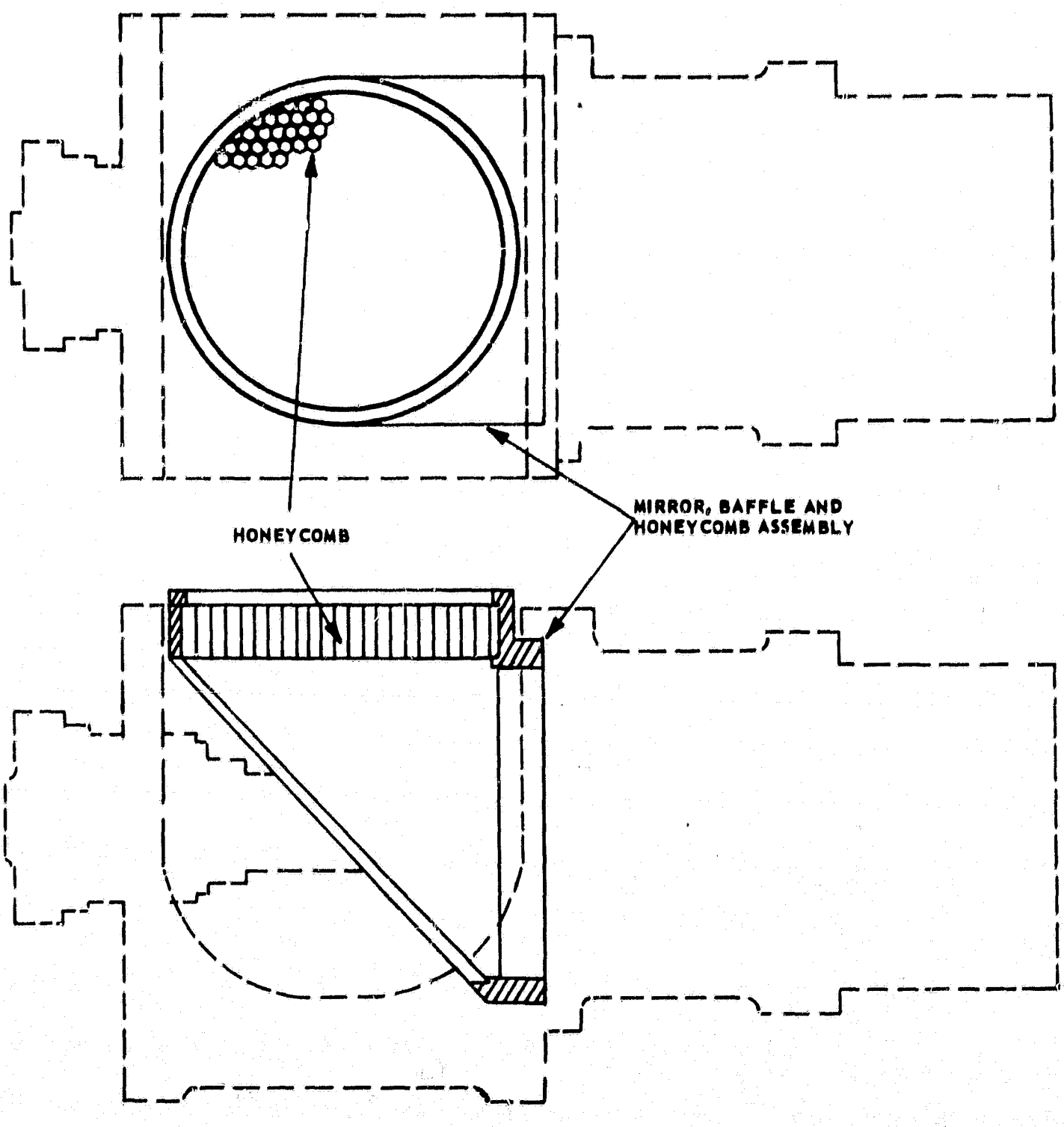



**Figure 13. Honeycomb Installation, Schematic Diagram**

A scanning mirror assembly incorporating the honeycomb shield was built and successfully tested. One further refinement of the stock honeycomb material used was necessary in order to provide effective shielding from off-axis radiation. Because of the finite field of view of the radiometer, the illuminated interior surfaces of the honeycomb will in turn illuminate the detector unless appropriate masking is provided. The geometry of the problem is shown in exaggerated fashion in Figure 14. If light from the area illuminated by off-axis radiation passes to the interior of the honeycomb within the cone of the radiometer field of view, it will reach the detector directly. The masking required to prevent this is shown in Figure A. The radiometer field of view in this case is a cone of appreciable sensitivity, and is somewhat larger than the field of view defined by the 50% response angle.

Masking as described in the previous paragraph was applied to a honeycomb structure and tested. The honeycomb used for the test had 1/4 inch openings and was 1-inch thick. These dimensions prevented direct illumination of the scanning mirror by sources more than approximately 15 degrees off-axis. Testing consisted of placing the Sun-Gun as close to on-axis as possible such that no light came directly through the honeycomb, first to one side of the axis and then to the opposite side, and observing the spurious signals with and without the honeycomb in place. On both sides of the axis the remaining spurious signal with the honeycomb in place was barely detectable (approximately 20 millivolts) in the most sensitive (log) mode of operation, and was substantial (approximately 2 volts) with the sunshade removed. Because of the nonlinearity of response in the log mode, the honeycomb attenuated stray light by a estimated factor of nearly 500. With the Sun Gun slightly further off-axis, spurious signals (with the honeycomb in place) were not detectable.

Several tests and analyses were carried out to determine the effect of the honeycomb on system response desired signal inputs. Theoretical analysis shows that for a "thin" honeycomb (that is, a flat mask having the shape of a cross section of the honeycomb perpendicular to the direction that light is traveling through the honeycomb), sine

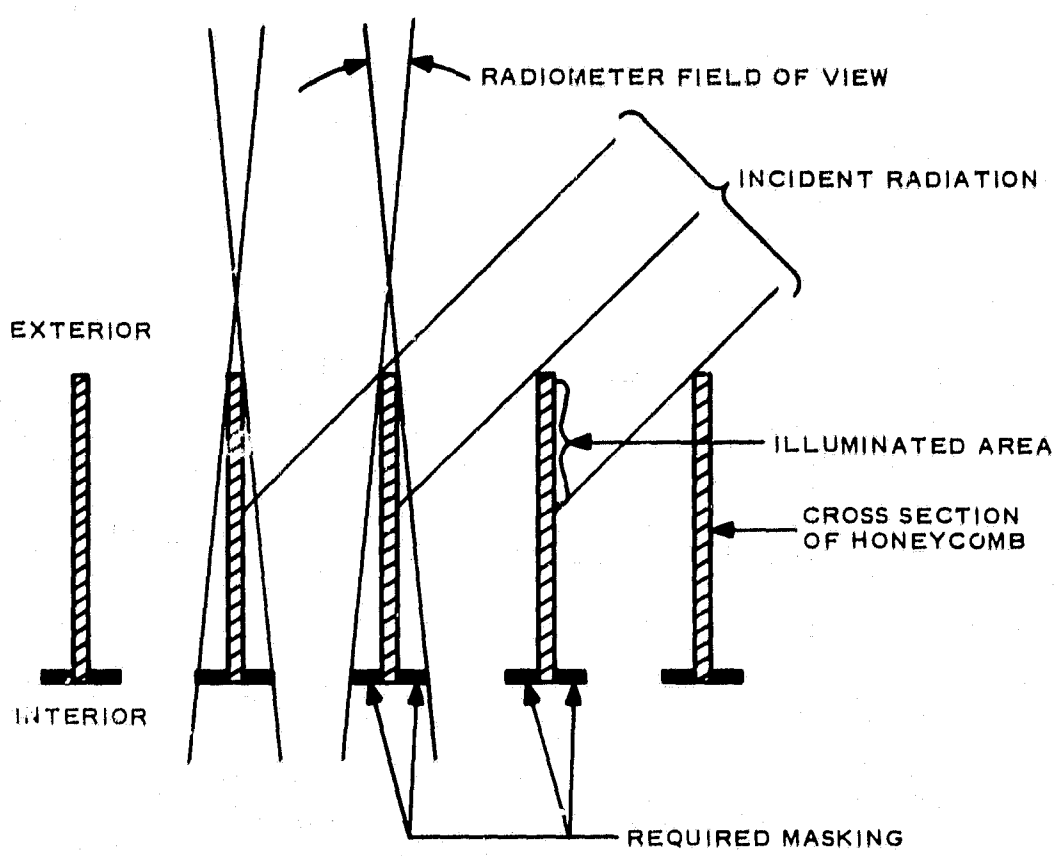



Figure 14. Honeycomb Refinement

wave response at almost all spatial frequencies is determined by multiplying the response without the honeycomb by a factor which is slightly larger than the square of the ratio of the clear area of the honeycomb to the total area of the honeycomb. For example, this ratio is 0.9 for a honeycomb which obscures 10% of the aperture area; the square of the ratio is 0.81; and response, therefore, at almost all spatial frequencies would be slightly larger than 0.81 times the response without the honeycomb. Exceptions occur in the form of narrow, sharp peaks at specific spatial frequencies for specific sine wave pattern orientations, and, in particular, at zero spatial frequency. The maximum of the peak at zero frequency is found by multiplying response without honeycomb by the unsquared ratio of clear area to total area of the honeycomb. The maxima at other peaks are found by multiplying response without honeycomb by a value no larger than the unsquared ratio and, of course, no smaller than the squared ratio. If the obscuration produced by the honeycomb is small, these peaks will have no practical significance.

The exact theoretical effect of honeycomb thickness has not been determined, but consideration was given to the question. Fresnel diffraction theory permits the determination of the distribution of the intensity and phase of radiation passing through the plane at the interior end of each individual cylinder of the honeycomb. These distributions have not been determined for the hexagonal honeycomb cylinders, but they will undoubtedly be similar to the corresponding distributions for a circular cylinder. The characteristics of the latter are that intensity and phase vary appreciably only in the vicinity of the periphery of the circle, with the scale of "vicinity" depending on the length of the cylinder and the wavelength of the radiation. In the present situation, for 10 micron radiation, the vicinity of the periphery of the circle will correspond closely to the size of the masks required at the interior ends of the cylinders. For visible radiation, the vicinity of the periphery will be much smaller than the required masks. The result is that within the open aperture at the bottom of each cylinder, the intensity and pahse of radiation will be nearly constant, and the theoretical effect of the honeycomb on sine wave response will be substantially the same as for a thin mask having the aperture pattern of the interior face of the honeycomb.

Experimental measurements were made. The field of view of the radiometer was measured with the aperture open, with the 1/4-inch honeycomb mentioned previously, and with a 1/8-inch honeycomb. The 1/8-inch honeycomb did not have the additional masking required for stay light protection. These field of view measurements are plotted in Figure 15. The scale of volts along the ordinate direction is of no particular significance for the separate measurements, but can be used to compare response with and without the honeycomb. If the three curves shown in Figure 15 are normalized for the same maximum value, the differences are scarcely perceptible. This leads to the conclusion that the radiometer field of view is not appreciably changed by the honeycomb.

Tests were also made using a 1-foot square heated plate as a target, unmasked to compare response at zero (or low) spatial frequency, and with bar pattern masks to compare response at high spatial frequencies. Target temperature was set at 150°C and

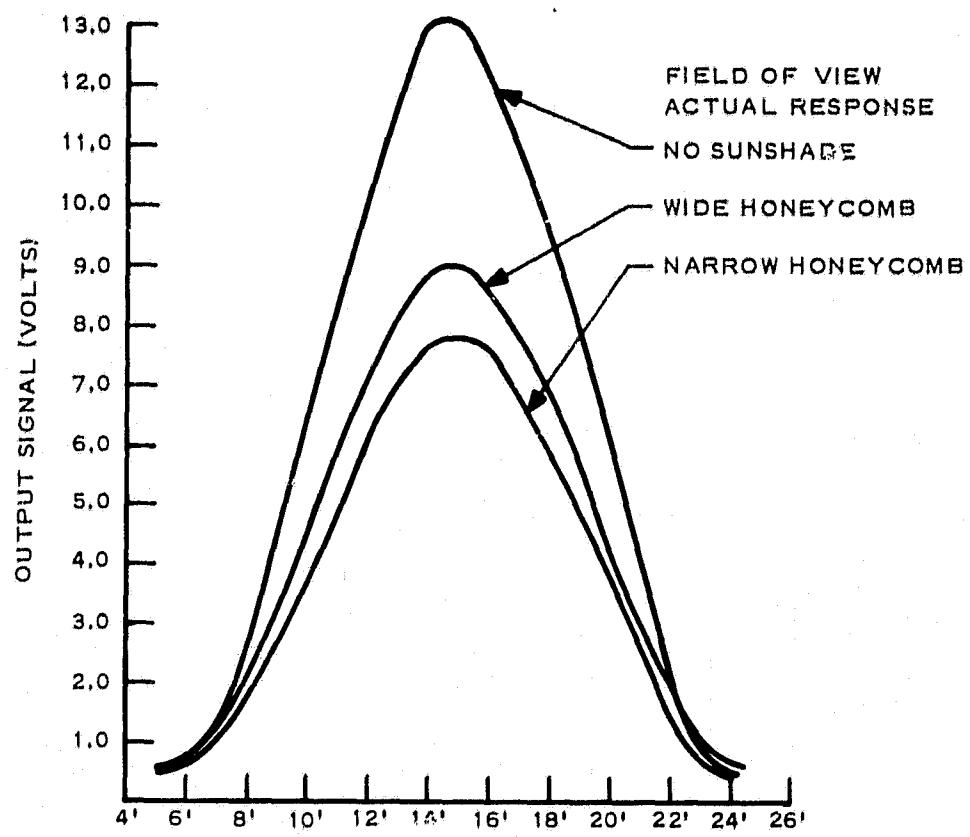



Figure 15. Field of View with and Without Honeycomb

measurments were made with the target at 40, 130, and 800 inches from the radiometer. Low frequency measurements were made with the motor drive on, and with the motor drive off (the scanning mirror moved by hand). High frequency measurements were made only at the 800 inch distance, since the target is out of focus at the shorter distances. Test results are summarized in Tables 2 and 3. Table 2 shows the effect of the honeycombs on low frequency response at the various target distances, and Table 3 shows the effect of the honeycombs at high spatial frequencies.

While the test results given in Tables 2 and 3 cannot be completely explained on theoretical grounds, some of the patterns evident in the data can be explained at least qualitatively. Theory predicts that at zero spatial frequency, response with the honeycomb will be reduced by the ratio of clear area to total area, but that at frequencies slightly greater than zero (with the low frequency boundary of the region depending

TABLE 2. EFFECT OF HONEYCOMB ON LOW FREQUENCY RESPONSE

| Target Distance | Scan | | No Honeycomb | 1/4" Honeycomb | 1/8" Honeycomb |
|---|---|---|---|---|---|
| 40" | By Hand | Response | 11.0v | 8.8v | 8.5v |
| | | % of Response with No Honeycomb | 100 | 80 | 77 |
| 130" | By Hand | Response | 11.0v | 9.1v | 8.2v |
| | | % of Response with No Honeycomb | 100 | 83 | 75 |
| | Motor Driven | Response | 10.5v | 8.0v | 7.8v |
| | | % of Response with No Honeycomb | 100 | 76 | 74 |
| 800" | By Hand | Response | 10.4v | 7.4v | 6.4v |
| | | % of Response with No Honeycomb | 100 | 71 | 62 |
| | Motor Driven | Response | 9.8v | 6.7v | 5.7v |
| | | % of Response with No Honeycomb | 100 | 68 | 58 |

TABLE 3. EFFECT OF HONEYCOMB ON HIGH SPATIAL FREQUENCIES

| Target Size | No Honeycomb | | 1/4" Honeycomb | | 1/8" Honeycomb | |
|---|---|---|---|---|---|---|
| | Response | % of Response to 12" Target | Response | % of Response to 12" Target | Response | % of Response to 12" Target |
| 12" | 9.8v | 100 | 6.7v | 100 | 5.7v | 100 |
| 3.2" | 3.3v | 33 | 1.7v | 25 | 1.4v | 25 |
| 2.3" | 1.0v | 10.2 | 0.5v | 7.5 | 0.35v | 6.1 |

upon honeycomb wall thickness and upon the wavelength of the radiation) response with the honeycomb will be reduced approximately as the square of clear area to total area. These relationships are shown in Figure 16.

Test results show that response with the honeycomb relative to response without the honeycomb decreases at the 12" target is moved away from the radiometer. However, as the target is moved away from the radiometer, the angle target subtends decreases and the spatical frequency content of the target (expressed in cycles per radian) will move to a higher frequency. Figure C shows that, at low frequencies, response with the honeycomb should decrease more rapidly than response without the honeycomb. Test result confirmed this. The frequencies involved also were consistent with the results. For the 1/8" honeycomb, painted wall thickness is about 0.008", and for the IR channel, $\lambda$ = 0.0004 inches; $t/\lambda$, therefore, is approximately 20 cycles per radian. The 12 inch target subtends an angle of 1/67 radian, and if this is taken to be one-half cycle of the dominant frequency, the dominant frequency is 33 cycles per radian.

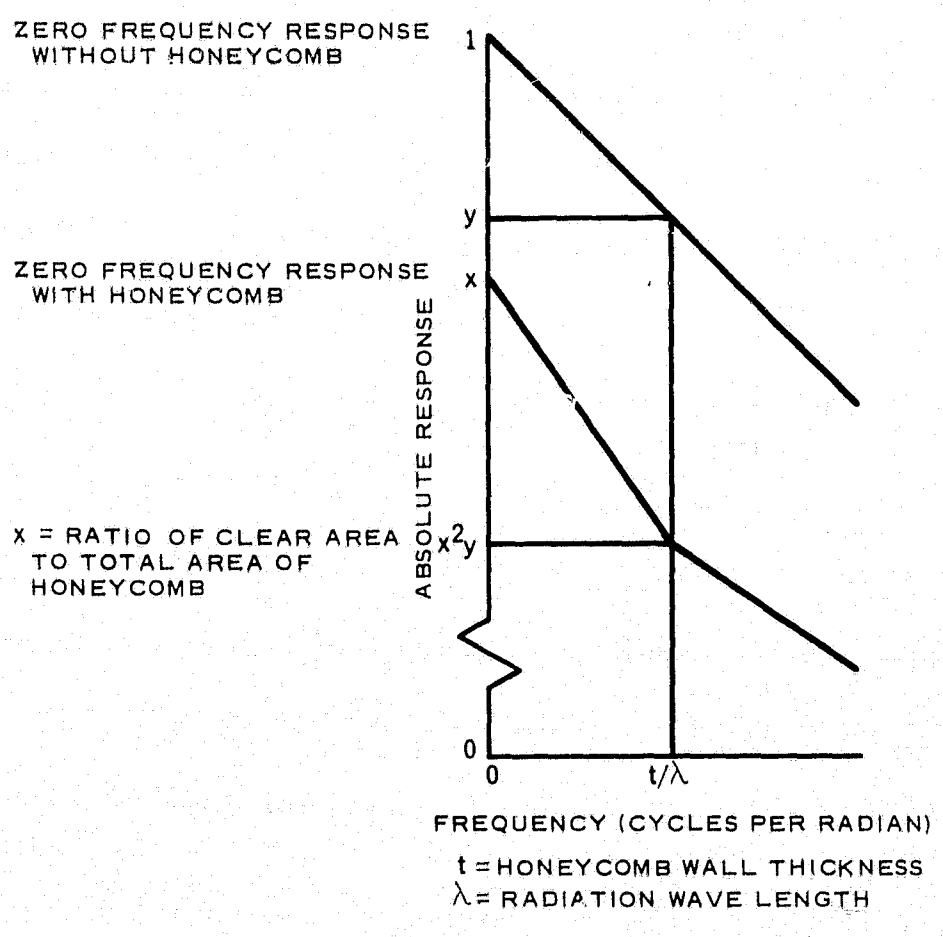



Figure 16. Approximate Modulation Transfer Function (MTF) with and Without Honeycomb

Test results also show that, at high frequencies, response relative to zero (low) frequency response is less with the honeycomb than without.

This again is consistent with the performance predicted by the plots in Figure 16 because of the peaked response at zero frequency with honeycomb which does not occur without the honeycomb.

Although the measured results cannot be fitted exactly to theoretical numbers, there is qualitative agreement. Considering the conditions under which data was taken (particularly the problem of optimum orientation of the honeycombs) the performance theory as described appears to be experimentally verified.

e. In-Flight Radiometric Calibration

Provisions have been made for in-flight calibration of both channels at the upper and lower ends of the scales of radiation input. For both channels, the lower calibration level will be established when the scanning axis is pointing into space a few degrees beyond the earth's horizon.

The upper calibration level for the infrared channel is established when the aperture of the radiometer is completely filled by the base of the scanning mirror casting (i.e., when the scanning axis is pointed towards, and perpendicular to, the radiometer base). The casting surface scanned by the radiometer has been grooved as well as blackened to increase the apparent emissivity. The included angle between the sides of the grooves is 30 degrees, and the surface has been painted with 3M black velvet paint which has an emissivity of about 0.95. The apparent emissivity of the surface should be somewhat greater than 0.98. Two thermistors have been attached to the outer surface of the casting to provide the temperature information necessary for calibration of the channel.

The upper calibration level for the visual channel is provided by a small collimator attached to the outside of the scanning mirror housing as shown in Figure 17. The collimator consists of a 1-inch square off-axis section of a Mangin mirror and a miniature incandescent lamp with its filament located at the focal point of the mirror. The calibration pulse occurs when the scan axis is parallel to the collimator axis and the reflecting side of the mirror faces the collimator; therefore, the pulse occurs outside the active scan interval. The lamp is an 8-volt lamp, voltage regulated to operate at approximately 6.5 volts. Final adjustment of the lamp voltage is made during visual channel calibration to produce a signal level corresponding to the 10,000 foot-lambert level. The power requirement for the lamp is approximately 1 watt; however, this is not considered excessive because the channel does not require frequent calibration.

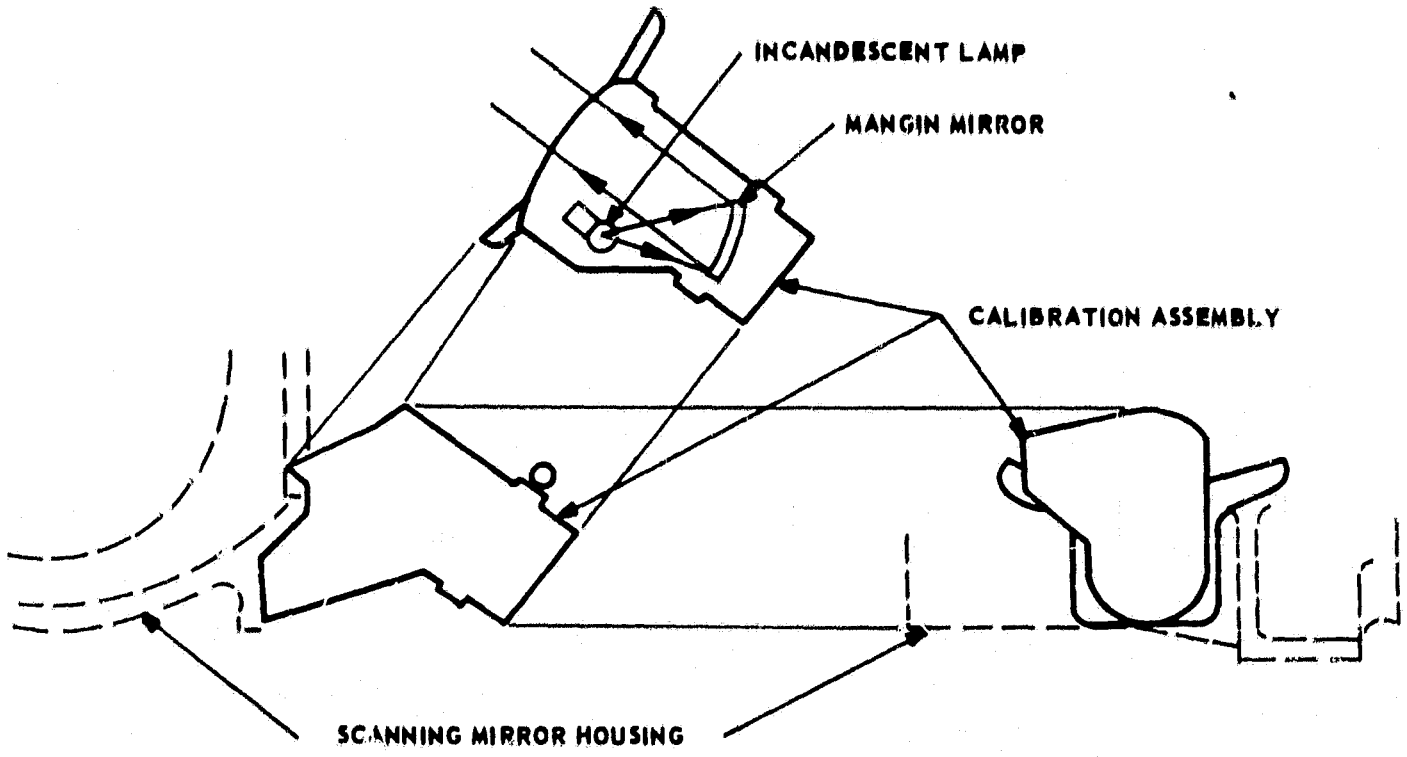



Figure 17. Visual Channel In-Flight Calibration Assembly

2. Radiometer Electronics

a. Low-Noise Preamplifiers

In general, the impedances of detectors extend from a few ohms to several hundreds of megohms, and their outputs are usually microvolts or nanoamperes. The primary purpose of a preamplifier is to increase the detector signal level to a usable magnitude without degrading the available signal-to-noise ratio. Therefore, the most important characteristic of such a preamplifier is its noise performance. The criteria used in selecting an amplifier of low-noise design to maximize the signal-to-noise ratio are described in the following paragraphs.

(1) Sources of Amplifier Noise

Amplifier noise sources are: (1) thermal noise; (2) shot noise; (3) 1/f noise; and (4) generation-recombination (G-R) noise. Of the four sources, only thermal noise and 1/f noise are significant.

Thermal noise (or Johnson noise) is characterized by the expression

$$e_{nj} = \sqrt{4kTBR} \tag{1}$$

where

k is Boltzmann's constant,

T is the absolute temperature (°K), and

R is the equivalent noise resistance of amplifier.

The equivalent noise bandwidth (B) is defined as

$$B = \frac{1}{A_o^2} \int_0^\infty A^2(f)df \tag{2}$$

where

$A_o^2$ is the peak voltage gain squared

and

$A^2(f)$ is the voltage gain as a function of frequency squared.

The noise power spectra is "flat" (i.e., the w/Hz is constant).

$$\frac{e^2_{nj}}{B} = 4kTR \text{ w/Hz} \tag{3}$$

The 1/f noise (or flicker noise) is a low frequency phenomenon. It may be characterized as

$$e_{nf} = k \int_{f_\ell}^{f_H} \frac{1}{f} df \tag{4}$$

where

k is a constant,

$f_\ell$ is the low-frequency limit, and

$f_H$ is the high-frequency limit.

Theoretically, $f_\ell$ has been shown to approach zero Hz and $f_H$ is approximately 50 Hz for field-effect-transistor (FET) amplifiers, and 500 Hz for bipolar transistor amplifiers. The term $f_H$ is the frequency at which the 1/f noise value equals the thermal noise value.

A plot of amplifier noise vs frequency is shown in Figure 18. The amplifier noise performance is measured by noise figure (NF) in db. That is,

$$NF = 20 \text{ Log } \frac{e_{ai}}{e_{nj}} \qquad (5)$$

where

$e_{ai}$ is the output amplifier noise reflected to the input

and

$e_{nj}$ is the thermal noise of the amplifier source resistance.

An ideal noiseless amplifier would have a NF of unity.

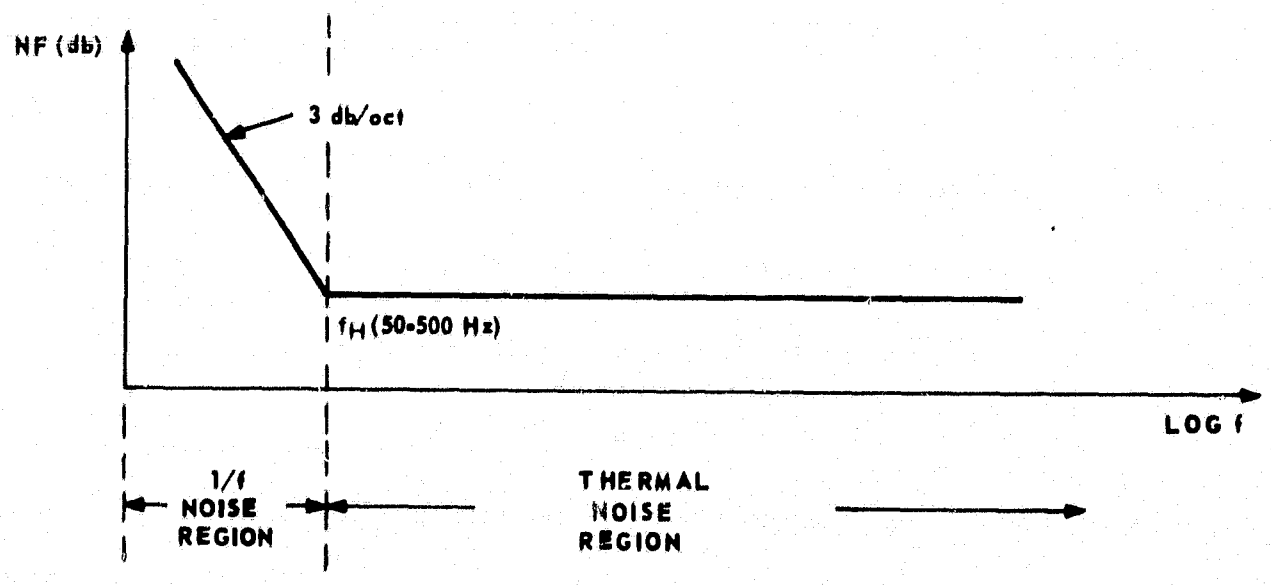



Figure 18. Amplifier Noise Spectrum Versus Frequency

(2) Amplifier Design

Low-noise preamplifiers can be designed using either bipolar or field-effect-transistors. These can be used either as discrete components or as part of integrated

or hybrid operational amplifiers. The choice of a bipolar transistor or an FET for low noise amplifier performance primarily depends upon the following three factors:

1) Detector impedance (source impedance),
2) Frequency range of interest, and
3) Bias considerations.

The effect of source impedance on amplifier noise performance (NF), for a bipolar transistor and an FET front end is illustrated in Figure 19. The NF of a cascade of amplifier stage is

$$F_o = F_1 + \frac{F_2}{G_1} + \frac{F_3}{G_1 G_2} + \cdots \frac{F_n}{G_1 G_2 \cdots G_{n-1}} \qquad (6)$$

where

NF is equal to 10 Log $F_o$

and

$G_n$ is the power gain of the nth stage.

Thus, the first stage of amplification determines, to a good approximation, the overall NF of the cascade.

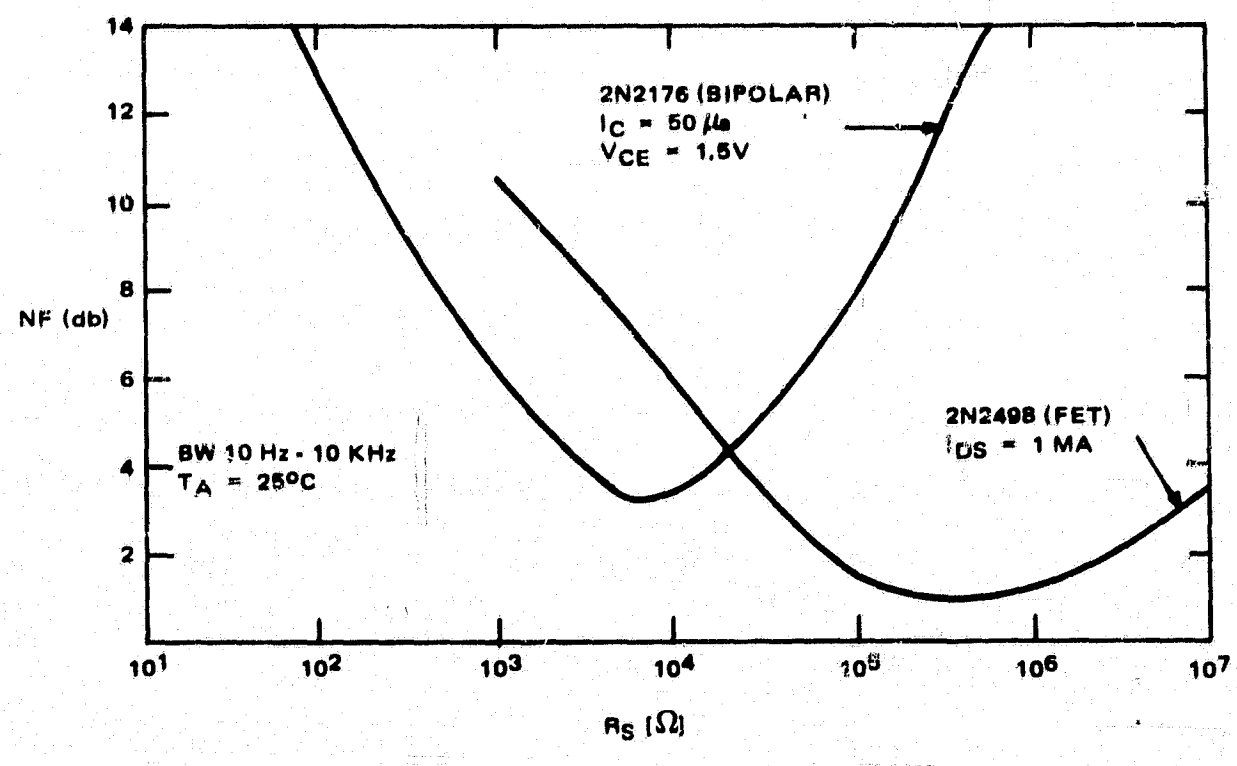



Figure 19. Broadband NF vs Source Resistance for a Typical Low-Noise Bipolar Transistor and an FET Amplifier

The data in Figure 19 indicate that an FET should be used in any preamplifier design when the source impedance exceeds 50 kilohms. Conversely, a bipolar transistor should be used when the source impedance is less than 50 kilohms to minimize the NF.

The bias-current level, in the FET design has a negligible effect on the position of the minimum in Figure 19. However, in the bipolar design this is not the case. as illustrated in Figure 20.

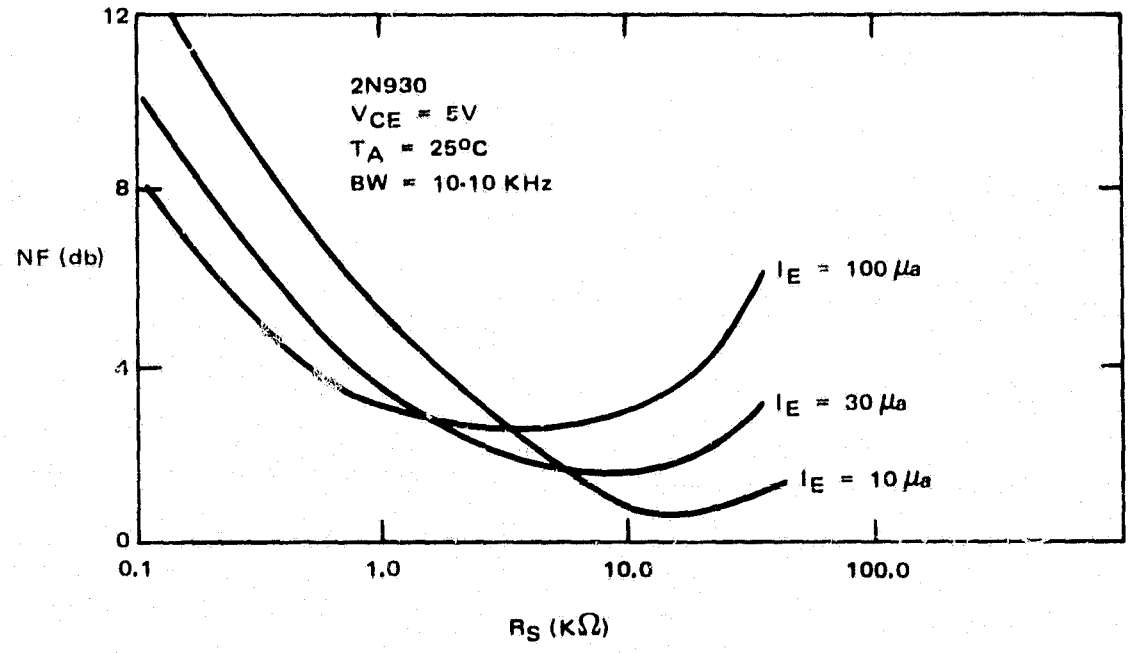



Figure 20. Broadband NF vs Source Resistance for a Bipolar Transistor as a Function of Bias Current

The lower the emitter bias current, the higher the source resistance at which the minimum NF is achieved. Although it seems that the emitter current can be decreased until the bipolar transistor NF approaches that of an FET for high source resistances, it must be remembered that the transistor is temperature and radiation sensitive for low values of emitter current.

Another criteria used in the selection of either a bipolar or FET transistor is the frequency region of operation. If the amplifier is to be operated entirely in the thermal noise region or with a wide bandwidth (greater than 2.0 kHz) the preceding criteria for selection will suffice. If the amplifier is to be operated in the 1/f noise region (see Figure 18), then NF characteristics must be carefully examined to determined whether an FET operated at a source resistance less than 50 kilohms is quieter than a bipolar transistor.

(3) Sample Design

The preamplifier in the IR channel is a good example of low noise design. It uses a Philbrick Q25AH hybrid operational amplifier which has an FET input transistor pair. The source impedance of the bolometer is approximately 100 kilohms at ambient temperature and increases with decreasing ambient temperature. The laboratory data of spot NF vs frequency for this amplifier is shown in Figure 21.

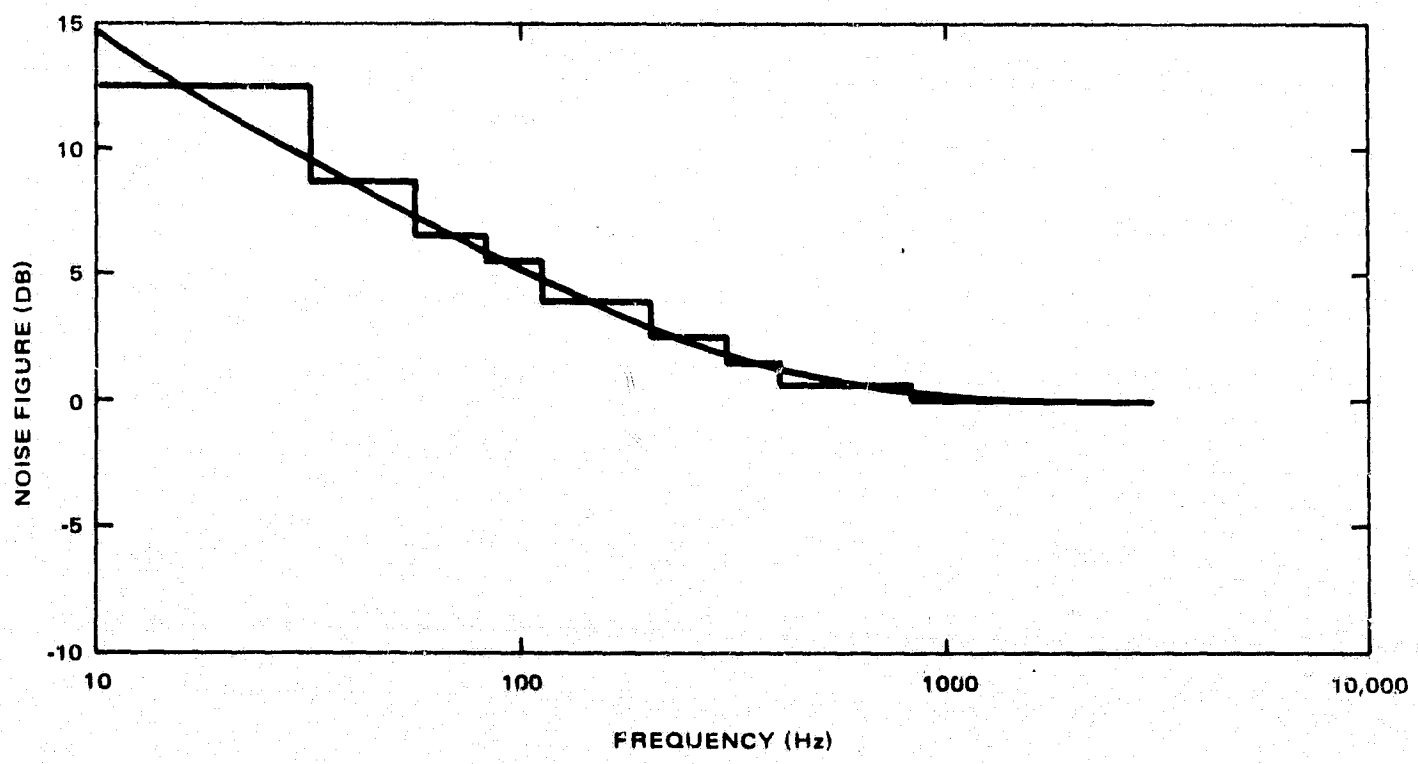



Figure 21. Spot NF vs Frequency for the IR Channel Amplifier

The measurements were taken using a wave analyzer with a 6 Hz bandwidth. The wideband noise figure (NF) was then calculated from the data numerically, using the following relationship.

$$NF = \frac{\ell}{BW} \sum_{N=0}^{\ell} NF_n (\Delta f_n) \qquad (7)$$

where

NF is the wideband noise figure,

BW is the total noise bandwidth = 4 kHz,

$NF_n$ is the noise figure in a bandwidth $\Delta f_n$,

$\Delta f_n$ is the bandwidth of a segment of the curve, and

$\ell$ equals 6.

The NF was calculated to be 0.55 db. This result compares favorably with the theoretically expected result of 0.2 db.

(4) Bolometer-Preamplifier Interface

The development of the infrared electronics was complicated because of the difficulty in successfully interfacing the preamplifier with the thermistor bolometer given certain inherent detector limitations. These detector limitations are:

- Presence of a large d-c bias component which masks the signal and makes direct coupling required for good low frequency response difficult.

- Slow response time constant-typically no faster than 1 millisecond.

A typical bolometer bridge circuit is shown in Figure 22. The bolometer consists of two thermistor flakes; one shielded from infrared, the other exposed to the focused infrared energy from the scene. The infrared energy absorbed in the active flake causes a small change in the flake resistance while no resistance

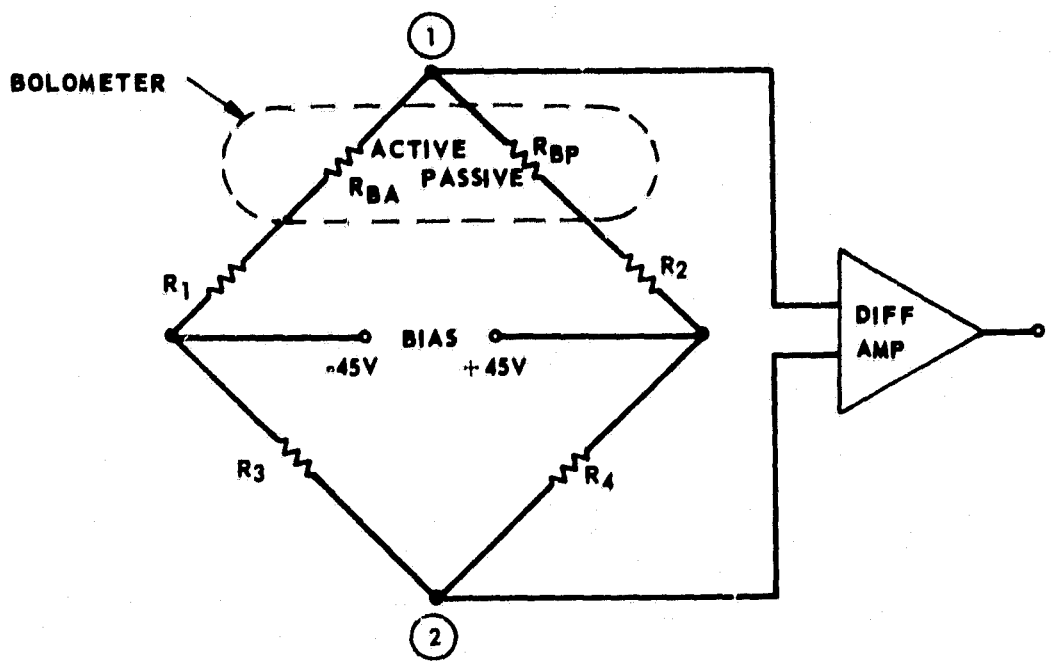



Figure 22. Basic Bolometer Bridge Circuit

change occurs in the passive flake. This resistance change is sensed by applying a fixed bias voltage on the bridge and measuring the signal produced by the unbalanced bridge. Ideally, if $R_1 = R_2$, $R_{BA} = R_{BP}$, and $R_3 = R_4$, the voltage at points 1 and 2 will be equal (in the absence of an infrared signal) and the output of the differential amplifier will be zero; a change only in $R_{BA}$ due to the infrared signal will produce an unbalance and will be amplified as signal. In practice, however, the resistors do not remain matched, and the bridge will be unbalanced for dc. $R_{BA}$ and $R_{BP}$ for a good bolometer can track to about 4 percent over a temperature range of -10° to +60°C, and can be tailored to track better than 0.25 percent using external temperature sensitive elements. Under conditions of 0.25 percent bolometer tracking, the bridge of Figure 22 will have a d-c unbalance of about 60 millivolts while the true signal from the bolometer due to the scene is about 1 millivolt maximum. Obviously, with a signal-to-dc noise ratio of 1/60, simple direct coupling of the bridge to the amplifier will be impossible because the amplifier will saturate on d-c and the zero reference will be lost. Response down to almost d-c in the amplifier is essential because the low-frequency cutoff requirement for this radiometer is about 0.025 Hz.

Methods for overcoming the inherent problem of separating the signal from the bias error while still maintaining near d-c response are:

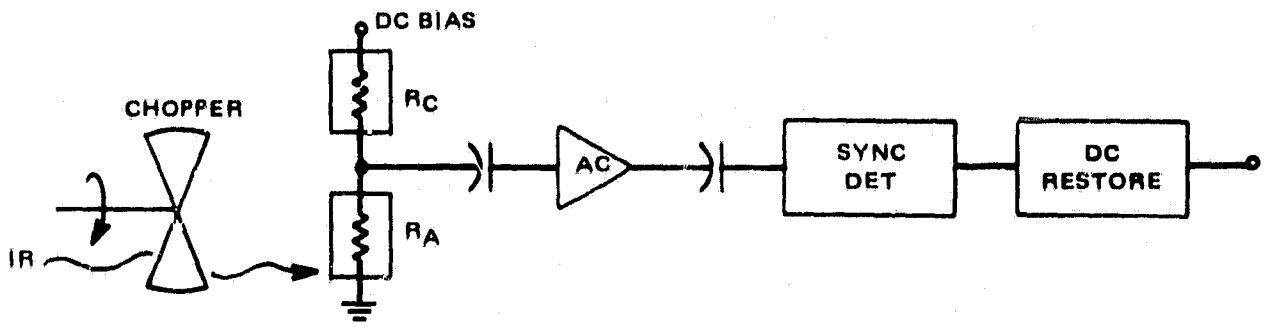
- Optical chopping,
- A-c bias,
- Capacitor coupling, and
- D-c coupling with clamp feedback as used in this radiometer.

These methods are shown schematically in Figure 23.

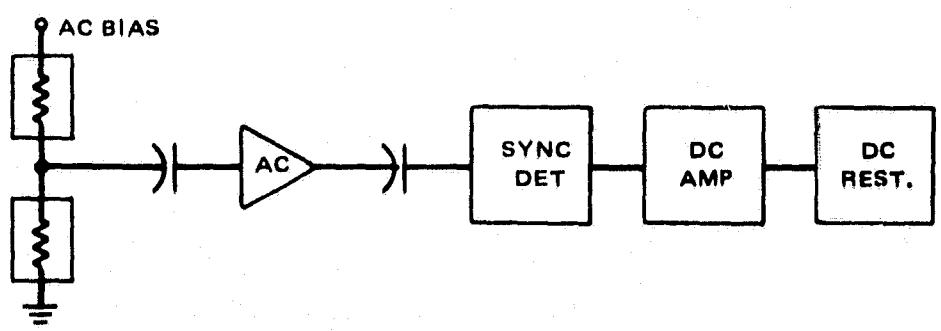
Optical chopping is a very inefficient method for overcoming the d-c bias problem. The incoming radiation must be chopped at least twice the highest frequency of the signal with the result that the time constant limitation of the bolometer is a factor for all signal frequencies down to d-c. Also, the mechanical requirements of the chopping blade represent at an undesirable addition to the radiometer.

In the a-c bias method, a high frequency bias is substituted for the d-c bias, and the bridge can be coupled to the amplifier with small capacitors. No improvement is made in the bridge unbalance over the d-c bias case and only a modest amount of gain can be employed before the signal is detected. Furthermore, the complexity and additional power drain of the a-c bias supply are undesirable. The only reason for using a-c bias is to reduce the effects of 1/f noise in the amplifier, because a-c bias translates all the signal frequencies outside the 1/f noise spectrum.

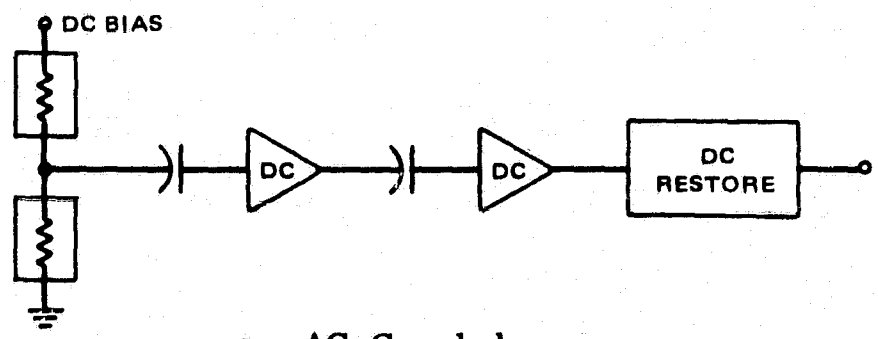
If capacity coupling is used, the time constant required for the 0.025 Hz low-frequency cutoff results in large, unwieldy capacitor values. Also, the droop associated with many RC time constants in series in the infrared electronics could result in the loss of calibration accuracy. The need to keep RC elements at a minimum makes it undesirable to use the bridge in a balanced fashion, thereby reducing the possibility of employing common-mode rejection of detector bias supply noise.



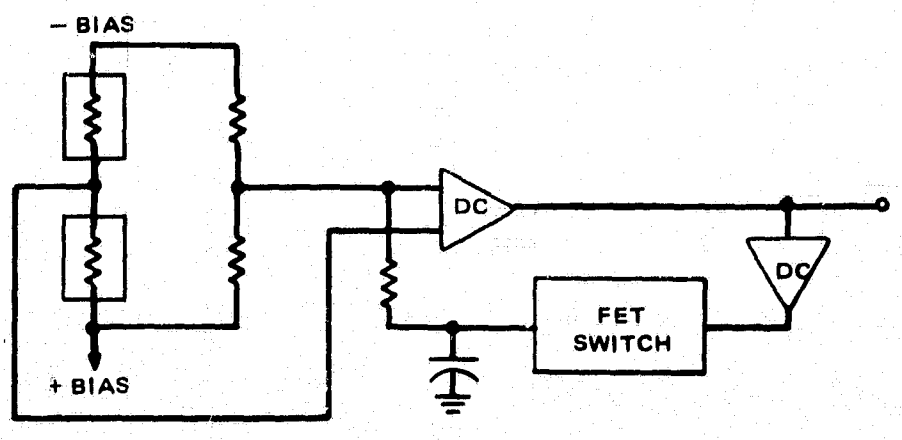

a. Optical Chopping




b. AC Bias




c. AC Coupled




d. Clamp Feedback

Figure 23. Bolometer-Amplifier Coupling Methods

The detector amplifier coupling scheme used for this radiometer avoids the objections of the foregoing methods and represents one of the most important features of the radiometer electronics. This method is described in detail later in this report.

Compared to photon detectors, thermistor bolometers are characterized by very slow response. At best, bolometers have time constants of about 1 millisecond, while photon detectors are faster than 1 microsecond. The bolometer used in this radiometer has a time constant of 2 milliseconds; a plot of its frequency response is shown in Figure 24.

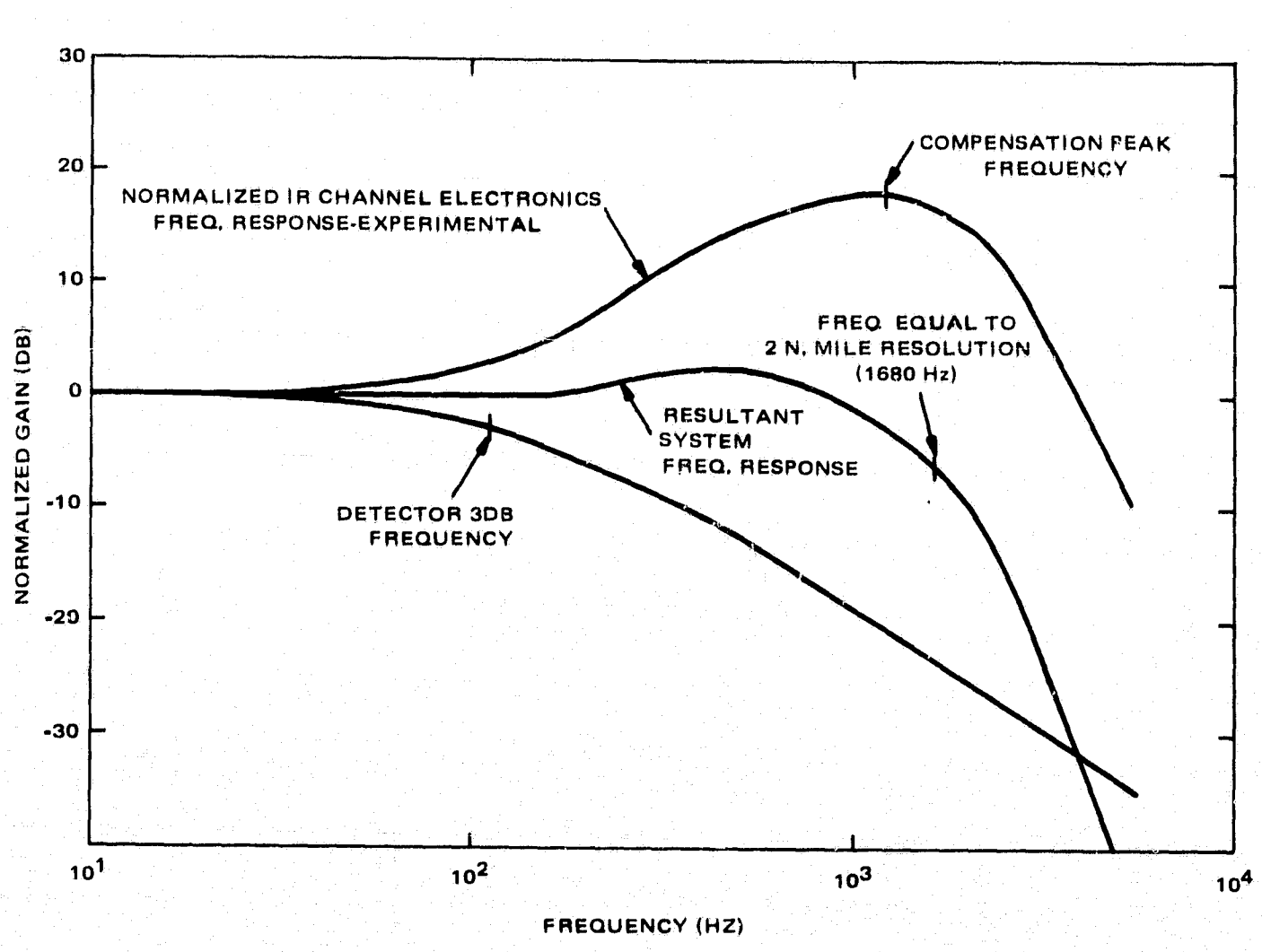



Figure 24. Infrared Channel Response Curves

The upper limit of the information band is 1650 Hz, and frequency compensation must be used to obtain uniform amplitude for all scene element sizes. The frequency characteristic is actually compensated for 50 percent electrical response as shown in Figure 24 to trade off good spatial resolution with usable NE$\Delta$T. The result of this high frequency compensation is a signal-to-noise ratio about 20 db worse than that available from a radiometer using a fast detector. Because of this severe noise penalty using a thermistor bolometer, the use of the lowest noise preamplifier available becomes extremely important. The investigation and use of amplifiers with noise figures of approximately 0.5 db in this radiometer helps achieve good NE$\Delta$T with 2-mile spatial resolution. A detailed description of the amplifiers is given later in this report.

b. Infrared Channel Signal Electronics

(1) Introduction

The infrared energy from the scene is directed onto the detector by the optics. The infrared detector is a thermistor bolometer biased in a bridge configuration. The bridge offers the advantage of strong common-mode rejection of detector power supply noise. The signal output of the bolometer bridge is direct-coupled to the detector preamplifier. The other bridge output (designated common-mode output) is direct-coupled to the common-mode amplifier.

The detector preamplifier is a low-noise stage with 0.5 db noise figure. In addition, the amplifier is boosted at the high frequencies to compensate for the roll-off of the slow detection time-constant.

The signal from the detector preamplifier is direct-coupled into the post amplifier and low-pass filter. These stages amplify the signal level and increase the cutoff rate of the overall system frequency response, respectively.

The signal from the active filter is sent through several control gates and a signal buffer before it finally appears at the output. The purpose of these gates is to insert into the IR signal a line sync pulse and staircase voltage calibration signal. In addition, during the time that these signals are inserted, a control gate blanks the IR signal output. These gates are activated by appropriate commands from the logic. The output of the signal buffer is designated the composite IR signal output because it contains both IR signal information and sync and calibration signals.

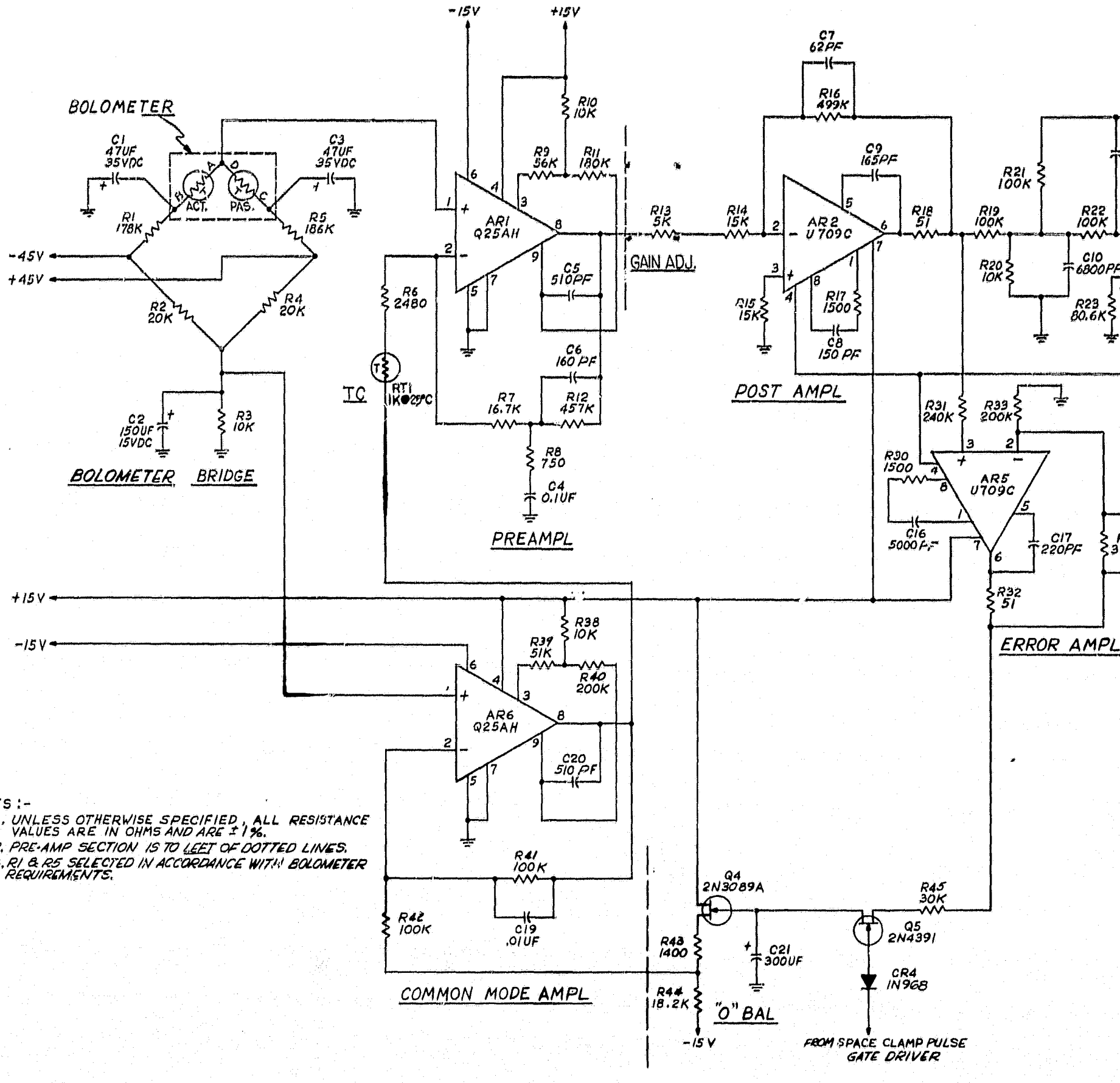
As discussed previously, it is desirable that the signal path from the bolometer to the output be direct-coupled. To achieve this result, a d-c stabilizing feedback loop from the post amplifier output to the detector preamplifier input, is included in the design. This loop maintains the output of the IR channel very near 0 volt d-c with variations in ambient temperature.

The design of the IR channel signal electronics, shown in Figure 25, is a major advance in the state of the art of low noise, direct-coupled, high-gain amplifiers primarily because of this feedback loop technique of d-c stabilization.

The feedback loop operates as follows. The d-c voltage level at the output of the post amplifier is compared to ground (0 volt) and the difference voltage is amplified by the drift-error amplifier. The bandwidth of the drift-error amplifier is restricted to approximately $1 \times 10^{-3}$ Hz in order to amplify only the d-c error.

The d-c error is fed into the space-clamp gate, which is essentially a series switch. The gate is activated by the logic. It is normally open and is commanded closed for a 12-millisecond period during the portion of the mirror scan when the optics are viewing space. During this time, the d-c output of the post amplifier should be zero. If it is not, the resultant error signal is amplified and sent through the closed gate to the space clamp memory and buffer.

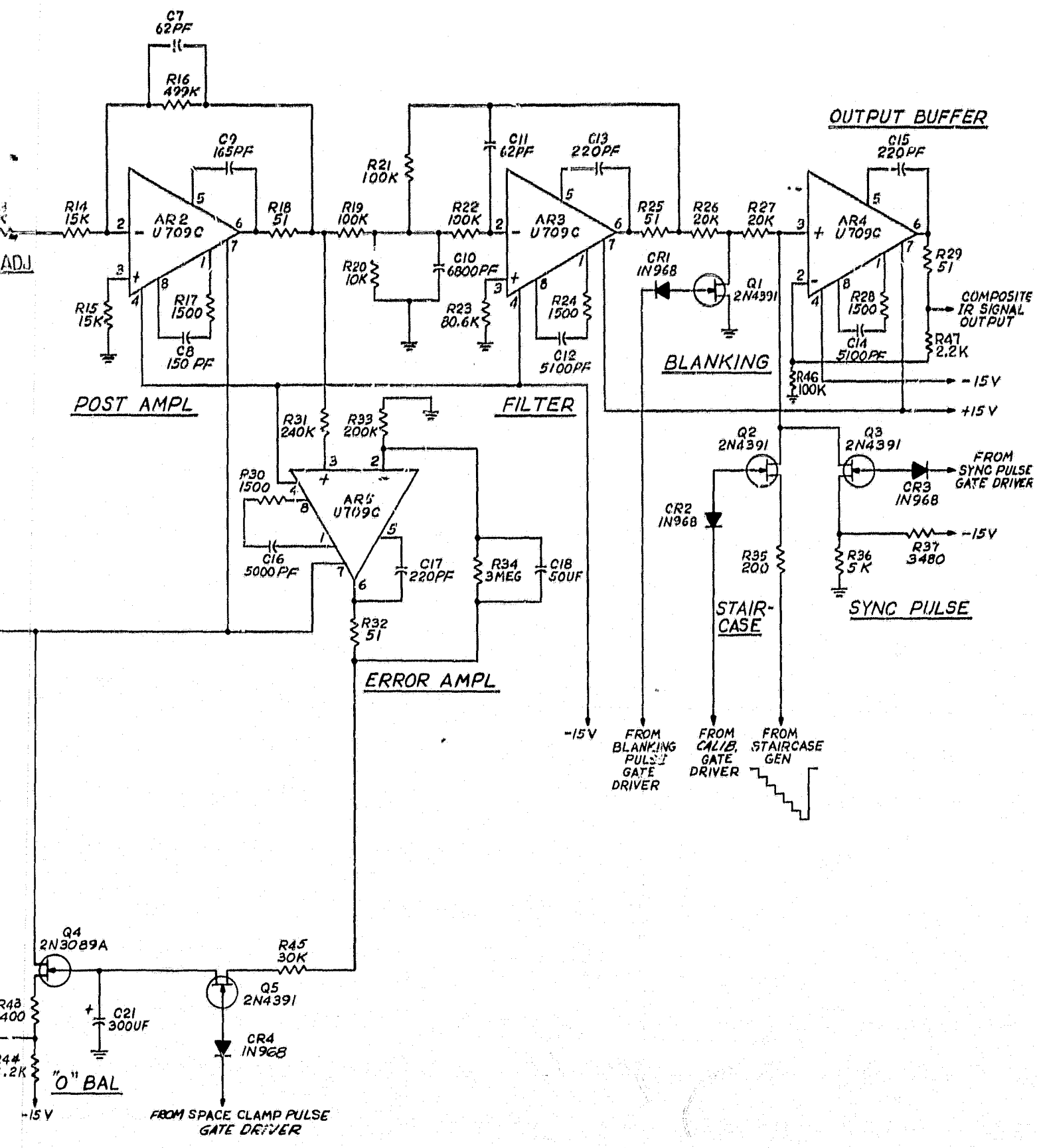
The space clamp memory consists of an ultralong time-constant capacitor network with a storage-time constant of approximately 100 seconds. The error signal is stored




NOTES :-

1. UNLESS OTHERWISE SPECIFIED, ALL RESISTANCE VALUES ARE IN OHMS AND ARE ± 1%.
2. PRE-AMP SECTION IS TO LEFT OF DOTTED LINES.
3. R1 & R5 SELECTED IN ACCORDANCE WITH BOLOMETER REQUIREMENTS.

Foldout #1




Fallout #2

**Figure 25. IR Channel Signal Electronics, Schematic Wiring Diagram**

in the memory. Its magnitude is re-established or readjusted every time the space clamp gate closes during the 12 milliseconds the radiometer views space.

The common-mode amplifier has two inputs: one from the memory and one common-mode output from the side of the bridge. This amplifier is designed to have unity gain. The output of the common-mode amplifier which consists of the d-c error signal and the bridge common-mode supply noise is presented to an input of the detector preamplifier.

The voltage difference, $V_D$, between the two detector preamplifier inputs is adjusted, by the above feedback technique, to a value which causes the output of the IR Channel to be clamped to 0 volt when the signal is not present.

Let

$$V_D = \left(E_s + E_{cm} + E_B + E_A\right) - \left(E_{FB} + E_{cm}\right) \qquad (8)$$

where

$E_s$ is the signal voltage from the bolometer

$E_{cm}$ is the bridge power supply common mode noise

$E_B$ is the bridge impedance error due to bolometer thermal tracking

$E_{FB}$ is the error signal from the feedback loop

Also,

$E_A$ is the thermal drift in the amplifiers referred to the input of the preamplifier.

$$E_{FB} = E_B + E_A \qquad (9)$$

Adding equations (8) and (9),

$$V_D = E_s \tag{10}$$

Equation (10) demonstrates that the feedback effectively cancels both the bridge d-c unbalance error and the thermal drifts in the d-c amplifiers.

A closer look at the feedback loop shows how this is accomplished. The signal path from detector input to output has a gain, G. The feedback error path has a gain, H, when the space clamp switch is closed. Since the preamplifier input voltage difference, $V_D$, is dependent upon stored memory error voltage, the closed-loop d-c gain, T, of the system is the same with the feedback loop opened or closed. Therefore,

$$T = \frac{G}{1 + GH} \tag{11}$$

If G is equal to 4500 and H is equal to 15, then

$$T = \frac{1}{H} = \frac{1}{15} = 67 \times 10^{-3} \tag{12}$$

Thus, if the bolometer input drift plus amplifier drift equals 1 volt, then the output will vary by only 67 millivolts. Breadboard tests have verified this predicted performance. This feedback technique is valid only for slowly changing ambient temperatures because of the loop time constants, as is the case in a typical satellite environment.

Reference to Figure 25 shows that the d-c feedback does not encompass the active filter and signal buffer. Although these stages are not included in the loop, the d-c stability of the system output is not compromised because the d-c gains of these stages are unity, and the expected thermal drifts are below the system output noise level.

(2) Detailed Description

The following discussion is based on the IR channel signal electronics schematic diagram shown in Figure 25.

The bolometer bridge consists of a two-flake thermistor bolometer (shown in the dotted section), five resistors and three capacitors. The detector has a 2 millisecond time constant, a peak voltage of 30 volts, and a responsivity of 1920 volts/watt at 0.6 peak voltage. Each flake is in series with a resistor (R1 or R5). These resistors serve a three-fold purpose: they adjust the flake bias voltage to 0.8 peak voltage; they prevent the possibility of accidental thermal runaway; and, most important of all, they maintain the bias across each flake at 0.7 peak voltage at all temperatures between -10° and +60°C. The signal output of the bridge is taken between the two flakes of the bolometer.

The other side of the bridge is formed by resistors R2, R3, and R4, which provide the necessary common-mode output. Capacitors C1, C2, and C3 filter high-frequency power supply noise.

The detector preamplifier uses a Philbrick model Q25AH amplifier in its design. This device is a low noise, high input impedance (FET input) operational amplifier An appropriate feedback network around the device provides a d-c gain and the frequency characteristics shown in Figure 26.

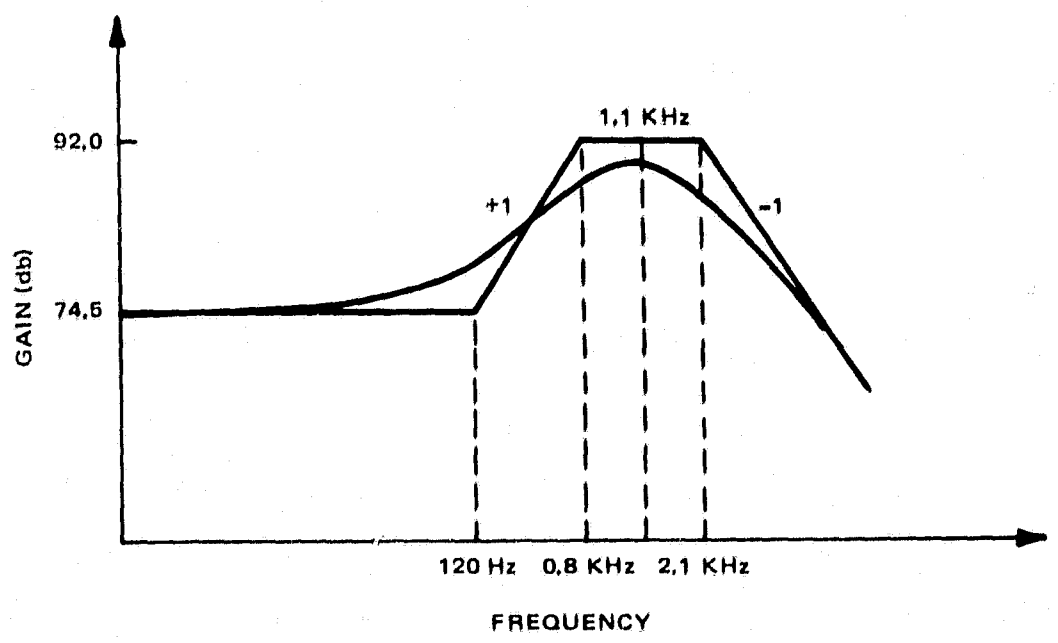



Figure 26. Frequency Response Characteristics of IR Channel Preamplifier

The peaking network is shown in Figure 25. Resistor R6 and thermistor RT1 provide compensation of the IR channel gain for changes in bolometer responsivity with temperature. Stability of the preamplifier is assured by careful feedback design and by capacitor C5.

The post amplifier, being less critical with respect to amplifier noise, uses a Fairchild $\mu$A709 integrated-circuit operational amplifier. A feedback network around the device provides a variable d-c gain through the selection of resistor R13. A 6 db/oct roll off starting at 5.1 kHz is achieved by R16 is parallel with C7. Stability of the post amplifier is assured by careful feedback design and appropriate selection of components C8, C9, R17, and R18.

The drift-error amplifier also uses a Fairchild $\mu$A709 integrated circuit oprational amplifier. A simple feedback network consisting of R34 in parallel with C18 provides

a 6-db/oct roll off starting at $1.06 \times 10^{-3}$ Hz. This low-break frequency allows only the d-c input to be amplified with a gain of 15. Stability of the drift error amplifier is assured by careful feedback design and appropriate selection of components R30, R32, C16, and C17. Thermal stability is achieved by the selection of R31.

The space clamp and buffer consists of components R45, Q5, CR4, C21, Q4, R43, and R44 shown in Figure 25. Q5 and CR4 comprise a series switch which is activated on command from the logic. When the switch is closed (during a 12-millisecond portion of sky time), capacitor C21 charges through R45 and Q5 to the error output of the drift error amplifier. The charging time constant is 9 seconds. Since the thermal time constant of the spacecraft is approximately 120 minutes, 9 seconds is sufficient time to charge capacitor C21 to the resultant error voltage level. When the switch is open, the off resistance of the FET switch is approximately $10^{11}$ ohms. The input resistance of the source follower, Q4, is approximately $10^{9}$ ohms. Therefore, the storage time constant of the circuit is greater than 83 minutes. With this long storage-time constant, there is no perceptable droop of the base line at the output of the IR channel, between clamp times. Resistors R43 and R44 form a voltage divider, the adjustment of which, allows balancing of the IR output d-c level.

The common-mode amplifier uses a Philbrick Q25AH, primarily because of its low-noise figure and high thermal stability. This amplifier is designed to have unity gain for both the error signal input and the bridge signal input and to have a 3-db cutoff frequency at 160 Hz. Stability of the common-mode amplifier is assured by careful feedback design and by capacitor C20.

The active filter uses a Fairchild $\mu$A709 integrated circuit operational amplifier with appropriate feedback around it to provide the desired low-pass filter response. In particular, the filter has a low-pass butterworth characteristic (i.e., maximally flat response). The filter has unity gain at d-c. The 3-db break frequency is 2.5 kHz. The roll-off rate is 12 db/oct. Stability is assured by careful feedback design and selection of components C12, C13, R24, and R25. Thermal stability is achieved

by selection of R23. Minimum weight and small component size are additional advantages of this design.

The control gates permit insertion of the sync pulse and the staircase voltage calibration signal onto the IR output signal. In addition, provision is made to blank the IR signal during sync and calibration time. The blanking gate, Q1, upon command shunts the IR signal from the active filter output to ground through R26. During this time, either Q2 or Q3 turns on, allowing the signal voltages on their respective sources to be impressed across R27 and, therefore, inserted on the output.

The output buffer also uses a Fairchild $\mu$A 709 integrated circuit operational amplifier in its design. Heavy feedback is placed around the device to provide a follower function. The signal input is fed into the noninverting input and the gain at d-c is 1.2. The output of this stage is the composite IR signal output. Amplifier stability is assured by proper selection of components C14, C15, R29, and R28.

(3) Sensitivity Calculations

The signal-to-noise ratio for the infrared channel is simply the signal from the detector for a 330°K scene divided by the amplifier plus detector noise referred to the amplifier input.

The signal from the detector is given by:

$$V_{s\ (330°K)} = \frac{N_{\Delta\lambda} A_o \Omega R \epsilon_o}{\text{bridge factor}} \qquad (13)$$

where

$N_{\Delta\lambda}$ is the radiance in a spectral band 10.5 to 12.5 microns at 330°K scene and equals $2.80 \times 10^{-3}$ watts $cm^{-2}$ $sr^{-1}$,

$A_o$ is the area of the collector and equals 126.8 $cm^2$,

$\Omega$ is the field of view of the radiometer and equals $7.85 \times 10^{-6}$ steradians, and

R is the detector responsivity and equals 1920 $vw^{-1}$.

The total optical transmission efficiency $\epsilon_o$ is 0.46 and is a product of the following suboptical efficiencies:

- Average transmission of the 10.5 to 12.5 micron filter equal to 75 percent.
- Unobscured portion of collecting optics equal to 89 percent.
- Reflectivity of scanning and collecting mirrors combined equal to 89 percent.
- Reflectivity of beam splitter equal to 78 percent.

The bridge factor equals 2 as a result of the shunting of the active flake with a compensating flake of equal resistance.

Thus:

$$V_{S\ (330°K)} = \frac{2.80 \times 10^{-3} \times 126.8 \times 7.85 \times 10^{-6} \times 1920 \times 0.46}{2}$$

$$= 1.27 \text{ millivolts}$$

The general form of the expression for the Johnson noise of the detector is given by:

$$V_n = (4K\ TB\ \Delta f)^{1/2} \qquad (14)$$

Since the bandpass $\Delta f$ of the amplifier is not flat to compensate for the detector time constant, as shown in Figure 24, expression for equation (14) is used.

$$V_n = \left\{4KTR \left[a^2_n (f_n - f_{n-1}) + a^2_{n-1} (f_{n-1} + f_{n-2}) \right.\right.$$

$$\left.\left. + \ldots + a_2^2 (f_2 - f_1) + a_1^2 (f_1 - f_0)\right]\right\}^{1/2} \qquad (15)$$

where

k is Boltzman's constant ($1.374 \times 10^{-23}$ joules per degree Kelvin),

T is the temperature at 300°K, and

R is the Resistance of the detector and compensator in parallel and equals 100 K ohms.

Assuming an electrical response of 50 percent and an optical system modulation transfer of 50 percent results in a total system response of 25 percent. For an electrical response of 50 percent, the peak frequency is 1100 Hz, and the detector noise is 13 microvolts using equation (15). With a detector noise of 13 microvolts, the resultant system noise using a 0.5 db amplifier is 13.8 microvolts. Thus, the signal-to-noise ratio is:

$$S/N = \frac{1.27 \times 10^{-3}}{13.8 \times 10^{-6}} = 92.5 = 39 \text{ db}$$

The actual measured S/N is 38 db and the difference between actual and measured is attributed to 1/f noise of the detector. This signal-to-noise ratio will provide the temperature resolution shown in Figure 27.

c. Visual Channel Signal Electronics

(1) Introduction

The visual channel signal electronics contain a silicon detector, conditioning networks, mode selection, voltage amplifiecation, blank and insert circuits, and an output buffer. A schematic diagram of the visual channel signal electronics is shown in Figure 28.

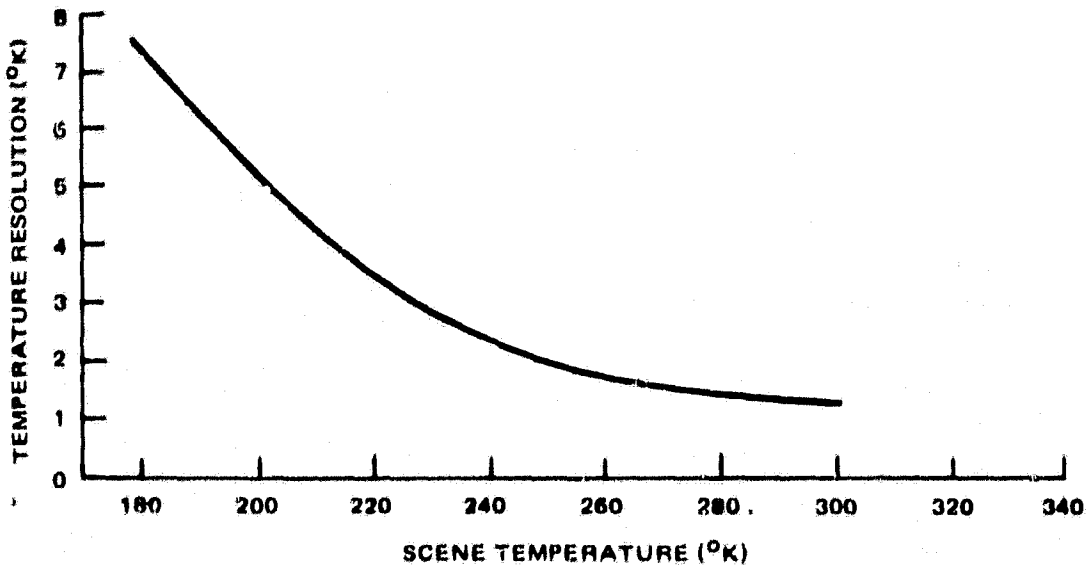
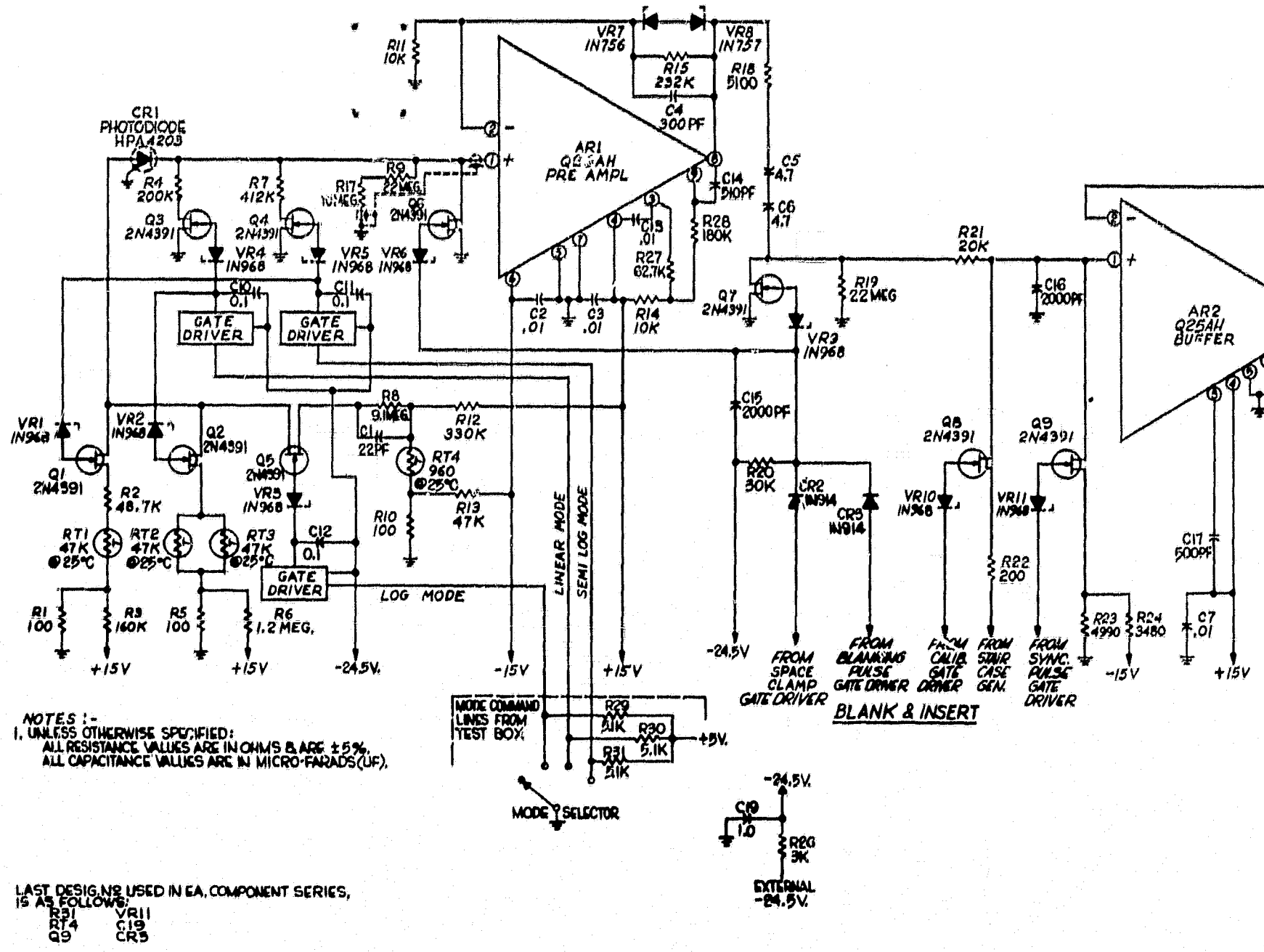



Figure 27. Temperature Resolution vs Scene Temperature

The visual detector is a Hewlett-Packard type HPA4203 ultrafast low-noise silicon planar PIN photovoltaic diode with high detectivity for visible and near infrared (0.4 to 1.0 microns) radiation. Use of the photodiode in a resistively-loaded, unbiased mode permits selection of a broad range of transfer characteristics from pure logarithmic for open circuit voltage amplifier case to pure linear for the short-circuit current amplifier mode. Use of a common voltage amplifier and selectable load resistors permits operation in the log mode using a 42.2 megohm load, semilog mode using 511 kilohms, and linear mode with 224 kilohms. A departure from linearity of a few decibels in the linear mode is a result of maintaining the load resistance high enough to avoid reduction of signal level but too high to satisfy the pure linear mode short circuit current requirement. The light diode resistance loading and amplifier configuration is shown in Figure 29.

(2) Detailed Description

Selection of the log, semilog, or linear, transfer characteristic is accomplished with 2N4391 junction FET switches which connect the proper output



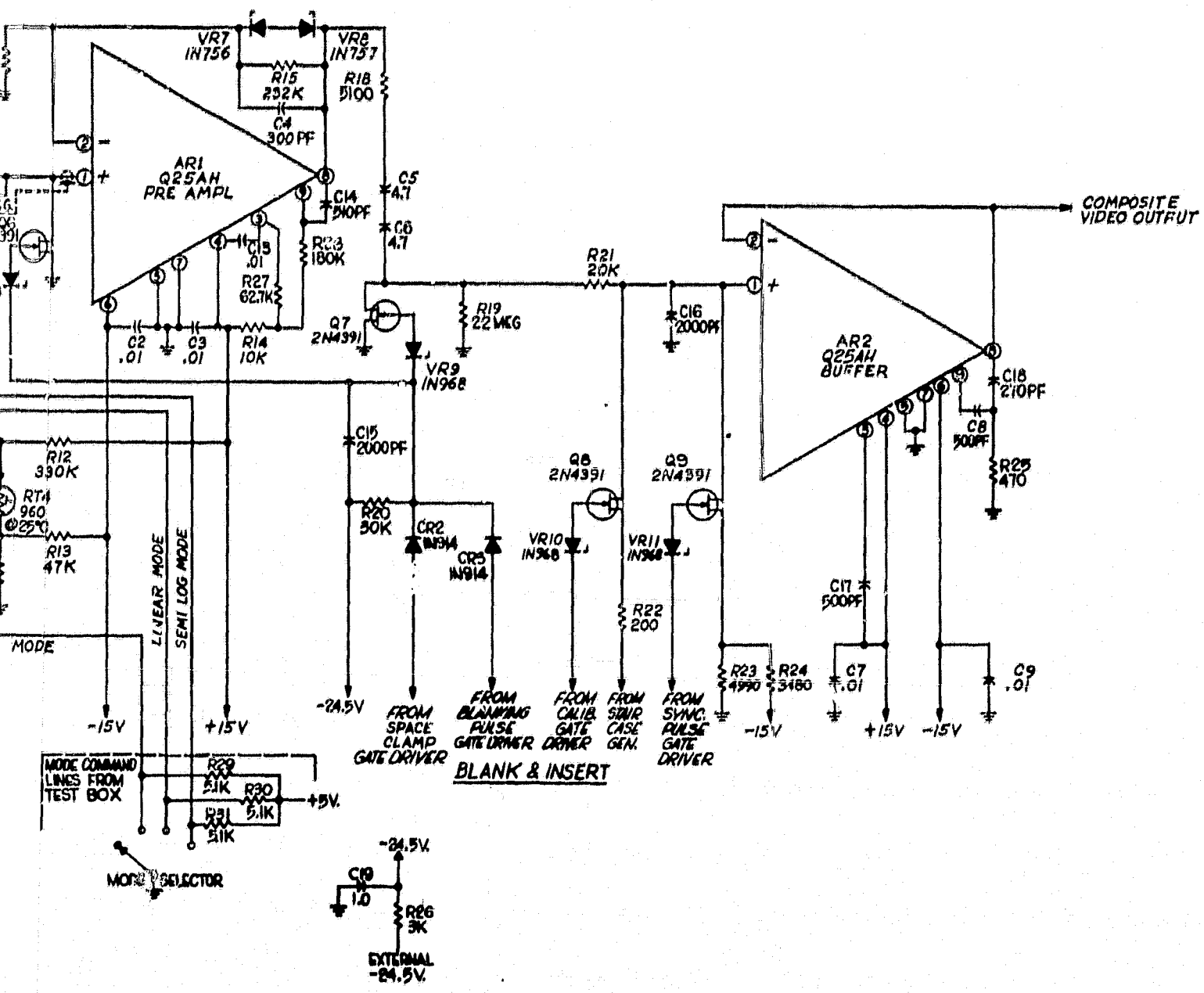

NOTES :-
1. UNLESS OTHERWISE SPECIFIED:
ALL RESISTANCE VALUES ARE IN OHM'S & ARE ±5%.
ALL CAPACITANCE VALUES ARE IN MICRO-FARADS (UF).

LAST DESIG.NS USED IN EA. COMPONENT SERIES, IS AS FOLLOWS:

| | |
|---|---|
| R31 | VR11 |
| RT4 | C19 |
| Q9 | CR3 |

Foldout # 1

Figure 2




Foldout #2

**Figure 23. Visual Channel Signal Electronics, Schematic Wiring Diagram**

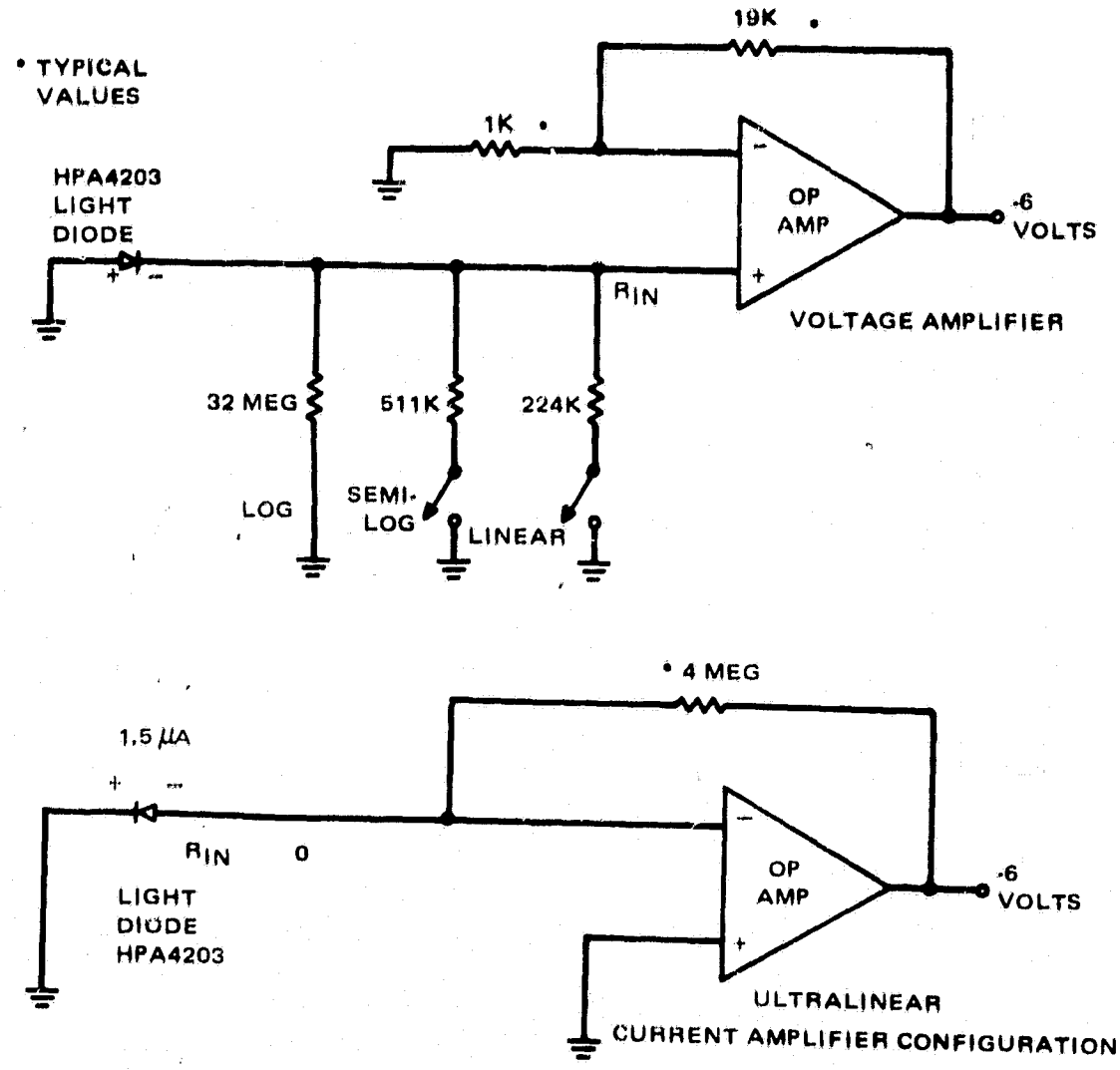


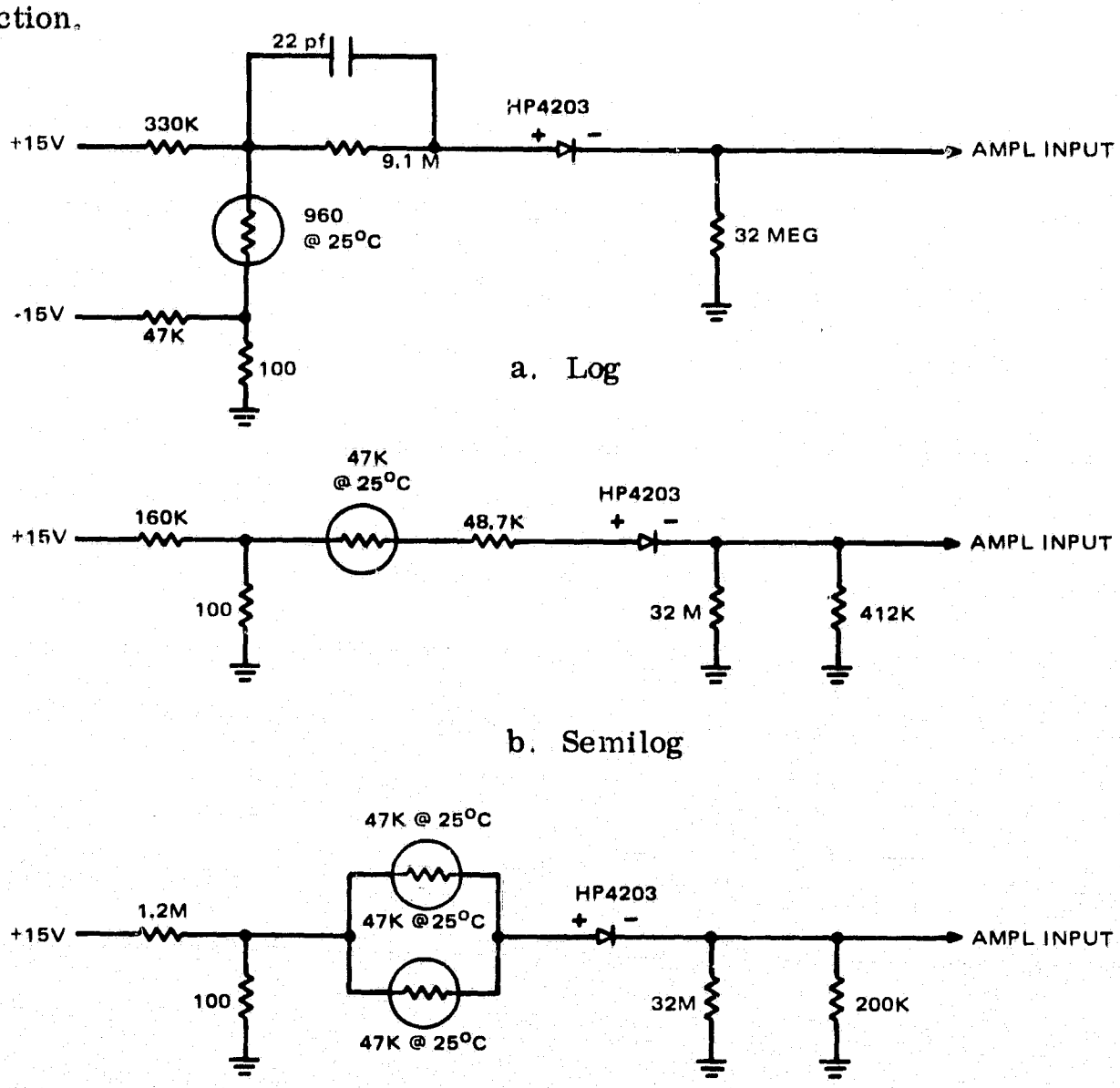

Figure 29. Light Diode Resistance Loading and Amplifier Configuration

load and matching input conditioning network to the light diode. Each mode is initiated through a separate command line activated by standard 0-volt enable and +5-volt disable logic levels. Level changing gate drivers using a 2N722 inverter provide a +5-volt enable and a -24.5-volt disable to switch the FET gates. The IN968 zener diode blocks gate-current flow by preventing a drain-to-gate breakdown when the FET is turned on. The relatively high shunt capacitance of this Zener acts to speed up FET turn on.

The LOG output load of 32 megohms is permanently connected and serves to tie down the amplifier input (in preference to leaving it floating). Upon LOG command, the LOG conditioning network is switched on completing the light diode circuit.

The semilog and linear networks and loads are disconnected. In either of the latter two modes, the 32 megohms shunts the selected output load resistor, changing the net load by approximately 1 percent.

Conditioning networks, shown in Figure 30, in conjunction with output load resistors permit the precise adjustment of: compression characteristics, by total loop resistance loading of the light diode; full-scale output level, by adjusting the resistance divider ratio or amount of resistance in the output compared to the input network resistance; temperature compensation, by using thermally sensitive resistors in the input network; and, zero scale output level adjustment using bias subtraction.




a. Log

b. Semilog

c. Linear

Figure 30. Conditioning Networks, Schematic Diagrams

The Q25AH is used as a very-high-input-impedance direct-coupled noninverting feedback amplifier with drift stabilization provided by an output capacitor and solid state input and output clamps. During space time (when the detector views cold black space), the output FET switch is gated on, charging the output capacitor to a voltage equal to the amplifier output offset. During earth time, the FET switch is gated off, and the voltage across the capacitor cancels the amplifier offset, thus providing an output equal only to the conditioned detector voltage times the gain of the amplifier.

The gate driver and FET gate are the same as those used in the mode-selection circuits. The 5.1-Kilohm resistor connecting pin 8 in series with the 2.3 microfarads drift-stabilization capacitor reduces the maximum inrush current and provides control of the charge time constant. The back-to-back Zeners (IN756 and IN757) provide rapid overload recovery by gain reduction in the presence of input transients exceeding nominal voltage. The feedback network provides a stable gain of 24.2 (or 27.7 db) with a -2 db bandwidth of 1680 Hz. Power supply (±15 volts) filtering is provided with the 0.01 microfarad bypass capacitors. Voltage offset is trimmed out with resistive network between pins 3 and 9 and the +15-volt supply.

The composite video signal is time multiplexed using a short switch for a blanking gate and series switches or transmission gates for inserting the stair and sync pulse.

The output signal from the visual channel video amplifier is the result of the detector field of view scanning the earth, sky, housing, and calibration lamp. At the initiation of blanking, a zero voltage offset low-resistance short circuit appears across the shunt switch. An input 5-Kilohm resistive load terminates the video amplifier while an output 20-Kilohm load terminates the insert circuitry (both through the same shorted shunt switch). When the sync gate is enabled, a -8 volt 30-millisecond pulse will appear on the output bus. After 10 milliseconds, the stair gate is enabled, permittting transmission of the 60-millisecond, six-level, -6 volt stair. After blanking is released, the composite video to the buffer, when commanded, resumes scan of the black housing and the calibration lamp. Note that the blanking time

time serves a dual function by also permitting d-c restoration of the amplifier using the same short switch. The diode OR gate provides the time multiplexed space clamp and blanking pulses to the shunt gate.

A Philbrick Q25AH is used as a very-high input-impedance direct-coupled follower or noninverting-feedback unity-gain amplifier. Input current of a nanoampere and input impedance greater than 10,000 megohms permits use of a high value load resistor (22 megohms) or a very long discharge ramp time constant (greater than 50 seconds) and also allows simple resistive mixing of sync and stair signals. Power inputs (±15 volts) are filtered with 0.01-microfarad bypass capacitors. With the special stabilizing network shown between pins 8 and 9 and between pins 3 and 4 for this 100 percent feedback connection, stability is assured. No voltage network is required because the voltage offset is only a few millivolts.

Transfer characteristics for the LOG, semilog, and linear modes used in the visual channel signal electronics are shown versus temperatures of 5°, 15°, and 25°C in Figures 31, 32, and 33. Also, shown in Figure 34, is the ultralinear short-circuit current mode which is desirable in a system where the analog is converted to digital before storage and transmission.

(3) Visual Channel Sensitivity Calculation

The solar irradiance at the earth's surface varies with Solar Zenith angle due to preferential scattering of the shorter wavelengths, but this can be ignored for relatively small air mass numbers. The spectrum of sunlight incident on the Earth's atmosphere is given in the 1965 Handbook of Geophysics and these data are reproduced in Table 4.

Integrating Table 4 with the combined spectral response curve (Figure 9) of the silicon detector results in a quantity which is essentially $N_\lambda R_\lambda$ (radiance times responsivity). For the wavelength interval 0.5 to 0.75, $N_\lambda R_\lambda$ is $23.6 \times 10^{-4}$ amp/cm$^2$ - ster.

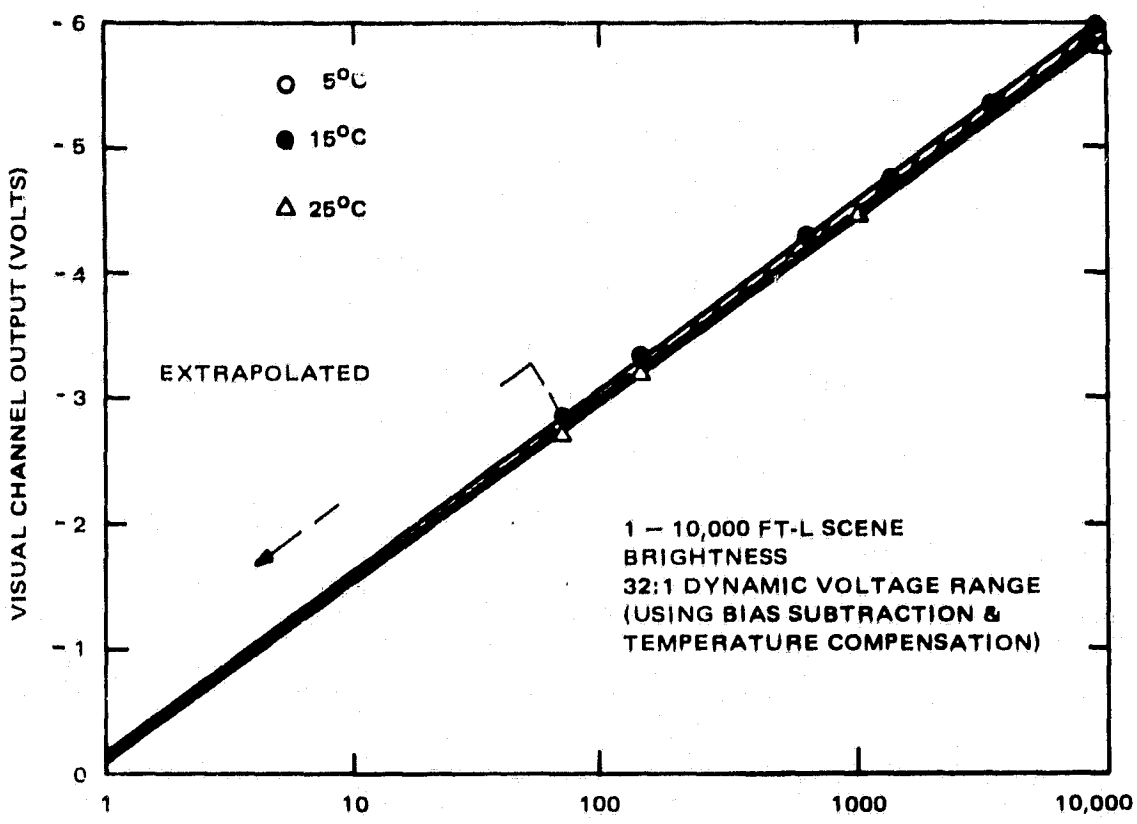



Figure 31. Transfer Characteristics, Log Mode

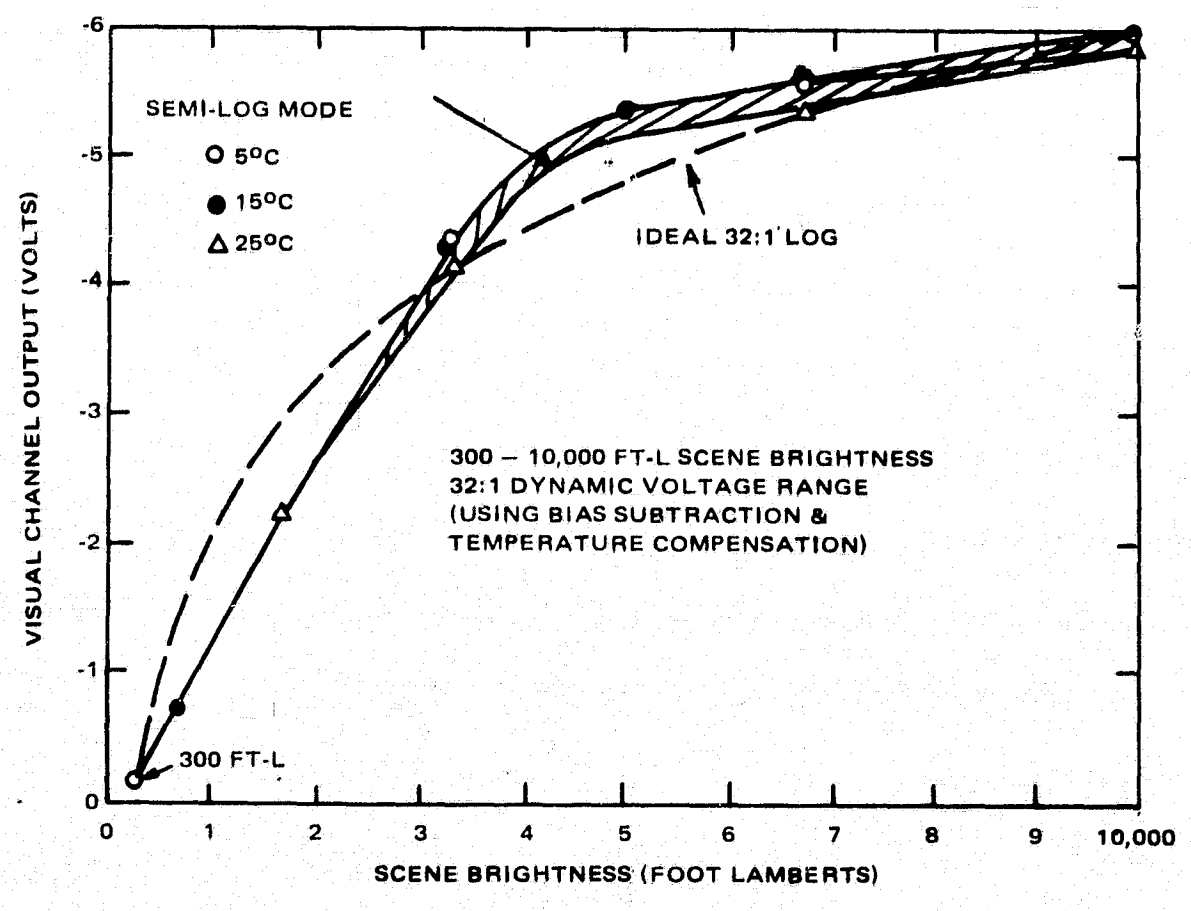



Figure 32. Transfer Characteristics, Semi-Log Mode

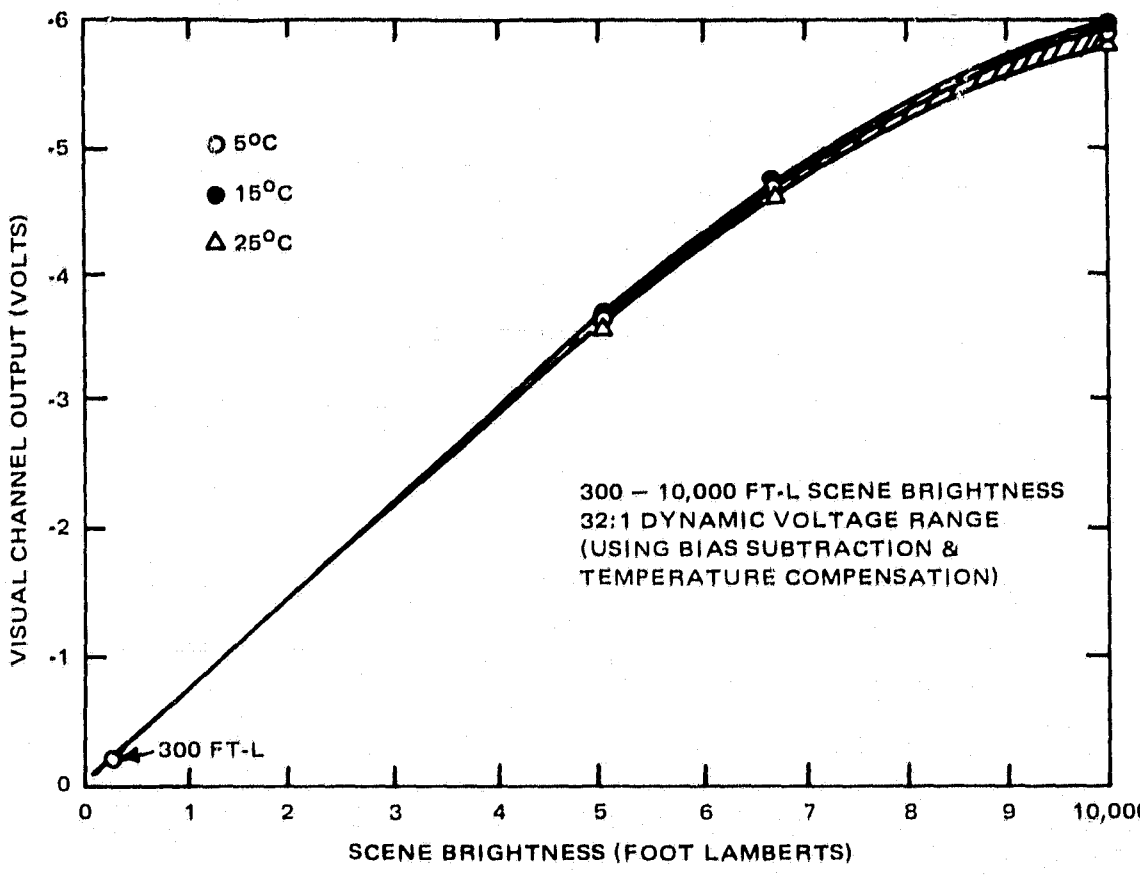



Figure 33. Transfer Characteristics, Linear Mode

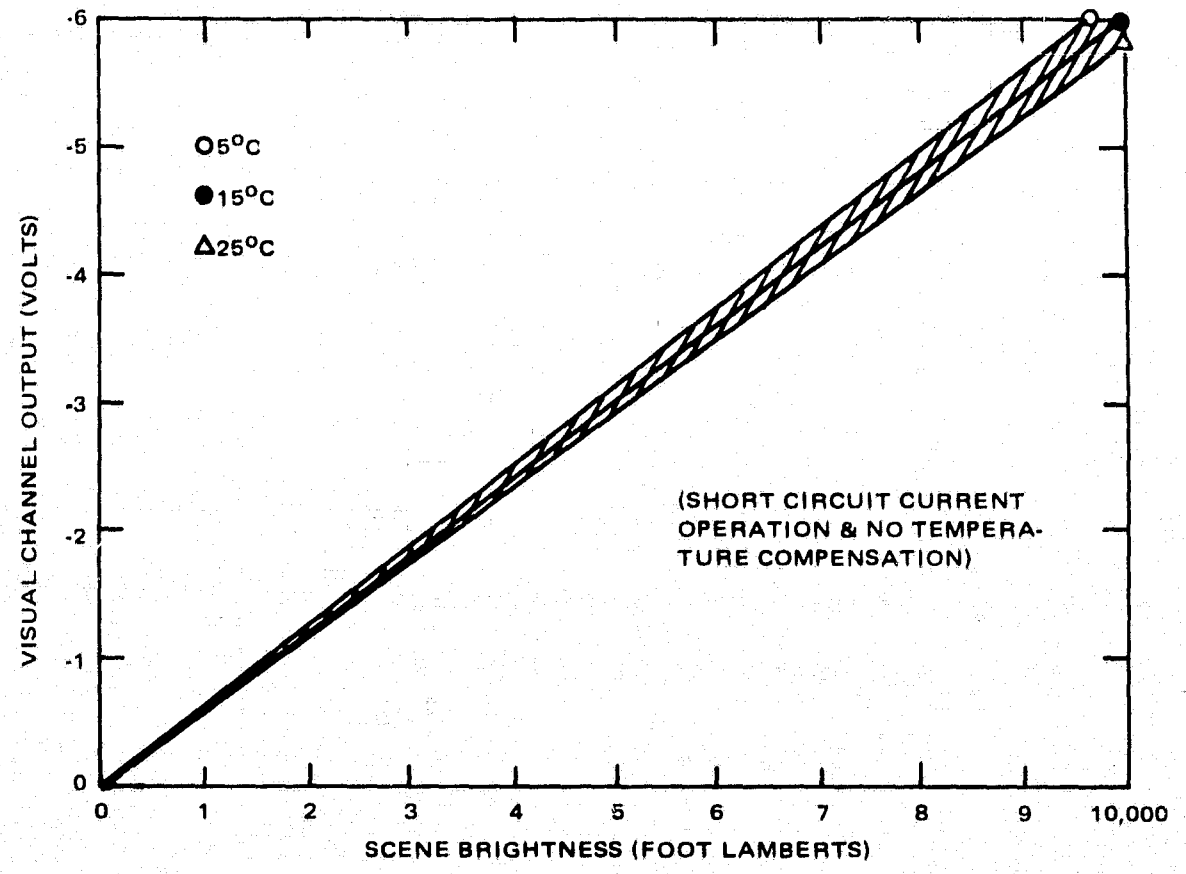



Figure 34. Transfer Characteristics, Ultra-Linear Mode

TABLE 4. SOLAR IRRADIANCE OUTSIDE THE ATMOSPHERE

| Wavelength Region (microns) | Irradiance (watts/$m^2/\mu$) |
|---|---|
| 0.5 - 0.55 | 980 |
| 0.55 - 0.6 | 950 |
| 0.6 - 0.65 | 860 |
| 0.65 - 0.7 | 770 |
| 0.7 - 0.75 | 680 |

The detector short circuit signal current produced is given by

$$i_s = \epsilon_o \, A_o \, \Omega \, N_\lambda R_\lambda$$

where:

$N_\lambda R_\lambda$ = $23.6 \times 10^{-4}$ amp/$cm^2$ - ster

$\epsilon_o$ = optical efficiency = 0.5*

$\Omega$ = Field of View = $4.15 \times 10^{-6}$ steradians

$A_o$ = Area of collector = 126.8 $cm^2$

$i_s$ = $0.5 \times 126.8 \times 4.15 \times 10^{-6} \times 23.6 \times 10^{-4}$

= $0.62 \times 10^{-6}$ amperes.

The Johnson noise developed in the load resistor of the linear mode is

$$V_{noise} = \sqrt{4KTR\Delta f}$$

* $\epsilon_o$ indicates the effects of the reflectivity of the three mirrors and the transmission of the magnifying lens. The effects of the filters and beamsplitter are already included in the $N_\lambda R_\lambda$ value.

$$V_{noise} = 3 \times 10^{6} \text{ volts}$$

for

$$R = 200 \text{ Kilohms}$$

and

$\Delta f$ = 2.62 kHz (effective noise bandwidth for a 1680 Hz bandwidth and a 6 db/octave rolloff)

For a 0.5 db NF amplifier $V_N = 3.2. \times 10^{-6}$ volts

The signal-to-noise ratio

$$S/N = \frac{i_S R}{V_N} = \frac{0.62 \times 10^{-6} \times 0.2 \times 10^{6}}{3.2 \times 10^{-6}}$$

S/N (for linear mode) = $3.9 \times 10^{4}$ at maximum scene illumination for 80 percent albedo.

## 3. Logic

### a. Introduction

The logic section of the dual channel scanning radiometer provides all necessary timing and control signals for the electronics, as well as the following timing and control functions:

- Space clamp (d-c restore),
- Video blanking,
- Sync pulse generation, and
- Staircase voltage calibration generation.

The logic is constructed of monolithic integrated circuits of the low-power diode transistor logics (DTL) type. The staircase generator uses a monolithic MOS FET six-gate array.

The logic is constructed of monolithic integrated circuits of the low-power Diode Transistor Logics (DTL) type. The staircase generator uses a monolithic MOS FET six-gate array.

b. Logic Design

The logic circuitry, shown schematically in Figure 35, requires only two signal inputs for operation, both of which are derived from the magnetic shaft encoder. They are the position-pulse signal and the velocity-pulse signal. The position pulse occurs once per revolution of the mirror. The velocity pulse occurs every degree of mirror rotation. The important logic input timing parameters are summarized in Table 5.

TABLE 5. LOGIC INPUT TIMING

| Parameter | Value |
|---|---|
| Motor Scan Rate (90 rpm) | 540°/sec/90 rpm |
| Motor Encoder Position Pulse Period | 667 ms |
| Motor Encoder Velocity Output Rate | 540 pps |
| Motor Encoder Velocity Output Period | 1.85 ms |

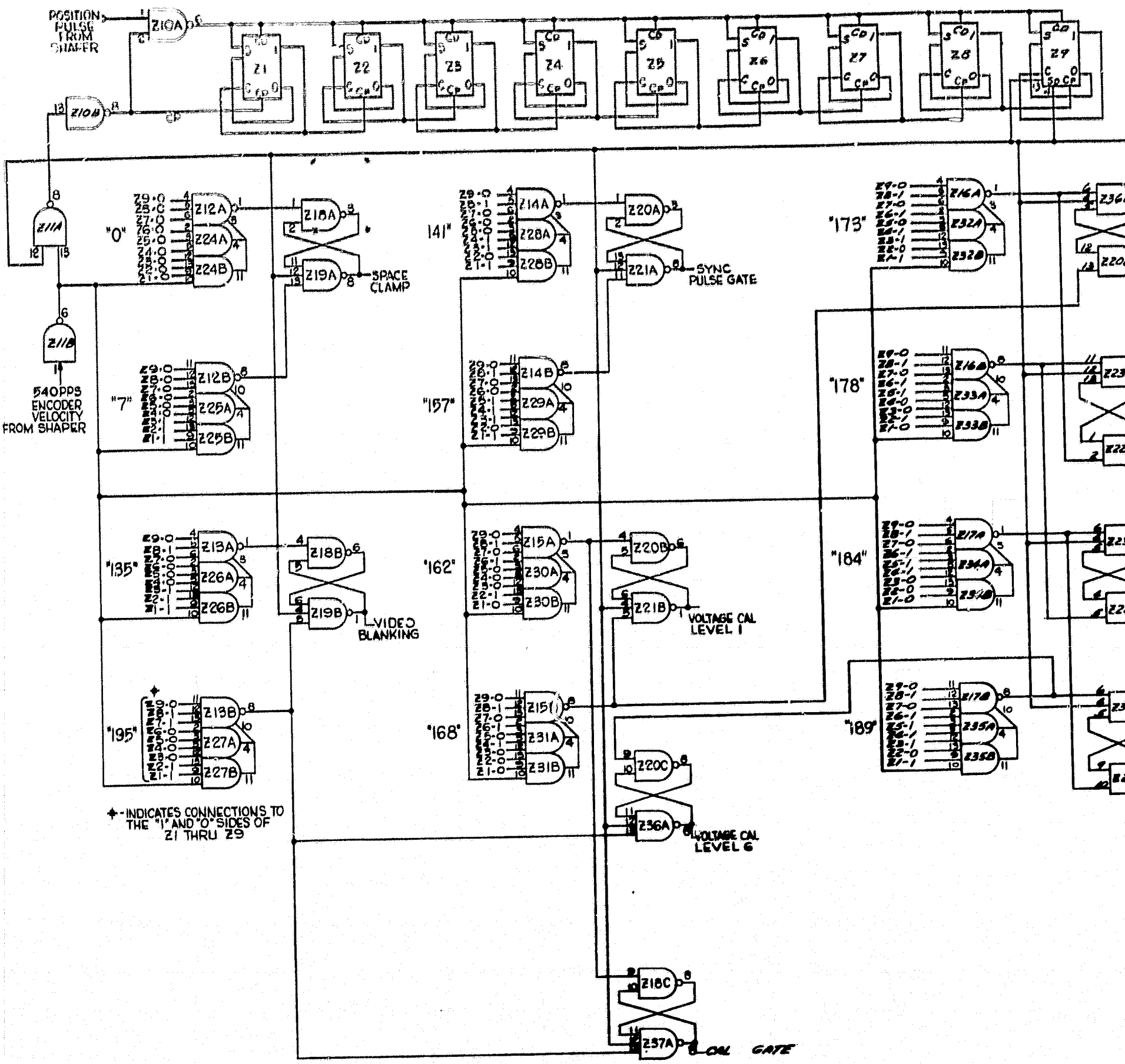
The logic consists of a 9-bit counter, constructed of type LPDT$\mu$L 9040 DTL clocked FLIP-FLOP modules. The remainder of the logic consists of DTL logic gates, described in Table 6, and configured to provide the necessary timing of events. In addition to the logic shown in Figure 35, the staircase generator is also located on the logic board. This generator, shown in Figure 36, is constructed of an MEM2009 P-channel MOS FET six-gate array and associated level-shifting transistor networks. These level shifters are required because the DTL logic which activates this device operates on 0 to + 5-volt logic levels whereas -24 to 0-volt levels are required for the MEM2009.

TABLE 6. TYPES OF LOGIC MODULES

| Module | Type | Description |
|---|---|---|
| Z1, thru Z9 | LPD T$\mu$L 9040 | DTL clocked Flip-Flop |
| Z10, Z11 | DT$\mu$L 930 | Dual 4-input gate |
| Z12 thru Z17 | LPDT$\mu$L 9042 | Dual 3- and 4-input gate |
| Z18, Z20, Z22 | LPDT$\mu$L 9046 | Quad 2-input DTL gate |
| Z19, Z21, Z23 | LPDT$\mu$L 9042 | Dual 3- and 4-input gate |
| Z24 thru Z35 | DT$\mu$L 933 | Dual 4 extender |
| Z36, Z37 | LPT$\mu$L 9042 | Dual 3- and 4-input gate |
| Staircase Generator | MEM2009 | 6 MOS FET array |

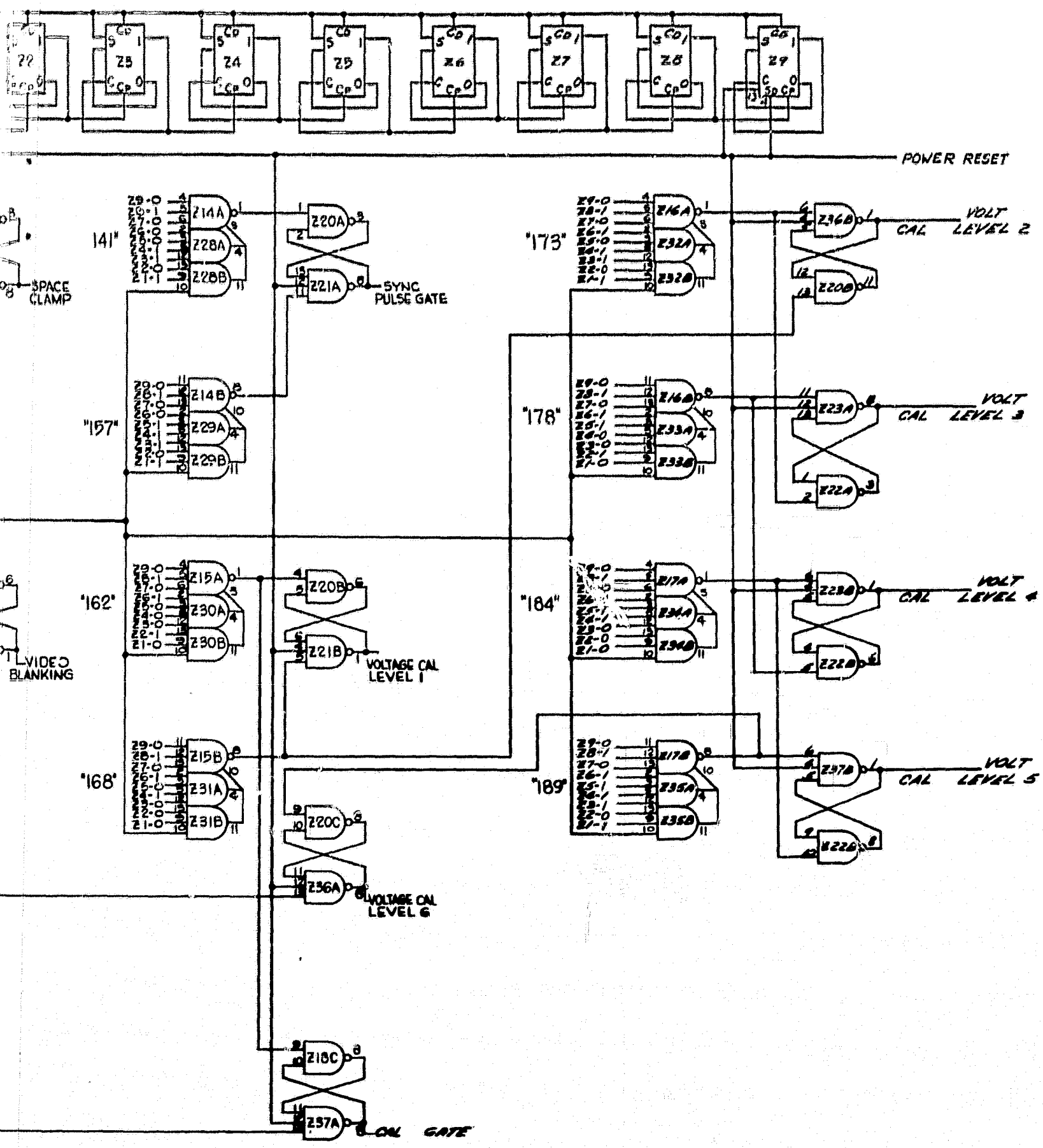
c. Logic Operation

The operation of the logic is presented in terms of the logic outputs and timing of events. These outputs and the corresponding times are summarized in Table 6. The DTL logic "ONE" is 0 volt and the logic "ZERO" is +5 volts.




Foldout #1

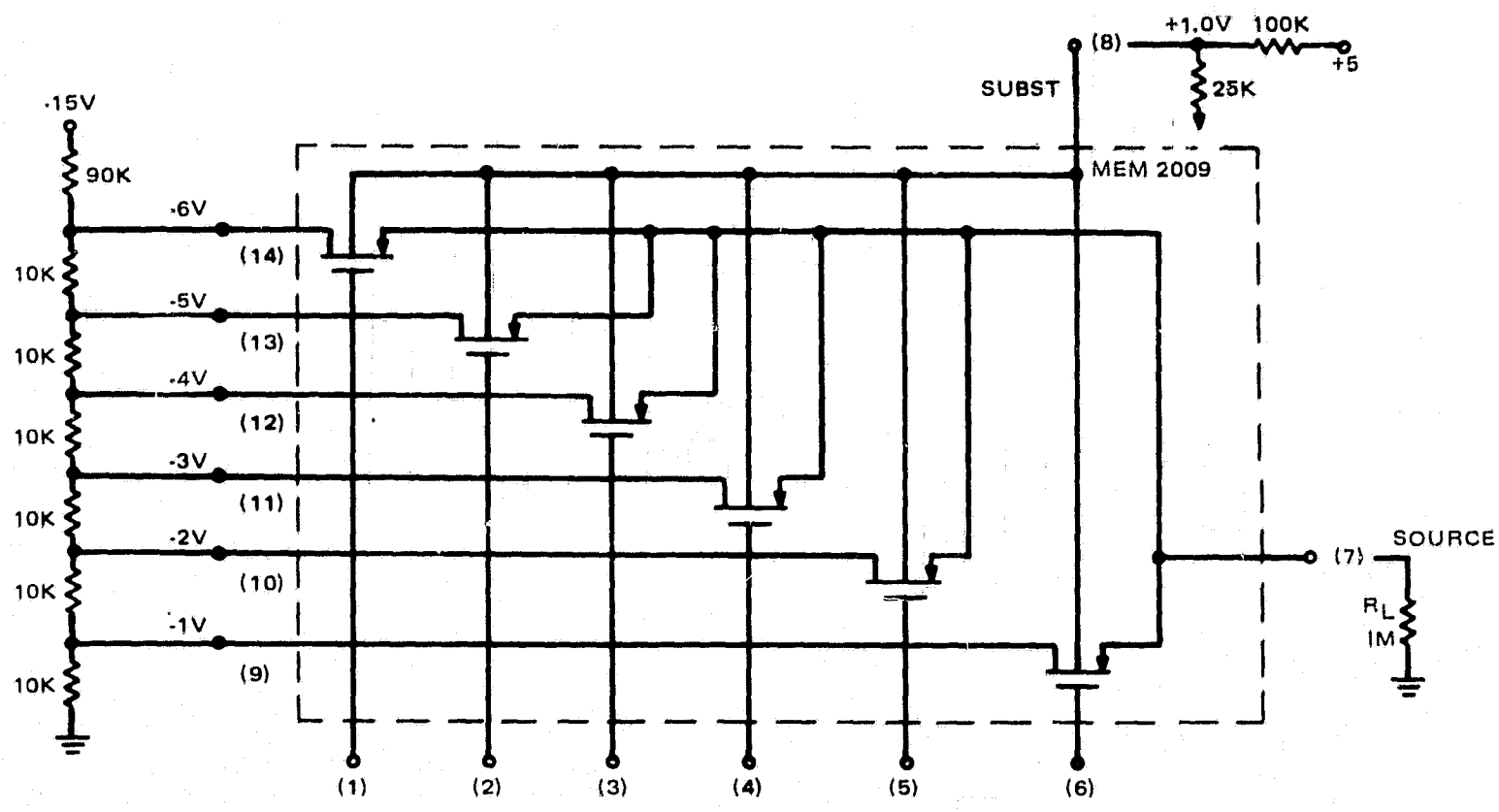
Figure




Foldout #2

Foldout #1

**Figure 35. Dual Channel Radiometer, Logic Diagram**



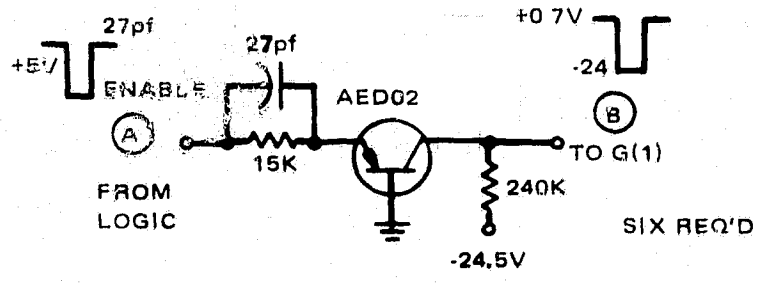




Figure 36. Six-Level Voltage Calibration Generator

A count is defined as the period of one velocity pulse (i.e., 1.85 milliseconds). For example, voltage calibration level 1 starts at count 162, or approximately 300 milliseconds after the start of the space clamp.

A truth table of the logic input to each gate section is shown in Table 8. It should be noted that each logic 9 bit word represents a count listed in Table 7.

The staircase generator circuit is essentially a six-input commutator and consists of an MEM2009, MOS FET array, a precision voltage divider, and a set of six-level shifters. Inputs (drains) 9 through 14 are connected to the voltage divider.

TABLE 7. LOGIC OUTPUTS AND TIMES OF EVENTS

| Outputs | Output Level (volts) | Count Time (× 1.85 milliseconds) |
|---|---|---|
| Enable Amplifier Space Clamp | 0 | 0 |
| Disable Amplifier Space Clamp | +5 | 7 |
| Enable Video Blanking | 0 | 135 |
| Disable Video Blanking | +5 | 195 |
| Enable Sync Pulse Gate | 0 | 141 |
| Disable Sync Pulse Gate | +5 | 157 |
| Enable volt. calib. level 1 | 0 | 162 |
| Disable 1 | +5 | 168 |
| Enable 2 | 0 | 168 |
| Disable 2 | +5 | 173 |
| Enable 3 | 0 | 173 |
| Disable 3 | +5 | 178 |
| Enable 4 | 0 | 178 |
| Disable 4 | +5 | 184 |
| Enable 5 | 0 | 184 |
| Disable 5 | +5 | 189 |
| Enable 6 | 0 | 189 |
| Disable 6 | +5 | 195 |
| Enable voltage calibration gate | 0 | 162 |
| Disable voltage calibration gate | +5 | 195 |

TABLE 8. LOGIC TRUTH TABLE

| Input Signal | Logic Condition | | | | | | | | |
|---|---|---|---|---|---|---|---|---|---|
| | Z9 | Z8 | Z7 | Z6 | Z5 | Z4 | Z3 | Z2 | Z1 |
| Enable Amp. D-C Restore | 0 | 0 | 0 | 0 | 0 | 0 | 0 | 0 | 0 |
| Disable Amp. D-C Restore | 0 | 0 | 0 | 0 | 0 | 0 | 1 | 1 | 1 |
| Enable Video Blanking | 0 | 1 | 0 | 0 | 0 | 0 | 1 | 1 | 1 |
| Disable Video Blanking | 0 | 1 | 1 | 0 | 0 | 0 | 0 | 1 | 1 |
| Enable Sync Pulse Gate | 0 | 1 | 0 | 0 | 0 | 1 | 1 | 0 | 1 |
| Disable Sync Pulse Gate | 0 | 1 | 0 | 0 | 1 | 1 | 1 | 0 | 1 |
| Enable volt. calib. level 1 | 0 | 1 | 0 | 1 | 0 | 0 | 0 | 1 | 0 |
| Disable volt. calib. level 1 | 0 | 1 | 0 | 1 | 0 | 1 | 0 | 0 | 0 |
| Enable 2 | 0 | 1 | 0 | 1 | 0 | 1 | 0 | 0 | 0 |
| Disable 2 | 0 | 1 | 0 | 1 | 0 | 1 | 1 | 0 | 1 |
| Enable 3 | 0 | 1 | 0 | 1 | 0 | 1 | 1 | 0 | 1 |
| Disable 3 | 0 | 1 | 0 | 1 | 1 | 0 | 0 | 1 | 0 |
| Enable 4 | 0 | 1 | 0 | 1 | 1 | 1 | 0 | 0 | 0 |
| Disable 4 | 0 | 1 | 0 | 1 | 1 | 1 | 0 | 0 | 0 |
| Enable 5 | 0 | 1 | 0 | 1 | 1 | 1 | 0 | 0 | 0 |
| Disable 5 | 0 | 1 | 0 | 1 | 1 | 1 | 1 | 0 | 1 |
| Enable 6 | 0 | 1 | 0 | 1 | 1 | 1 | 1 | 0 | 1 |
| Disable 6 | 0 | 1 | 1 | 0 | 0 | 0 | 0 | 1 | 1 |
| Enable voltage calibration gate | 0 | 1 | 0 | 1 | 0 | 0 | 0 | 1 | 0 |
| Disable voltage calibration gate | 0 | 1 | 1 | 0 | 0 | 0 | 0 | 1 | 1 |

The voltage divider provides six 1-volt levels, 0 through -6 volts. The control signals are applied to inputs (gates) 1 through 6 in time sequence, such that each MOS FET turns ON in succession. The MOS FETs are normally OFF and turning them on sequentially permits each voltage divider level output to be impressed across the output (7), $R_L$. Thus, a staircase waveform, starting at 0 and climbing to -6 volts, is generated.

4. Scanning Mirror-Velocity Control Loop

a. Basic Requirements

The two primary considerations in the design of the radiometer mirror-velocity control loop are:

- Short-Term Jitter - The instantaneous velocity must be held sufficiently constant within any one revolution to maintain the angular position of the mirror within 2 milliradians of the position it would have been in had the velocity been truly constant.
- Long-Term Velocity Requirements - The velocity must be locked onto a reference frequency.

b. Design for Short-Term Jitter Requirements

The mirror is driven by a d-c brush torque motor. Since the design philosophy is to keep the weight and, hence, the inertia low, it is necessary to have a tight-velocity control loop around the motor to meet the short-term jitter requirements.

Based on measurements of once-around frictional variations of the drive motor, it was determined that the velocity loop would require an open-loop d-c gain of greater than 50 db to meet the requirements. To achieve a suitably damped closed loop with an open-loop bandwidth low enough to ignore ill-defined lags due to motor inductance or inherent amplifier capacitive effects, it becomes necessary to employ a compensation circuit. The frequency compensation network chosen is a lag-lead followed by a lead-lag.

The velocity feedback is derived from a 540-pulse-per-revolution encoder, rotating on the same shaft as the motor and mirror. The encoder pulses are converted to dc in a frequency-to-d-c converter. The output of the converter includes a certain amount of 540-cycle-per-revolution ripple, which, because of the high-loop gain, would be sufficient to saturate the power amplifier. However, since the velocity of the motor is nominally constant and, therefore, the ripple is at a constant frequency, the ripple is eliminated using a sharp notch filter. Since the frequency of the notch is considerably above the loop crossover frequency, the loop stability is not affected. The solid (unbroken) lines in the block diagram of Figure 37 show the velocity control loop.

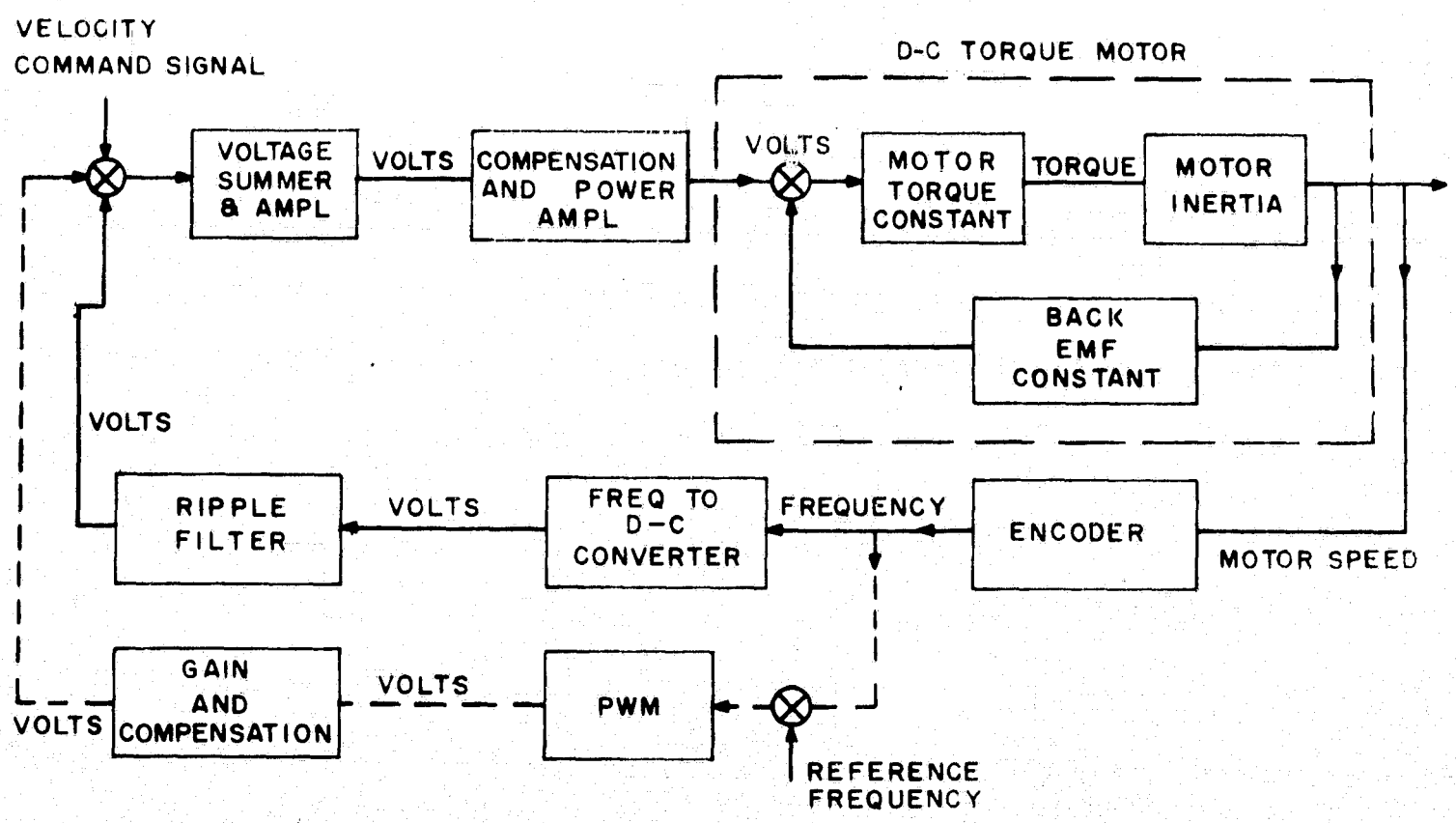



Figure 37. Radiometer Mirror-Velocity Control Loop, Block Diagram

c. Design for Long-Term Velocity Requirements

To maintain the velocity locked to a reference frequency, the portion of the block diagram shown by interrupted (broked) lines in Figure 37 is used. Further details of the pulse-width modulator (PWM logic circuitry are shown in Figure 38. Basically, the operation of the loop is as follows. The phase of the encoder velocity output signal is compared with that of the spacecraft clock reference signal in the PWM. The PWM produces a series of bipolar constant-amplitude, rectangular output pulses of frequency equal to the 540 pps reference frequency. The pulse polarity is determined by the polarity of the phase difference while the varying width is instantaneously representative of the magnitude of the phase difference of the phase difference of the two frequencies. This signal is then smoothed and fed through a gain and compensation amplifier before summing into the velocity-loop input. The velocity command signal of the velocity loop is still required to maintain the nominal velocity of the mirror approximately at that value demanded by the PWM loop. This will keep the PWM signal at a low value.

The operation of the bipolar pulse width modulator shown in Figure 38 is as follows. At time t = 0, the 540 pps reference frequency clock input pulse rises from 0 to +5 volts. The output of the associated input inverter simultaneously falls from +5 to 0 volts. This logical "ONE" level sets the No. 1 R-S flip-flop causing the R-S flip-flop No. 1 output to go to 0 volts. The output of the associated output inverter rises to +5 volts while the output of the sense amplifier goes to +10 volts because of the noninverting gain of 2 for signals entering the plus input via the resistive attenuator (3500 and 6800 $\Omega$).

At time t = $\tau$ the encoder velocity input goes to +5 volts, the associated inverter output goes to 0 volt, setting the No. 2 R-S flip-flop. Simultaneously the NAND gate output goes to 0 volt setting the monostable multivibrator generating a disable gate of 1 milliseconds duration that immediately resets both flip-flops. The flip-flop No. 2 does not get set and the output remains at +5 volts in response to simultaneous set

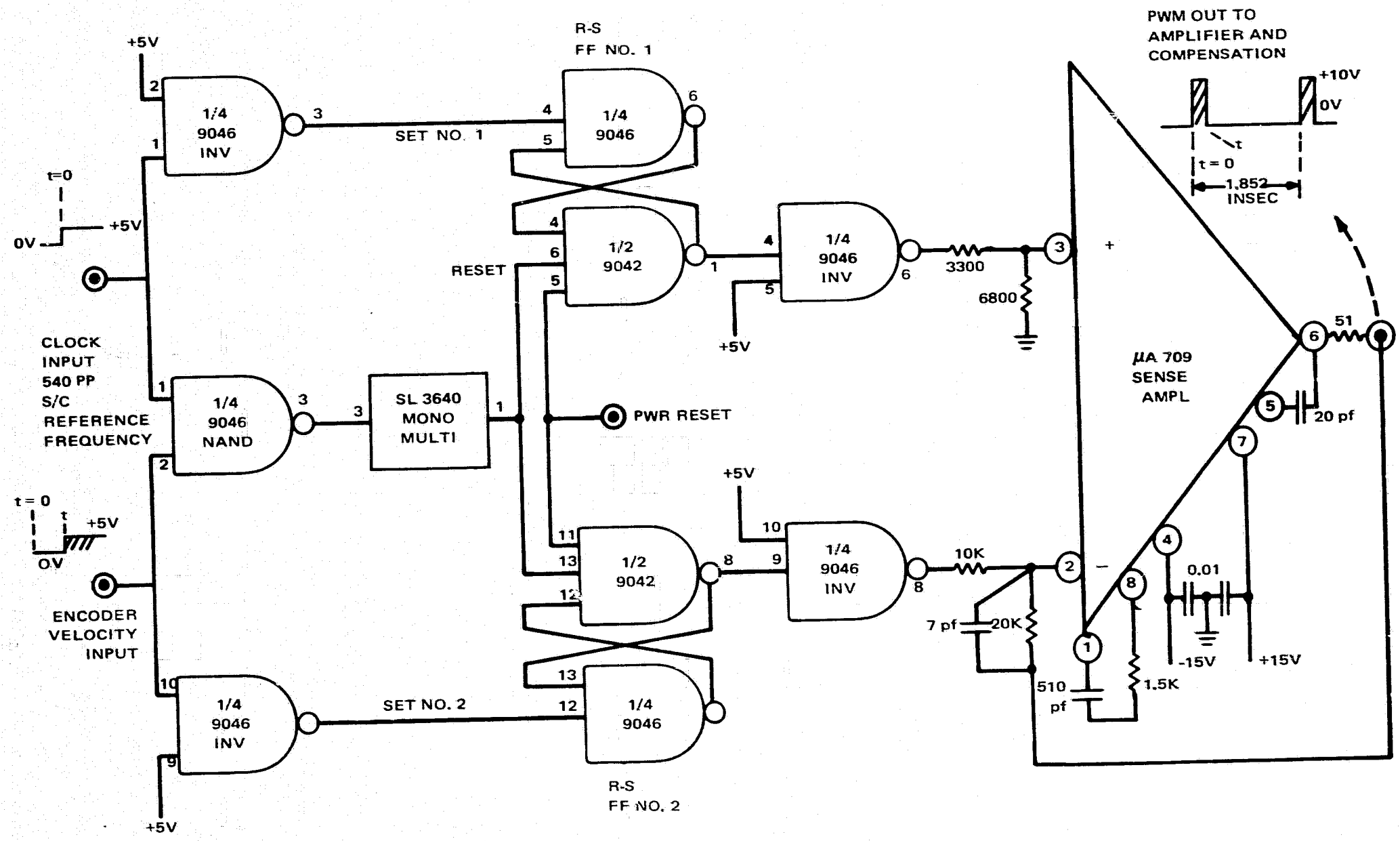



Figure 38. Bipolar PWM $\phi$-Detector for Phase-Locked Mirror Speed Control Position Loop

and reset commands. The sense amplifier output falls back to zero and remains there until another positive transition occurs at the input inverters. Alternate invereted PWM output pulses which would occur at the time of negative transitions at the input inverters are disabled by the reset pulse which straddles this time event as shown in Figure 39.

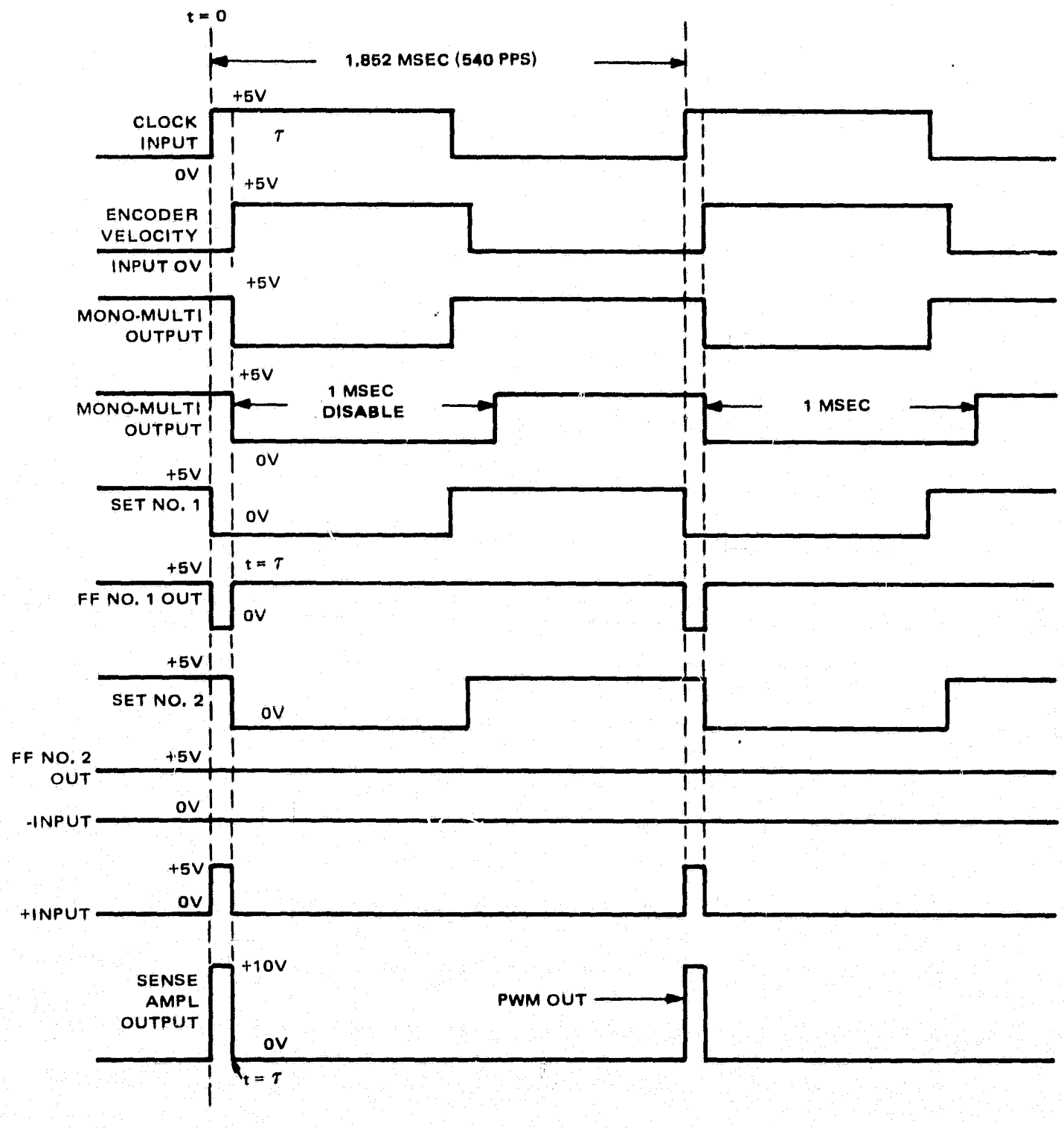



Figure 39. PWM Timing Diagram

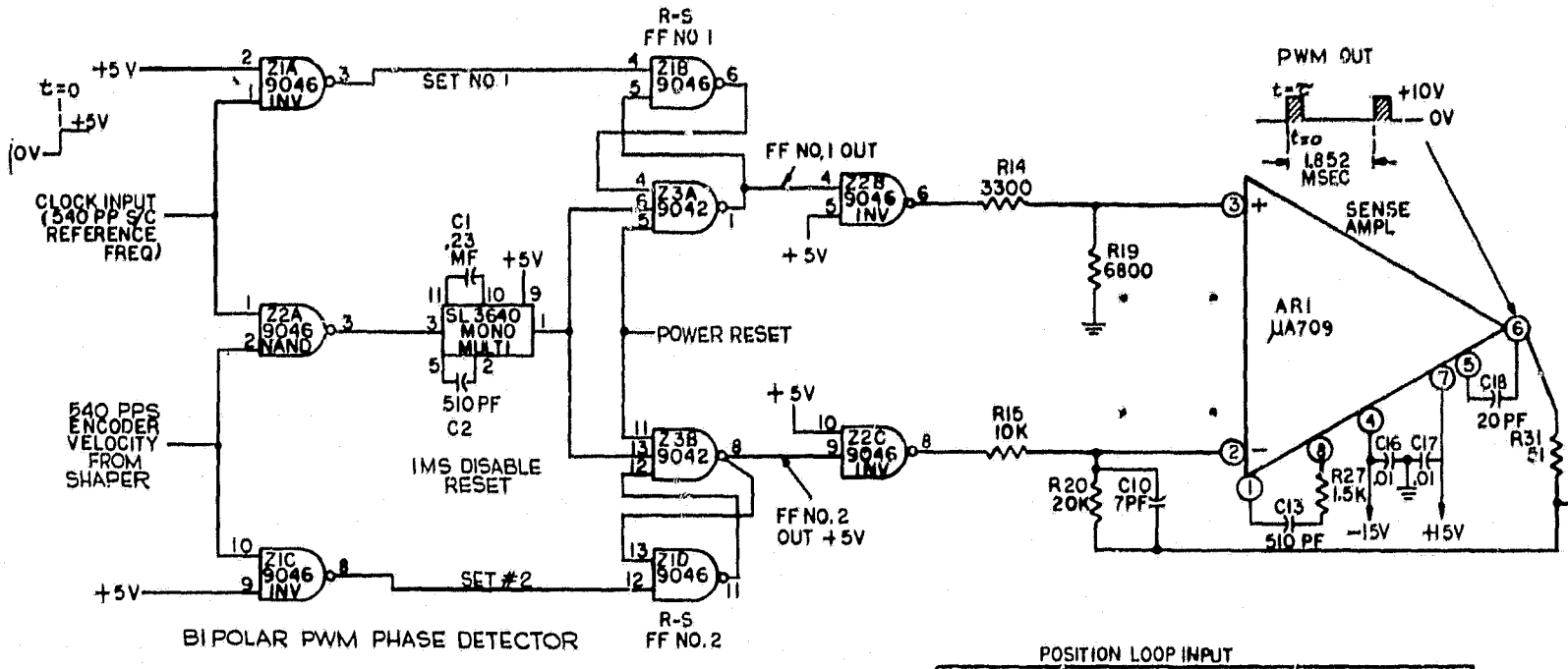
The average value of the sense amplifier PWM output pulse train is directly proportional to the duty cycle as shown in Figure 40.

Ideally, the PWM transfer function is $A_{avg}/\phi_\epsilon = 1.59$ volts/radian. The frequency response is limited by the low pass filter described in the following paragraphs.



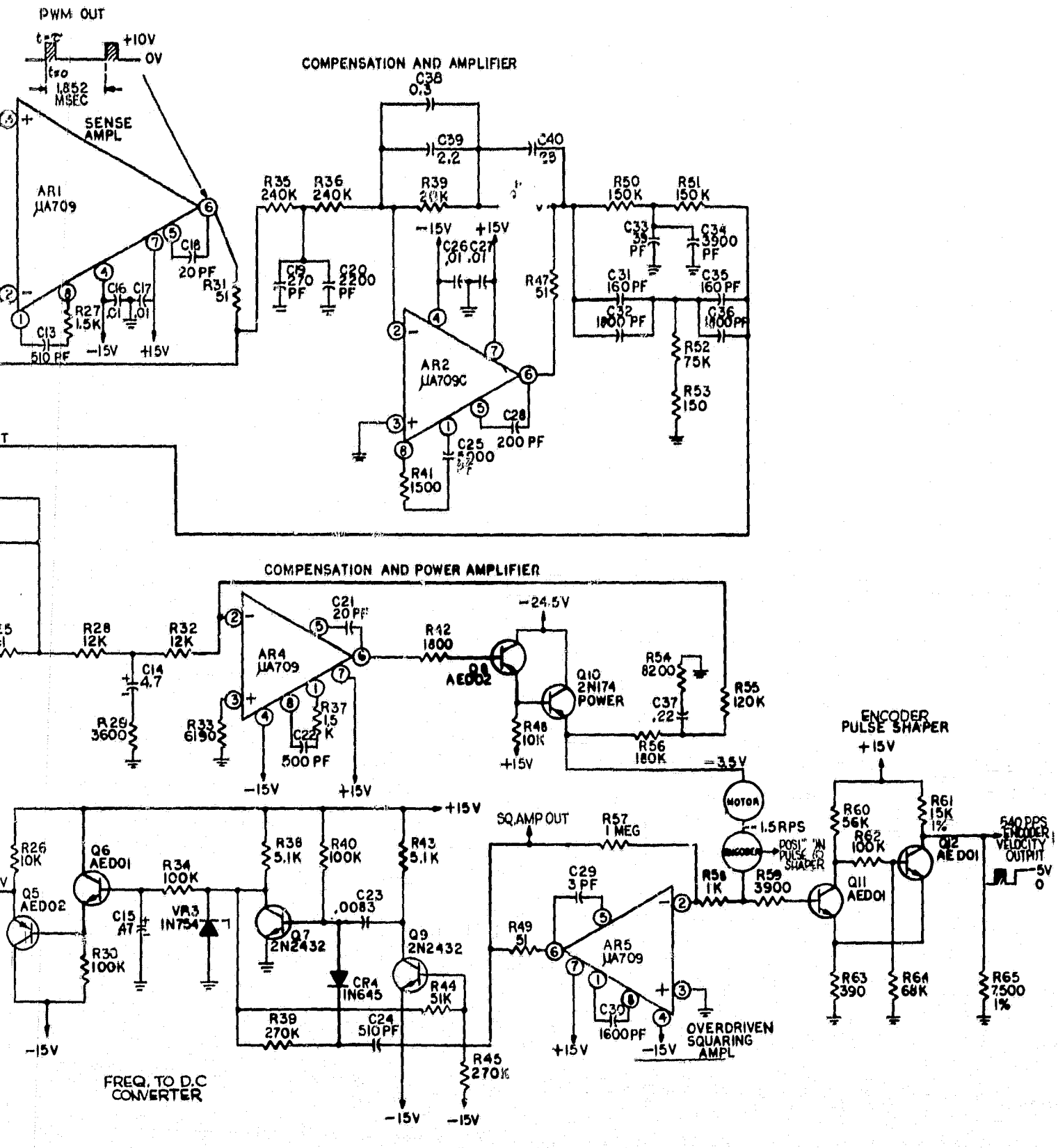

Figure 40. Sensor Amplifier Duty Cycle

The amplifier and compensation networks shown in Figure 41 provide the proper low pass and notch filtering of the PWM error signal. Adequate gain and phase compensation is also provided prior to insertion of the phase error signal into the current summing point of the main tachometer loop to assure a stable and tight phase-lock mirror-speed control system. A Fairchild $\mu$A709 integrated circuit operational amplifier is used in the inverting mode with a near unity gain at d-c,




UNLESS OTHERWISE SPECIFIED:
ALL RESISTANCE VALUES ARE IN OHMS AND ARE ±5%.
ALL CAPACITANCE VALUES ARE IN MICRO-FARADS (UF).

Foldout #1




Foldout #2

**Figure 41. Motor Drive Electronics, Schematic Wiring Diagram**

thus not requiring d-c offset or drift correction. Power inputs (±15 volts) are filtered with 0.01 microfarad bypass capacitors. An open-loop rolloff with a slope of -1 (-6 db/octave) is provided with the Miller capacitor (200 picofarads) between terminals 5 and 6, and the RC lag compensation (5000 picofarads and 1.5 Ω) between pins 1 and 8. Nyquist stability is therefore assured for this near 100 percent d-c feedback connection. The output 51-ohm resistor provides capacitive drive capability. The position notch and compensation network characteristics are shown in Figures 42 and 43.

The motor drive electronics which comprise the motor drive forward loop and the tachometer feedback loop are shown in Figure 41. The velocity command signal is provided by a precision, temperature-drift-compensated series voltage regulator reference source. The notch amplifier serves as the summing amplifier for the

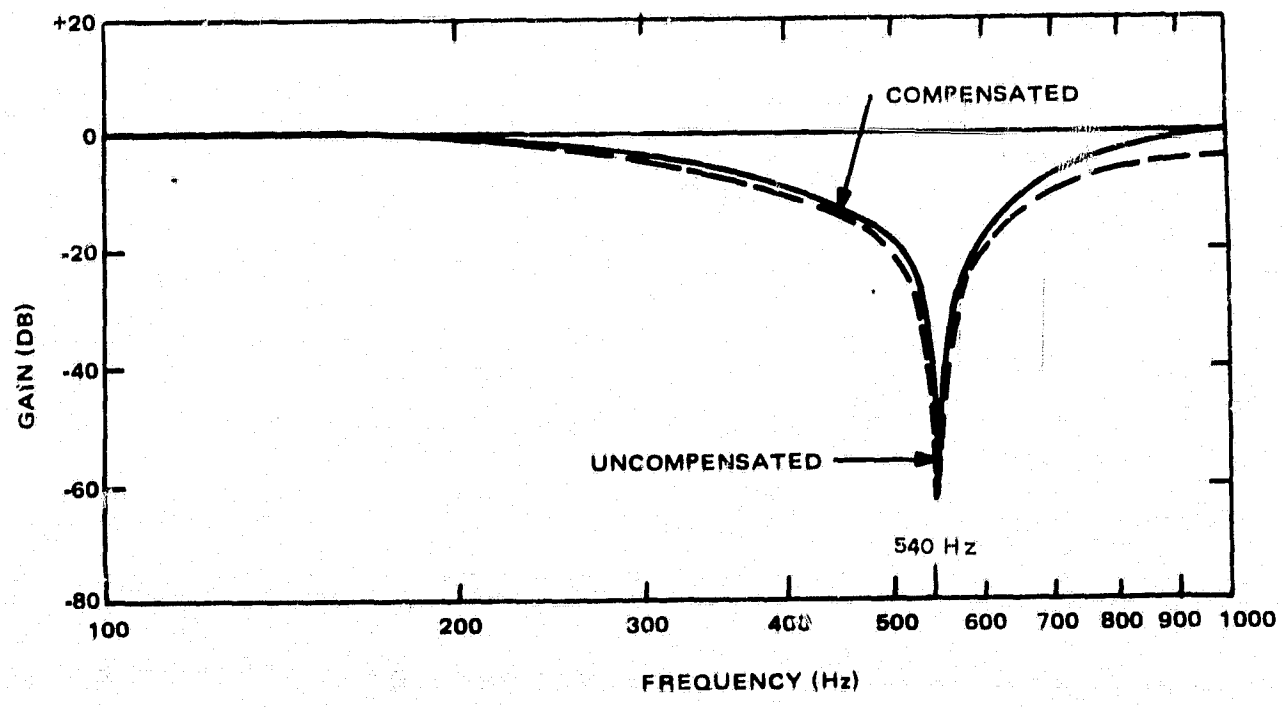



Figure 42. Position Notch Filter and Notch Pulldown

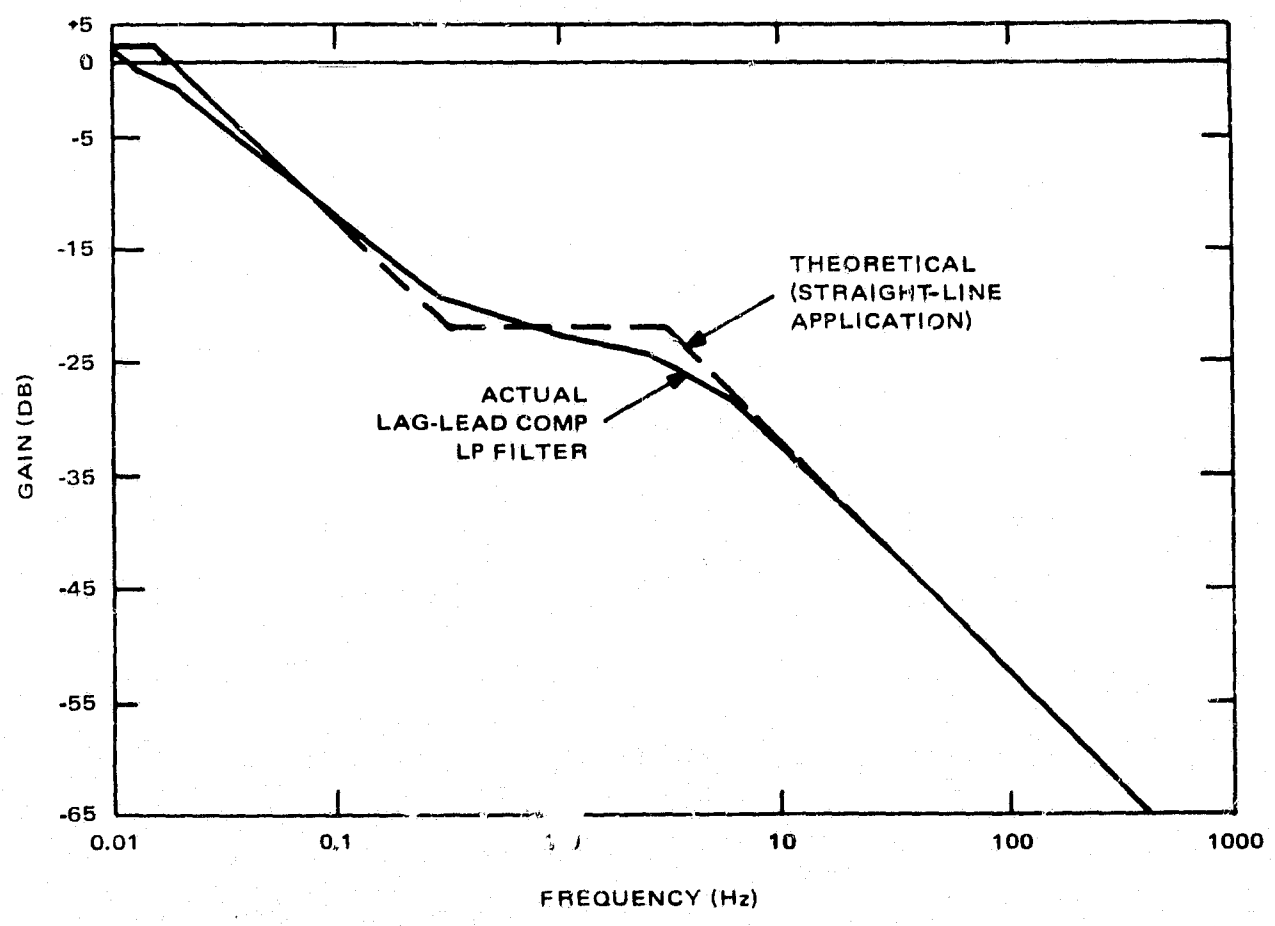



Figure 43. Compensation Network

reference speed input, the tachometer feedback and the position loop feedback. The notch amplifier feedback network provides a double lag-lead velocity notch pulldown. The amplitude-limited PWM output of the 1N754 Zener diode is shown in Figure 44.

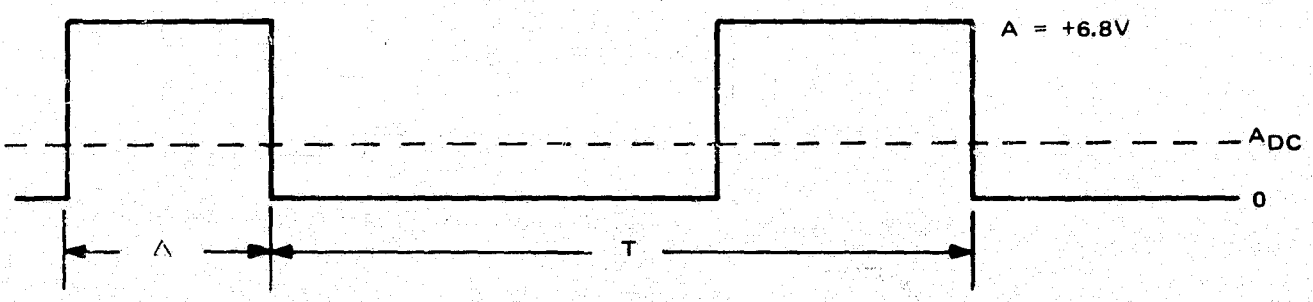



Figure 44. Zener Diode Amplitude-Limited PWM Output

The Bode plot for the uncompensated velocity loop is shown as a dashed line in Figure 45. The phase margin at the crossover frequency of 190 radians/second is essentially zero due to the slope of 2 dropoff. However, 45 db of feedback is available at the once-around motor-shaft frequency and serves to attenuate speed flutter due to this major source of torque disturbance. Values of 50-Hz motor commutator ripple torque effects are minor even without the benefits of feedback which are essentially nil at this frequency. The addition of lag-lead/lead-lag (or notch) compensation results in a safe 37-degree phase margin at the 215 radian/second crossover frequency by sliding through 0 db at a -1 slope.

The Bode plots for the uncompensated and compensated phase-lock loop are shown in Figure 46. For the gains shown of 0.04533 for the closed tach loop (or the velocity regulator) a times-five position loop amplifier gain and a 360-times multiplication of phase error via the 360 magnetic pole encoder, the phase margin is -23 degrees which is

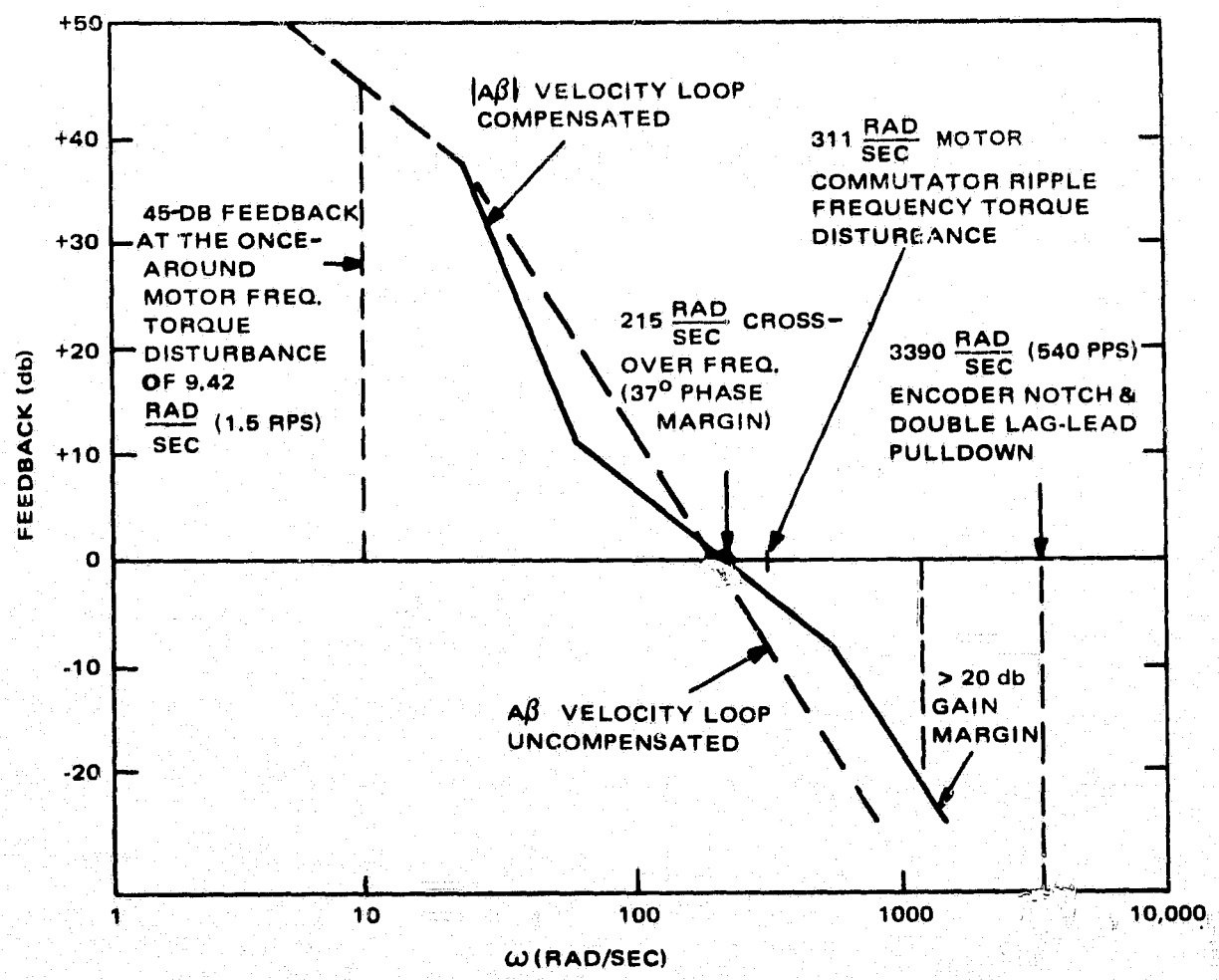



Figure 45. Velocity Loop Characteristics

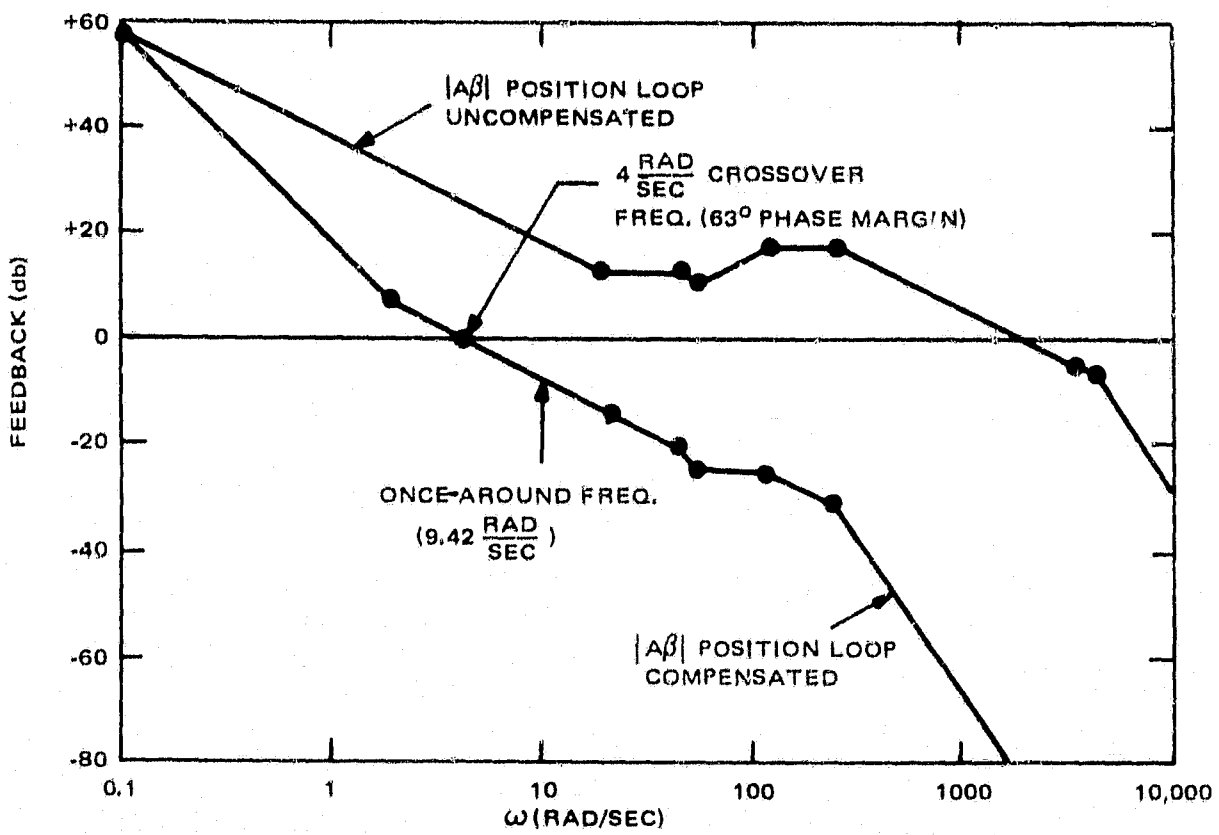



Figure 46. Phase-Lock Loop Characteristics

unstable in the uncompensated configuration. With lag-lead compensation the crossover slope becomes -1 and the crossover frequency 4 radians/second with a 63 degree phase margin. This bandpass provides for long term drift correction of about two revolutions or more.

5. Power Supply

The power supply consists of a DC/DC converter, five full-wave bridge rectifiers, and five voltage regulators to produce the voltages shown in Figure 67.

The DC/DC converter portion of the power supply as shown in Figure 48, uses power transistors, Q1 and Q2, and transformer T. Q1 and Q2 are normally biased ON. In this condition, diodes D4 and D5, D6 allow current to flow in primary windings 1-2

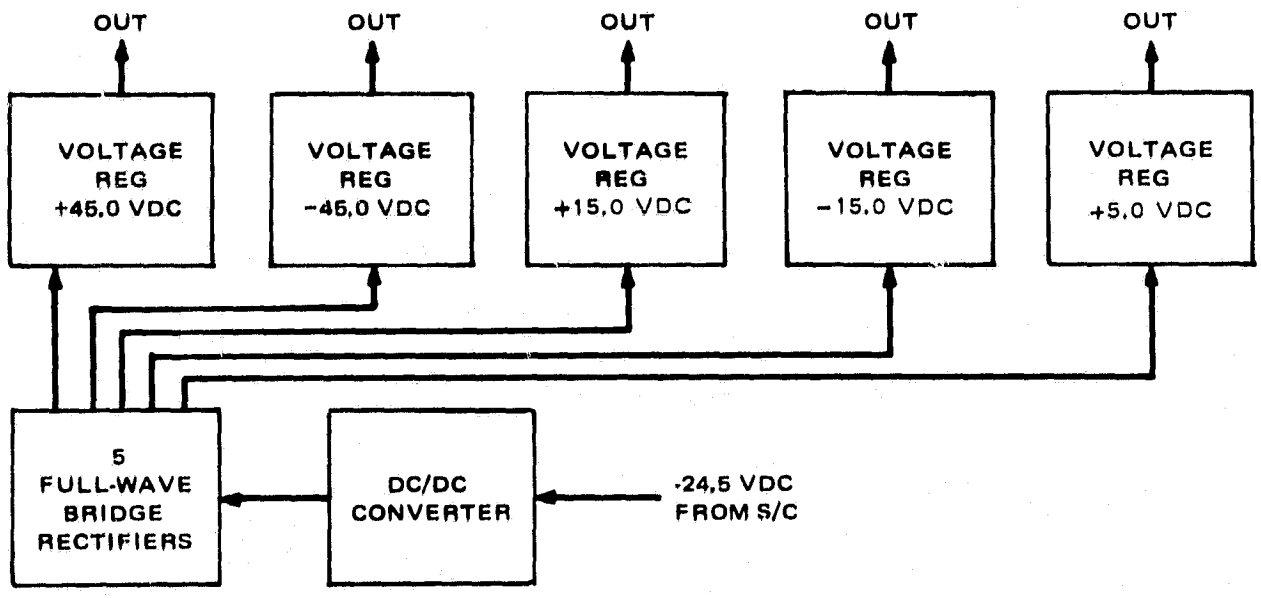
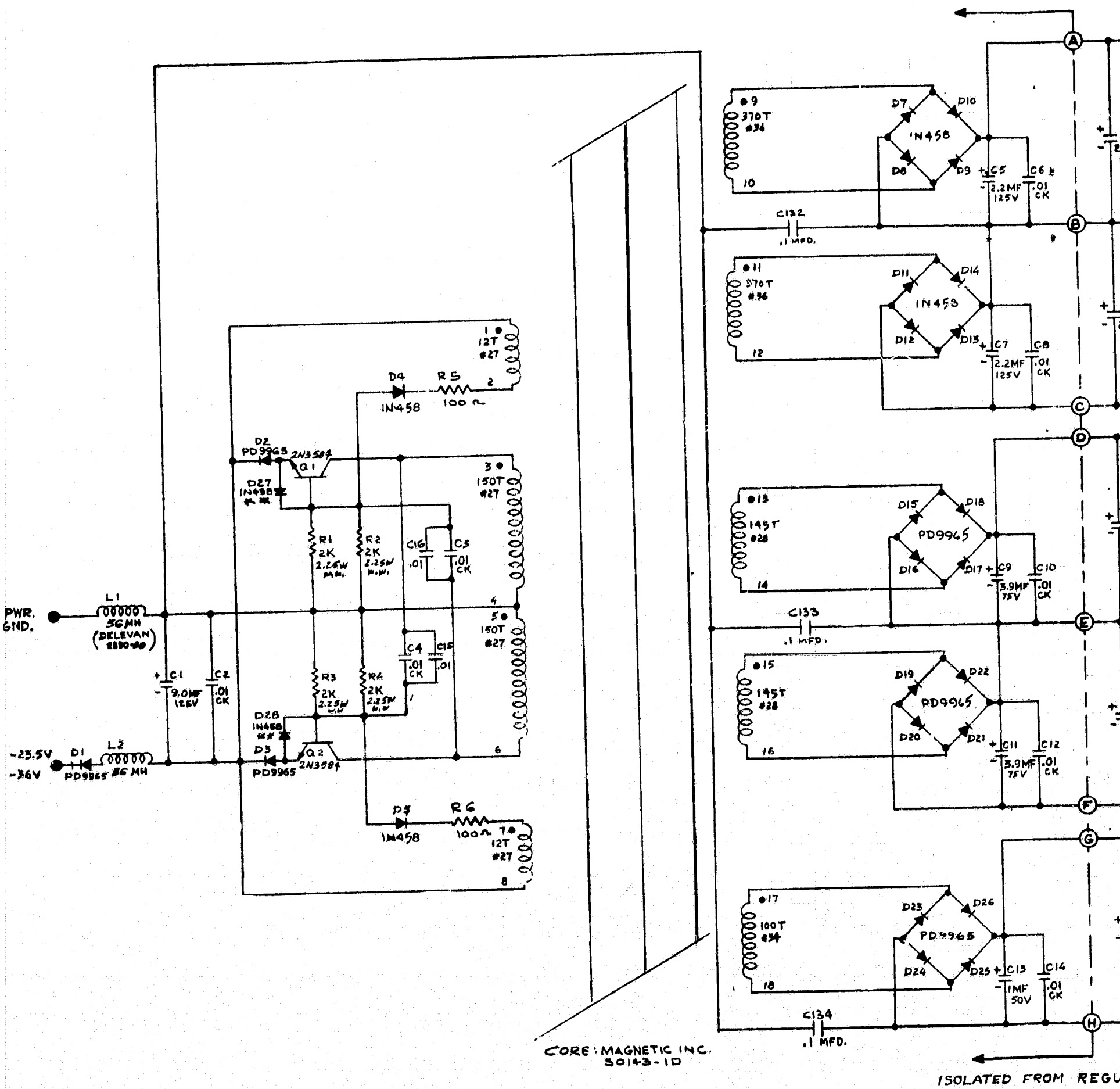



Figure 47. Power Supply, Block Diagram

and 7-8 respectively. Primary windings 3-4 and 5-6 carry the collector currents of Q1 and Q2, respectively. Capacitive cross-coupling of the base of Q1, to the collector of Q2, and vice versa, ensures that regeneration will start upon application of power to the circuit. Capacitors C3 and C4 and resistors R1, R2, R3, and R4 in conjunction with transistors Q1 and Q2 form an astable multivibrator. Due to the astable action, Q1 and Q2 turn OFF, causing the currents in the primary windings to cease flowing. Since the core material of transformer T, is of the square-loop hysteresis-type, regeneration is sustained, and a square wave appears on each of the five secondary windings. The frequency of oscillation is approximately 12 kHz. Each secondary winding output is full-wave bridge-rectified and filtered, as shown in Figure 48.

Components L1, L2, and C1, C2 are included to suppress converter noise on the input power line. The d-c voltage output of each rectifier is then impressed upon the input of an appropriate voltage regulator.


PWR.
GND.
L1
56MH
(DELEVAN
2890-20)
C1
9.0MF
125V
C2
.01
CK
-25.5V
-36V
D1
PD9965
L2
86 MH
D2
PD9965
2N3584
Q1
D27
IN458
R1
2K
2.25W
M.W.
R2
2K
2.25W
M.W.
C16
.01
C5
.01
CK
3
150T
#27
4
5
150T
#27
C4
.01
CK
C15
.01
R3
2K
2.25W
M.W.
R4
2K
2.25W
M.W.
D28
IN458
D3
PD9965
Q2
2N3584
6
D4
IN458
R5
100 Ω
2
1
12T
#27
D5
IN458
R6
100Ω
7
12T
#27
8
CORE: MAGNETIC INC.
50143-1D
9
370T
#36
10
D7
D10
IN458
D8
D9
C5
2.2MF
125V
C6
.01
CK
C132
.1 MFD.
11
370T
#36
12
D11
D14
IN458
D12
D13
C7
2.2MF
125V
C8
.01
CK
13
145T
#28
14
D15
D18
PD9965
D16
D17
C9
3.9MF
75V
C10
.01
CK
C133
.1 MFD.
15
145T
#28
16
D19
D22
PD9965
D20
D21
C11
3.9MF
75V
C12
.01
CK
17
100T
#34
18
D23
D26
PD9965
D24
D25
C13
1MF
50V
C14
.01
CK
C134
.1 MFD.
A
B
C
D
E
F
G
H
ISOLATED FROM REGU

Fallout #1

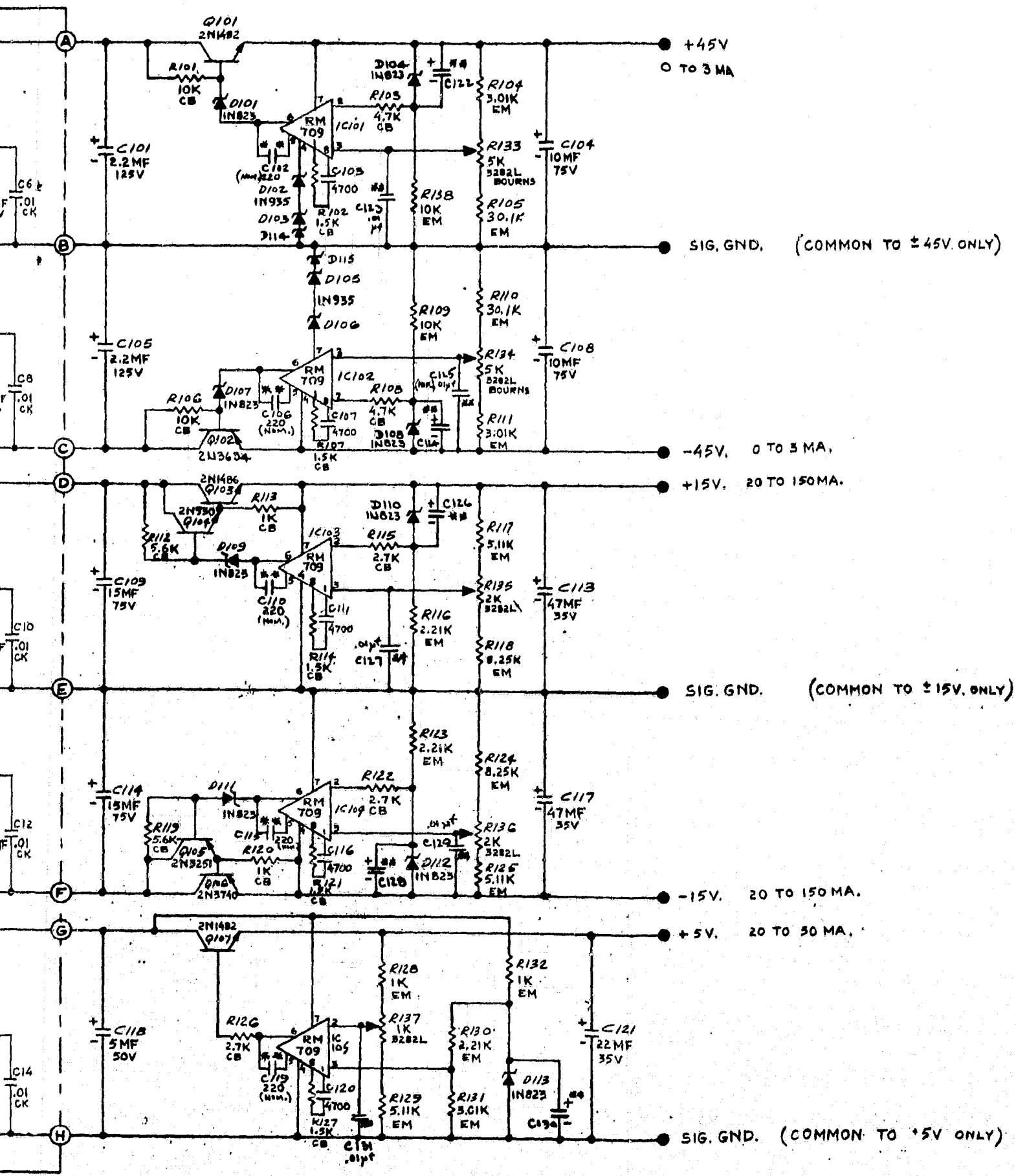



Figure 48. DC-to-DC Converter, Schematic Diagram

Foldout #2

All five voltage regulators utilize the same basic design technique. A typical voltage regulator, shown in Figure 49, consists of a series pass power transistor Q1, error amplifier AR1, a Zener diode voltage reference VR1, and a resistive divider network R1, R2, see Figure 49.

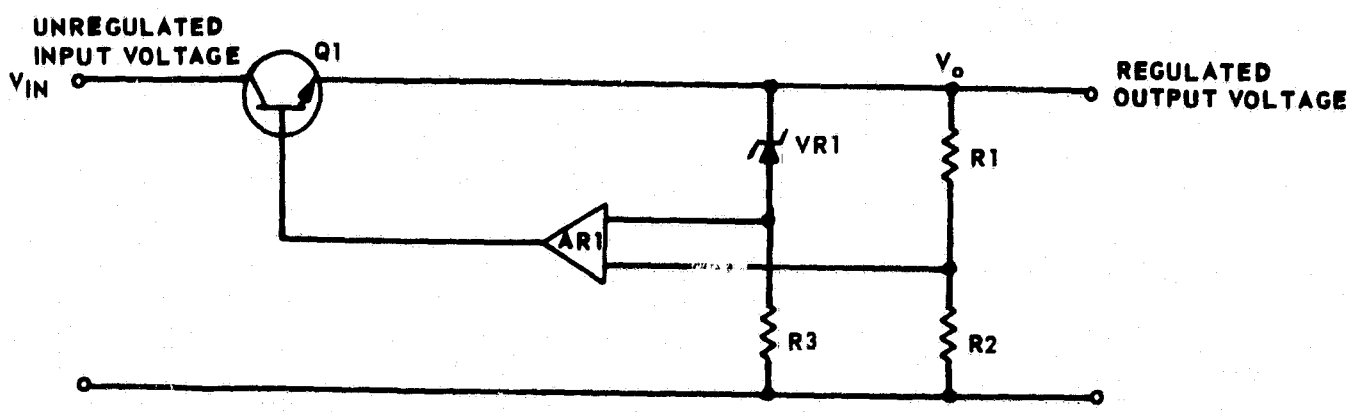



Figure 49. Typical Voltage Regulator, Simplified Schematic

The regulated output voltage, $V_o$, is sampled at the center of the voltage divider network consisting of R1 and R2. The resulting sample is compared to the reference voltage across the Zener diode, VR1. This voltage difference is amplified by the error amplifier AR1 and used to control the voltage drop across transistor Q1 in a manner which keeps $V_o$ constant.

## 6. Mechanical Design

The radiometer assembly consists of three principal subassemblies: the first houses the scan mirror drive motor, the scanning mirror, and the collimator for in-flight calibration of the visual channel; the second houses the Cassegrain telescope objective; and the third houses the detectors, filters, and beamsplitter.

Preamplifier electronics for both channels are mounted near the detectors. Separate castings are used for the scanning mirror and Cassegrain objectives to facilitate the substitution of the scanning mirror design which incorporates the honeycomb shield. In a prototype design, these two castings could be combimed into a single casting with an attendant
saving in weight.

The details of the mechanical construction are shown in Figure 50. The mechanical design was straight-forward with few exceptions. Provision is made for individual focusing in both channels. Provision is also made for translational adjustment of the detectors perpendicular to their respective optical axes so that the fields of view of the two channels can be brought into coincidence.

The only real problem encountered was the differential expansion between the quartz elements of the Cassegrain objective and their metal mounts. Differential expansion over the anticipated temperature range (from -10° to +60°C) is less than 0.2 percent, it is less than 0.1 percent from room temperature to either extreme. The secondary mirror is 1.5 inches in diameter, and the differential expansion is 0.0015 inch. Cement is used to hold the secondary mirror in place because of its tolerance to expansion.

However, the scanning mirror is 5 inches in diameter, which leads to a differential expansion of 0.005 inch. In the present design, the mirror is constrained from axial motion in either direction by direct metal-to-quartz contact. A 0.1-inch wide flat surface around the outer periphery of the front surface rests against a machined surface of the casting into which it mounts. It is held against this surface by a cover plate which presses against its back surface. The edge thickness of the mirror is 0.5 inch; thus, differential expansion is 0.0005 inch. This differential expansion is accommodated by spring washers under the bolts which hold the cover plate against the back of the primary mirror. The differential diametral expansion is accommodated by providing sufficient diametral clearance. In addition, a channel

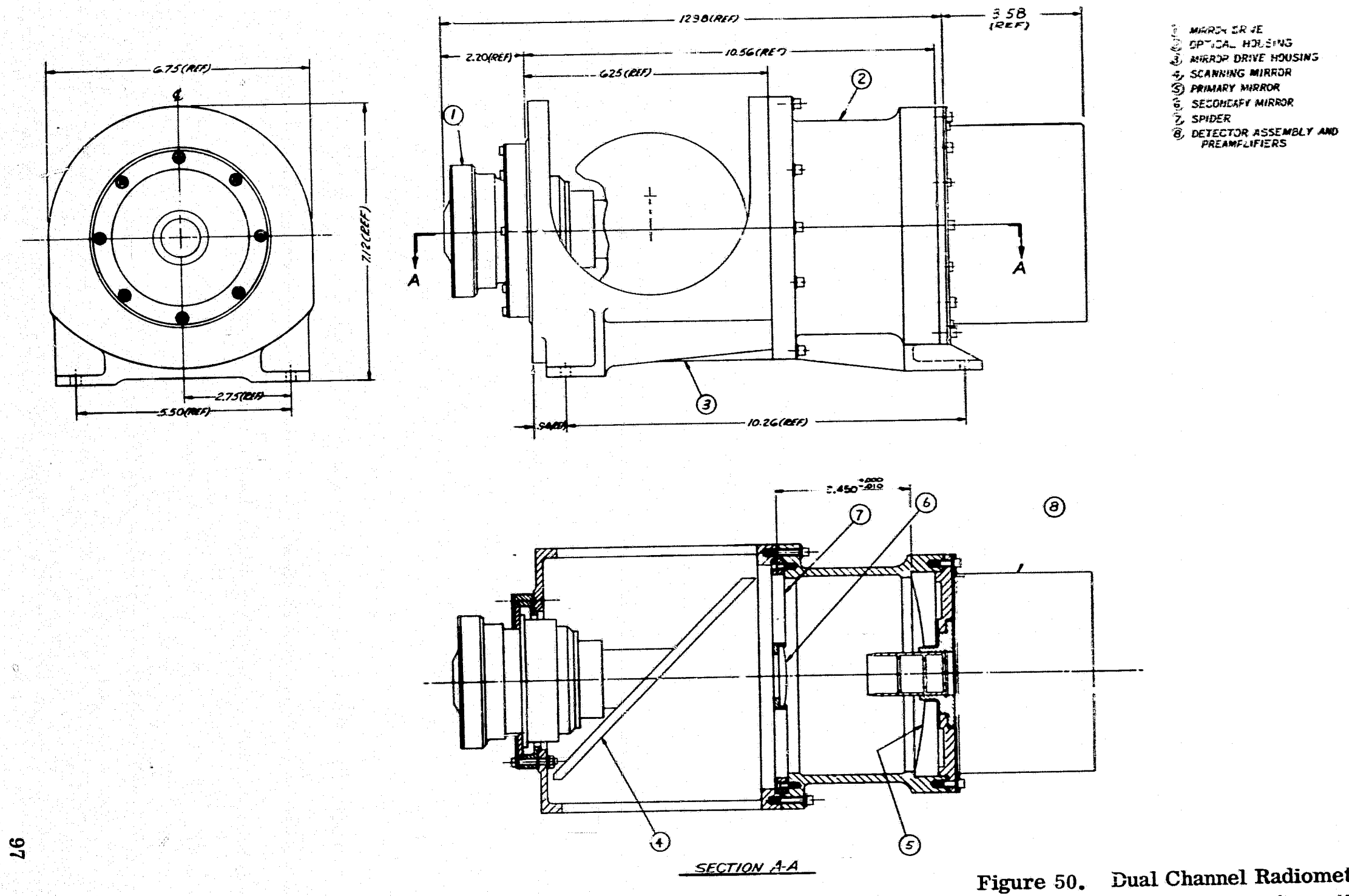



**Figure 50.** Dual Channel Radiometer, Mechanical Configuration

is cut into the casting surface which surrounds the mirror diameter. After alignment is completed, the space between the mirror edge and the casting is completely filled with RTV, which provides support and cushion against radial motion, and also provides damping of axial motion.

A tubular unit contains the drive motor which rotates a 5-inch, 45-degree mounted mirror at a constant speed. Also contained within this unit, and keyed to the shaft with the mirror, is a position encoder which provides electrical signals to the system controls, identifying the position of the mirror.

The drive housing is a simple aluminum shell supporting the encoder stator and the d-c motor stator. To ensure the highest degree of concentricity between the encoder stator and the outside diameter of the shaft bearings, the encoder elements are assembled and potted into the rough-machined shell; then the bearing seats and the inside diameter of the encoder stator are fine-machined at the same setting. Encoder concentricity is critical because of the small radial clearance (0.003 inch) between rotor and stator. A total runout not exceeding 0.0005 inch is achieved in this design. The shell shaft has been designed similarly in that the encoder rotor parts are assembled and potted onto the rough-machined shaft, after which the rotor outside diameter and bearing seats are fine-machined at the same setup. Using this technique, there is virtually no eccentricity between stator and bearing outside diameter or rotor and bearing inside diameter. Thus, the total runout is only that present in the bearings themselves about 0.0003 inch.

The mounting of the Inland T-2157E torque motor presents no problem because of its considerably greater radial clearance with a resultant looser concentricity requirement. The motor stator is retained in the stator shell with four screws, while the rotor is securely clamped between the two splined adapters by a threaded cap.

To mechanically lock all fasteners in place, lockwire, lockwashers, or locking inserts are used in preference to organic thread-locking compounds to minimize contamination of the bearings or encoder surfaces.

The dynamic shaft seal consists of a close-fitting sleeve whose length (0.375 inch) is long relative to its radial width (0.0015 inch). Calculations indicate that at an inside pressure of $10^{-4}$ torr and an outside pressure of $10^{-13}$ torr (space), the leakage rate of lubricant molecules through the seal should not exceed 30 grams/year. Because the internal components of the drive operate satisfactorily at $10^{-4}$ torr, there is no need for static seals, as such. As long as the end caps have a reasonably close pilot fit in the shell, their impedance will be sufficiently higher than the dynamic seal; thus, the molecular leakage through them can be ignored.

A cast or welded-aluminum mirror assembly is rought-machined and permanently bolted to a splined adapter. This adapter performs three functions: (1) acting as the rotating member of the dynamic shaft seal, (2) locking the mirror to the shaft, and (3) providing precision datum for final grinding of the mirror.

## 7. Packaging Design

The dual channel radiometer electronics shown in Figure 51 are divided into two packages: the preamplifiers and the main electronics box.

The IR preamplifier, the common-mode amplifier and the entire visual channel are packaged with the detectors on the back of the mirror housing to achieve a minimum noise pickup condition. The remainder of the electronics are packaged using the standard Improved TOS design concept.

The preamplifiers and the visual channel are located on two circular boards mounted on standoffs directly behind the detectors to prevent RF interference, feed-thru filters are used to connect these circuits to the cable going to the main electronics box. This cable also contains the necessary connections for the encoder, the motor, and the temperature sensors.

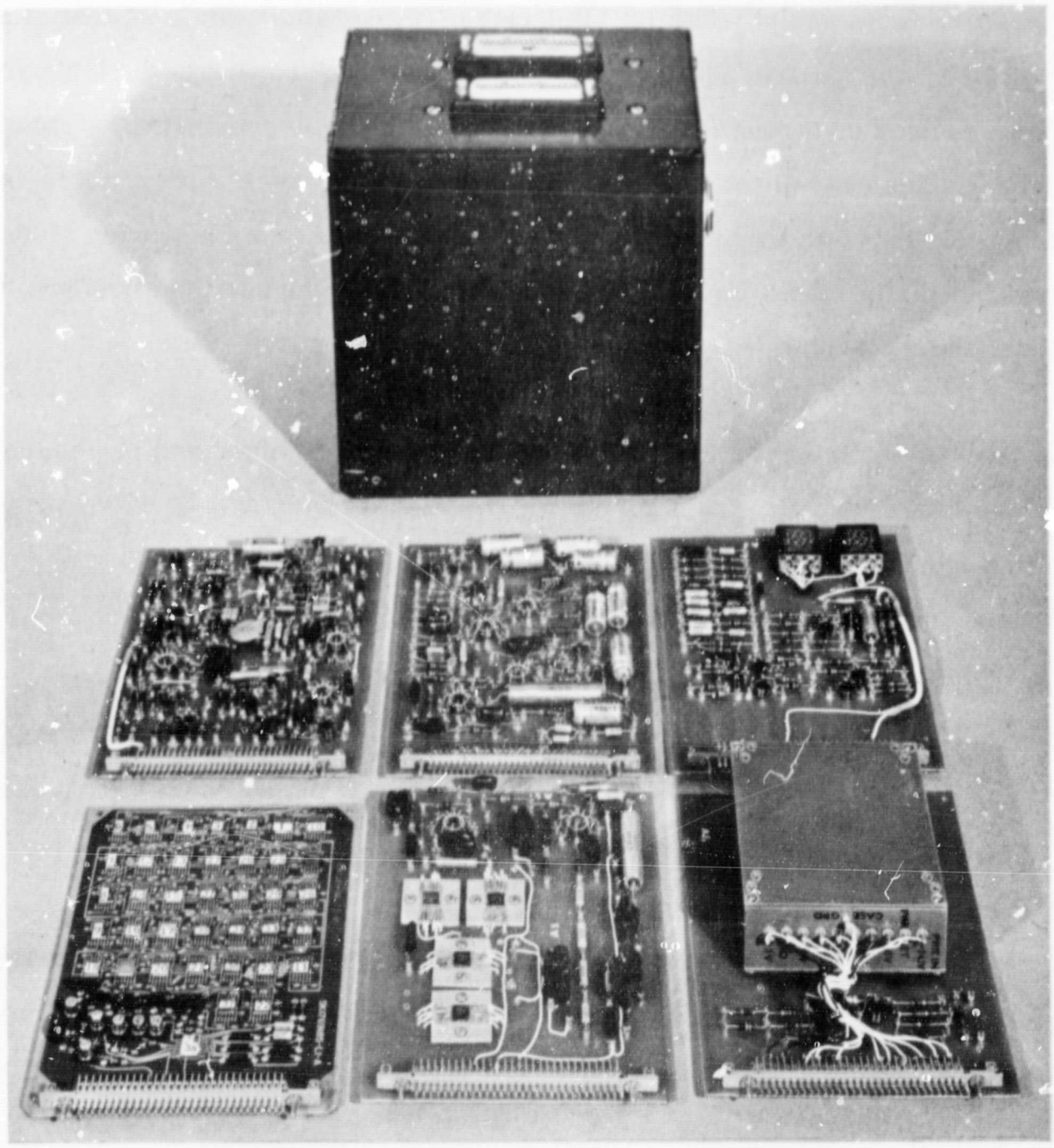


Figure 51. Dual-Channel Scanning Radiometer Electronics Packaging

The main electronics box, containing six circuit boards and a harness board, is 8" by $5\frac{1}{2}$ by 7". There are two 60-pin connectors on the harness board end; one goes to the preamplifiers, the visual channel, and the motor; the other connector goes to the test box.

The six circuit boards are mounted in the box using Bircher slides and 60-pin malco connectors. These circuit boards are spaced 1 inch apart in the following order: A1 - motor drive; A2 - IR amplifier; A3 - telemetry; A4 - logic; A5 - position loop; and A6 - lamp driver and DC/DC converter.

The logic board is a four-layer printed circuit board, while all other boards are hard-wire boards. The power transistors for the motor drive and lamp drive are mounted on the sides of the box to provide proper thermal conduction for these components. Furthermore, the DC/DC converter was mounted on the side of the box to also provide proper thermal conduction for this device.

## 8. Telemetry

Circuitry is included in the dual channel scanning radiometer electronics to provide additional information about important "housekeeping" functions as shown in Figure 52. In actual spacecraft use, these functions would be telemetered to the ground. In this engineering model, these functions are brought out to a test box for observsation.

The housekeeping functions provided are as follows:

- IR detector bias monitor,
- Electronics bias monitor,
- Motor operation indicator, and
- Temperature sensors.

With the exception of the temperature sensors, all monitor and indicator outputs will read -2.5 volts when operation is normal. The voltage output of each temperature sensor will vary linearly with the temperature being monitored. The linearity is within 3 percent. For

$$-20^{\circ}C \leq T \leq +55^{\circ}C$$

the output voltage from the sensor, $V_o$, will be

$$-1.3 \text{ volts} \leq V_o \leq -5.0 \text{ volts}$$

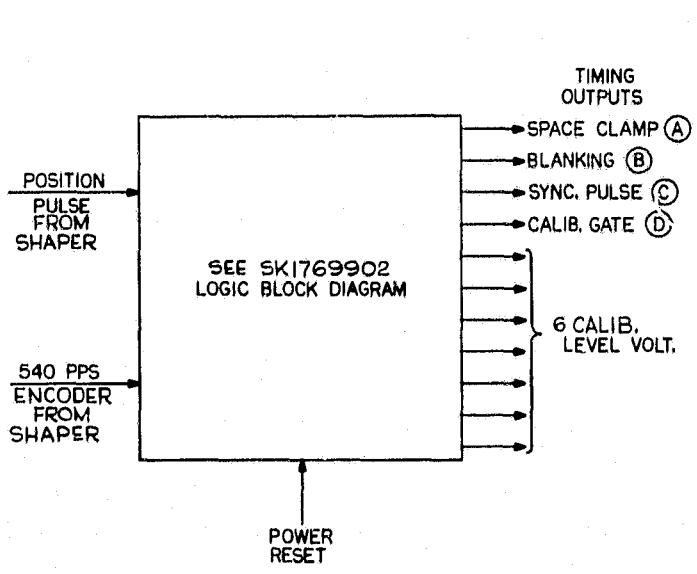
The temperature sensor is a Gulton Industries Voltage Temperature module, model VT-30. It is a three-terminal passive device which, when connected to a regulated power source, supplies an output voltage that is a linear function of temperature.

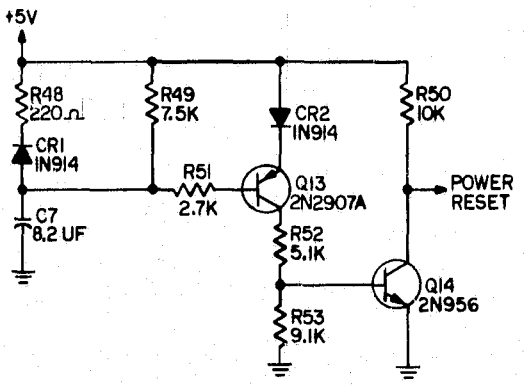
The temperature sensors are mounted to monitor the temperature of the following points:

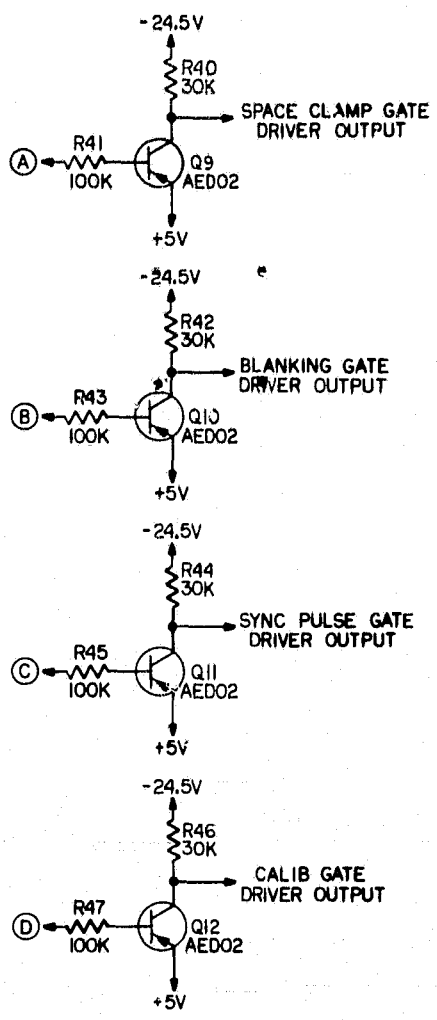
- Housing backscan I,
- Housing backscan II,
- Detector mounts,
- Electronics I,
- Electronics II, and
- Spare.

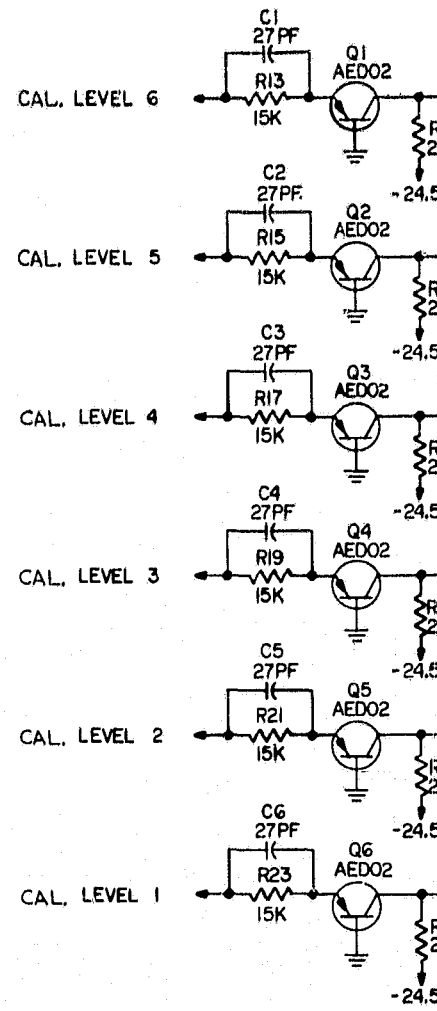
The IR detector bias and electronics bias monitors are resistor networks. The motor operation indicator detects the average value of the square wave from the motor drive squaring amplifier and presents -2.5 volts at its output when the motor frequency is 540 Hz.

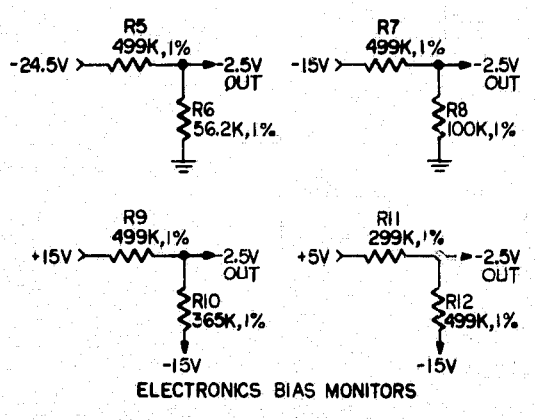
As explained in the logic section, the staircase voltage generator is actually a six-input commutator. This basic commutator could be used to commutate the nine telemetry points from the radiometer by adding two more MEM2009 MOS FET six-input gates and adding two gate signals. Thus, the staircase could be gated off and the MEM2009's gated on to commutator (IR processor) currently used in TOS.



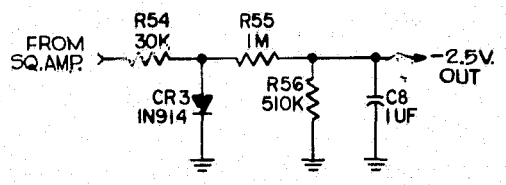



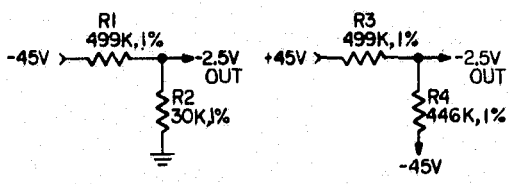



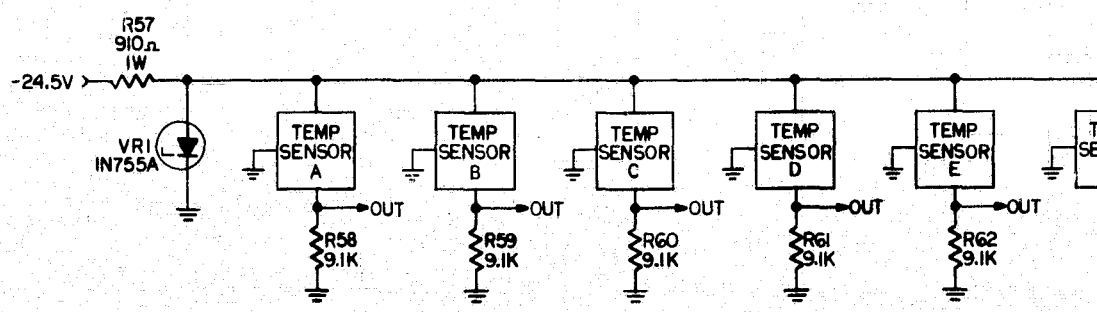

ELECTRONICS BIAS MONITORS




MOTOR OPERATION INDICATOR

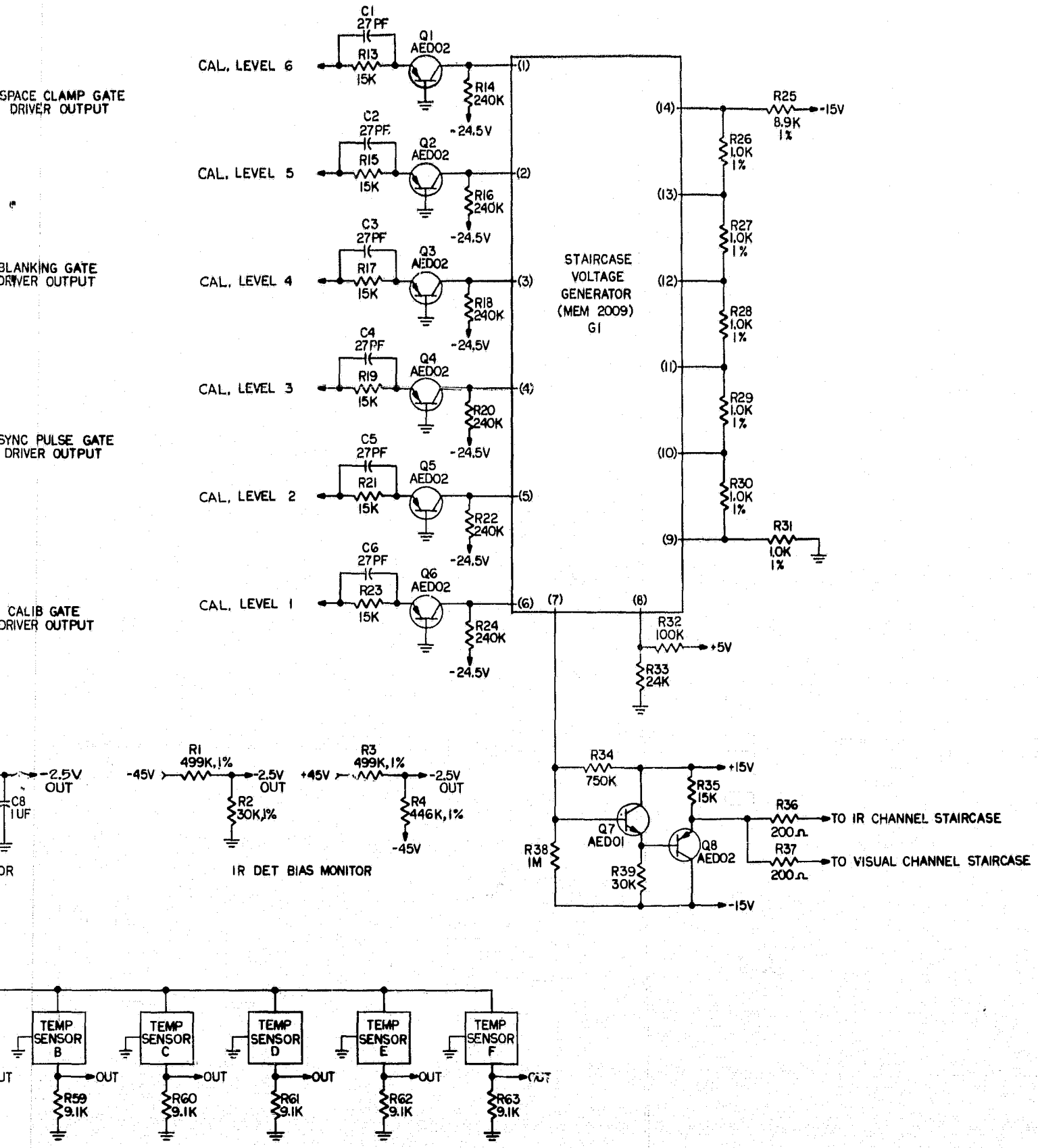



IR DET BIAS MONITOR




NOTE:
1. UNLESS OTHERWISE SPECIFIED, ALL RESISTANCE VALUES ARE IN OHMS, TOL. IS ±5%.

Foldout #1




Foldout #2

Figure 52. Telemetry, Logic, and Gating Circuits, Schematic Wiring Diagram

## D. RADIOMETER CALIBRATION AND TEST

### 1. Alignment and Focusing

The engineering model radiometer was aligned and focused using an infrared collimator. The furnace which supplies radiation for the infrared channel is sufficiently incandescent for use as the radiation source for the visual channel as well. The target aperture of the collimator was set to provide a 1 milliradian scanning spot. The radiometer assembly, with the scanning mirror assembly removed, was placed on a rotary table facing the collimator. Provision was also made for rotating the radiometer in elevation.

The visual detector and the associated magnifying lens were first centered mechanically behind the Cassegrain. Accurate centering to the optical axis of the Cassegrain is not necessary since the spot size produced by the Cassegrain with a point source at infinity is an order of magnitude smaller than the visual detector. Even if this spot size is increased somewhat by off-axis operation, it will still be substantially smaller than the detector. The radiometer was then aimed to center the image of the collimator target on the detector. This was done by scanning the radiometer in azimuth and elevation. Finally, the detector was focused to maximize signal output.

The infrared detector was then focused and aligned. Focusing was accomplished by centering the radiometer on the collimator target for several positions in the focusing range, and setting it at the position which gave maximum output. Alignment consisted of translating the detector perpendicular to the sensor axis until the half voltage directions were centered at the same direction as for the visual channel. Then angle between the half-voltage directions for the visual channel was measured to be approximately 9-arc minutes in each meridian; in the infrared channel it was 10 arc minutes in the azimuth (horizontal) and 15 arc minutes in the elevation (vertical) direction.

## 2. Spatial Resolution Measurements

The measurement of spatial resolution is complicated by the large hyper-focal distance (at least 150 feet) associated with the radiometer. This difficulty has been overcome through the use of a spacer which moves the detector-filter-beamsplitter assembly about 1 inch away from the Cassegrain assembly. This brings the object distance from infinity to approximately 67 feet; however, this means that the Cassegrain objective is not being used with the proper object-image conjugates, and some loss of image definition results. Again, however, because of the order of magnitude difference in size between the detector and the spot produced by a point source at infinity, the resultant loss of resolution is small, if not negligible.

Spatial resolution measurements were made using a 1 foot square field source (a temperature controlled, black painted, heated plate) with appropriate three-bar masks in front of the source. The same targets were used for both infrared and visual channel tests because the front of the target is white and shows three black bars to the visual channel and three "bright" bars to the infrared channel. This technique is particularly useful since signals from the visual and infrared channels can be displayed simultaneously to demonstrate the alignment accuracy of the channels relative to each other.

Resolution measurements are limited to the higher spatial frequencies by the size of the field source at the 67-foot object distance. If measurements are desired at lower spatial frequencies, the spacer between the detector-filter-beamsplitter assembly and the Cassegrain can be increased, with a resultant decrease in object distance. This results in further loss of image definition which is not significant at lower spatial frequencies.

## E. SPACECRAFT INTERFACE

The interface between the dual channel scanning radiometer and the Improved TOS spacecraft can be divided into the following categories:

- Mechanical,
- Electrical,
- Data handling.

### 1. Mechanical

The mounting of the dual channel radiometer on the Improved TOS baseplate in the space presently occupied by the TOS scanning radiometer should be relatively straight-forward. The envelope of this radiometer is smaller than the present TOS scanning radiometer with one minor exception; the housing which shields the detectors and preamplier interferes with the shroud clearance line. The housing can easily be shortened and shaped to fit the shroud by repackaging the preamplifier electronics in the space around the detector mounts. The weight of the radiometer is less than the present TOS radiometer and can be decreased about 2 pounds more by additional machining of excess housing metal, repackaging of the electronics, and a change from the magnetic to an optical encoder in the motor drive. The electronics box has dimensions smaller than the present TOS scanning radiometer and could also be reduced still more with repackaging and by changing from point-to-point wiring to printed-circuit wiring of the electronic boards.

### 2. Electrical

The dual channel radiometer is designed to interface with the existing power supply voltages and command system format of the Improved TOS spacecraft. Two commands in addition to the existing six for the scanning radiometer are required to activate the semi-long and log modes of the visual channel. It does not appear that separate motor and amplifier on-off commands are required for the dual channel

radiometer. The motor command currently used for the TOS scanning radiometer could be borrowed for one of the two required for the visual channel mode switching.

The dual channel radiometer uses 9.5 watts of power from the 24.5 volt supply. This power could be reduced to less than seven watts by substituting a 20-volt motor for the present 3.5-volt motor, changing from the Fairchild $\mu$A709C to the $\mu$A709A operational amplifier, and improving the power supply efficiency from 50 to 60 percent. The $\mu$A709A amplifier can be directly substituted for $\mu$A709C and the 20-volt motor can be directly substituted for the present low-voltage motor. The power supply efficiency can be improved 10 percent by a redesign of the DC/DC converter transformer and the substitution of $\mu$A709A operational amplifier for the $\mu$A709C presently used.

3. Data Handling

Because of the improved resolution (2 nautical miles versus 4 nautical miles) the data format of the video from both channels of the dual channel radiometer is different from the TOS scanning radiometer in the following ways:

- The scan rate is twice that of the TOS radiometer;
- The video bandwidth is 1680 Hz compared to 450 Hz for the TOS radiometer.

Of these two differences, the bandwidth increase is the most significant. This bandwidth increase affects the performance requirements of the tape recorder, multiplexer (MUX), and S-band transmitter in the TOS spacecraft. The present scanning radiometer tape recorder can store the 1680-Hz signal with essentially no change in the transport or electronics requiring only minor changes in phase and amplitude equalization. The MUX would require redesign and the extent of this cannot be assessed without further study. The S-band transmitter can be used without modification. Except for the MUX redesign, it appears that the dual chanel radiometer can be accommodated on the Improved TOS with little impact on current hardware designs.

## F. DIGITAL DATA HANDLING

Conversion of the analog signal to a digital one offers a number of significant advantages. These are:

- Ability to transmit the dynamic range capability of the infrared and visual channel which now varies from 40 to 80 db;
- Preserve linearity, radiometric calibration, and signal-to-noise ratio;
- Elimination of analog sync which currently "wastes" 20 percent of the transmitted dynamic range;
- Elimination of the voltage calibrate signal, which is superfluous in a digital system;
- Ability to stretch the data into the dead time for more efficient tape storage and signal transmission to the ground, and to provide a better aspect ratio in hard-copy reproduction.

The disadvantages of the digital approach are the resulting increased bandwidth and the complexity of the added systen. components and digital tape recorder required to process the analog signal.

A typical digital data handling system for the radiometer is shown in the block diagram of Figure 53.

The analog signal is converted to digital by an 8-bit analog to digital converter. The bit stream is then stored in a buffer store in real time and read out at a rate four times slower to stretch the useful 90-degree signal to occupy a full 360 degree scan angle. This stretched signal is then stored in a tape recorder (e.g., an all-digital-track High Data Rate Storage System - HDRSS recorder).

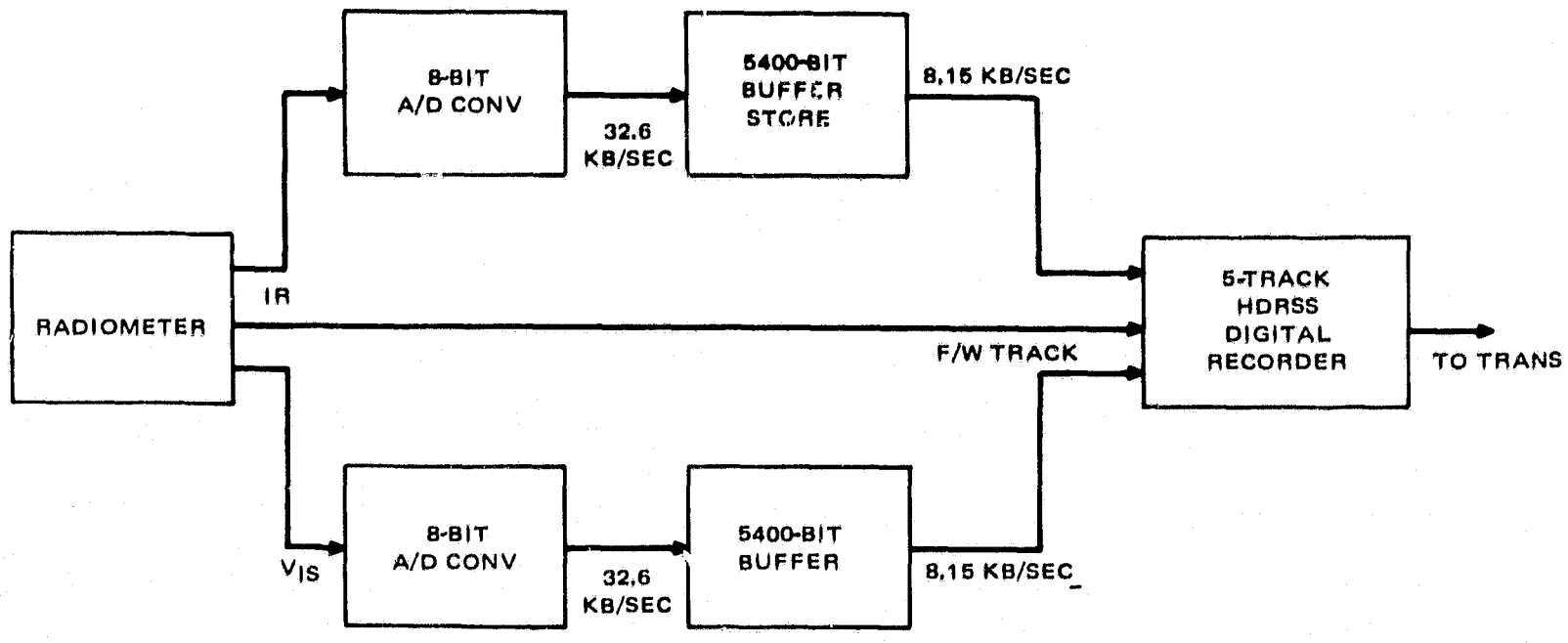



Figure 53. Digital Data Handling System For Radiometer

The recorder bit capacity required can be computed as follows:

$$\text{bit rate/}_{\text{channel}} = \frac{r f_m t A_Q f_s}{T}$$

where

$r$ is the sampling rate = 2.2,

$f_m$ is the maximum video frequency,

$t$ is the useful line time for contiguous coverage (90 degree coverage and no horizons in picture) = 0.167 second,

$A_Q$ is the bits per sample = 8,

$T$ is the scan period = 0.667 second, and

$f_s$ is the factor for sync and calibrate signals = 1.1.

Then,

$$\text{bit rate/}_{\text{channel}} = \frac{2.2 \times 1680 \times 0.167 \times 8 \times 1.1}{0.667}$$

$$= 8.15 \text{ kilobits/second/channel.}$$

Or, 16.3 kilobits/second for both IR and visual channel can be recorded on four tracks of a HDRSS recorder. Thus, with the addition of a timing track, a total of five tracks are required. The present HDRSS recorder is a five-track recorder — two digital and three analog. This recorder can be converted to five digital tracks with no change in the mechanism or heads.

The buffer store for each channel is fed a bit rate of 32.6 kilobits/second during an earth time of 0.167 seconds, or a total 5400 bits. The 5400 bits are read into the buffer store in 0.167 records and read out in 0.667 seconds. It should be noted that the remaining 25 percent of the bits stored from the previous scan are being read out when the bits from the current scan are being stored. A glass delay line appears to have the properties needed for this serial buffer requirement. Magnetic core or MOS array storage could also be considered for this application. Further study would be required to select the most practical and economical approach.